UNIVERSIDADE DE SÃO PAULO
Escola de Engenharia de São Carlos

Efficient numerical computational strategies for solving phase-field models in fracture analysis

Caio Silva Ramos

Doctoral Thesis of the Postgraduate Program in Civil Engineering (Structural Engineering) of the São Carlos School of Engineering, University of São Paulo (SET-EESC-USP)

EESC · USP

Caio Silva Ramos

Efficient numerical computational strategies for solving phase-field models in fracture analysis

CORRECTED VERSION

(The original version is available at São Carlos School of Engineering)

Ph.D. thesis submitted to São Carlos School of Engineering, University of São Paulo (USP), in partial fulfillment of the requirements for the degree of Doctor in Science - Programa de Pós- Graduação em Engenharia Civil (Engenharia de Estruturas).

Advisor: Prof. Dr. Sergio P. B. Proença

Coadvisor: Prof. Dr. Carlos A. Duarte

São Carlos

2025

Ficha catalográfica elaborada pela Biblioteca Prof. Dr. Sérgio Rodrigues Fontes da EESC/USP com os dados inseridos pelo(a) autor(a).

Ramos, Caio Silva
R175e Estratégias numérico-computacional para eficiente solução de modelos de campos de fase na análise de fratura / Caio Silva Ramos; orientador Sergio Persival Baroncini Proença; coorientador Carlos Armando Duarte. São Carlos, 2025.

Tese (Doutorado) - Programa de Pós-Graduação em Engenharia Civil (Engenharia de Estruturas) e Área de Concentração em Estruturas -- Escola de Engenharia de São Carlos da Universidade de São Paulo, 2025.

1. Campos de fase. 2. L-BFGS. 3. Busca linear. 4. Fratura mecânica. 5. Quasi-Newton. I. Título.

Eduardo Graziosi Silva - CRB - 8/8907

FOLHA DE JULGAMENTO

Candidato: Bacharel **CAIO SILVA RAMOS**.

Título da tese: "Estratégias numérico-computacionais eficientes para solução de modelos de campos de fase na análise de fratura".

Data da defesa: 31/10/2025.

Comissão Julgadora	Resultado
Prof. Titular Sergio Persival Baroncini Proenca (Orientador) (Escola de Engenharia de São Carlos/EESC-USP)	APROVADO
Prof. Dr. Marco Lucio Bitttencourt (Universidade Estadual de Campinas/UNICAMP)	APROVADO
Prof. Dr. Geovane Augusto Haveroth (Instituto de Ciências Matemática e de Computação/ICMC-USP)	APROVADO
Prof. Dr. Fernando Pereira Duda (Universidade Federal do Rio de Janeiro/UFRJ)	APROVADO
Prof. Dr. Raul Rosas e Silva (Pontifícia Universidade Católica do Rio de Janeiro/PUC-RIO)	APROVADO

Coordenador do Programa de Pós-Graduação em Engenharia Civil (Engenharia de Estruturas):
Prof Associado **Ricardo Carrazedo**

Presidente da Comissão de Pós-Graduação:
Prof. Titular **Carlos De Marqui Junior**

ACKNOWLEDGEMENTS

I wish to start by expressing my profound gratitude to my supervisors, Prof. Sergio Proença – USP and Prof. Armando Duarte – UIUC, for their unwavering support throughout these years of doctoral research. I am immensely grateful for the chance to be part of two such exceptional research groups and for all the expertise they imparted to me, as well as their dedication to my academic development. I particularly want to acknowledge Prof. Duarte for welcoming me to Urbana-Champaign during the year I resided there conducting part of this doctoral investigation. I also wish to recognize the examination committee members for their insightful feedback and essential recommendations that enhanced my work. My appreciation extends to all faculty members and staff of the Department of Structural Engineering (SET) at São Carlos School of Engineering – University of São Paulo, for the assistance provided during my doctoral journey. Special recognition goes to colleagues from both research groups for their extraordinary contribution to the development of this investigation and for the extensive discussions regarding computational implementation, C++, and phase-field methodologies.

My gratitude also goes to all my friends from Imperatriz, who remained close despite the geographical distance, from São Carlos, and from Urbana-Champaign for the memorable conversations and for making life during my doctoral studies much more enjoyable. I cannot adequately express in words the significance each of you has had during this period. I want to convey my eternal appreciation to my parents, Dinha and Antônio, for consistently having faith in me, dedicating all efforts to provide me with quality education, understanding my decisions, and for all the affection and encouragement throughout these years away from home.

Finally, I wish to acknowledge with appreciation the financial assistance provided by the São Paulo Research Foundation – FAPESP, through grants #2019/00434-7 and #2020/14605-5.

"O otimista é um tolo. O pessimista, um chato.
Bom mesmo é ser um realista esperançoso."
Ariano Suassuna

ABSTRACT

RAMOS, C. S. **Efficient numerical computational strategies for solving phase-field models in fracture analysis**. 2025. Thesis (Doctorate in Science) - São Carlos School of Engineering, University of São Paulo, São Carlos, 2025.

Phase-field models for fracture have emerged as powerful computational frameworks that provide a variational formulation of Griffith-type fracture mechanics by describing the competition between elastic and fracture energy potentials. These models naturally incorporate fracture evolution into the governing equations, allowing cracks to propagate along paths of least energy resistance without requiring explicit crack tracking algorithms or *ad hoc* propagation criteria. However, phase-field fracture simulations are computationally expensive due to the non-convex, highly nonlinear nature of the energy functional, which leads to poor convergence in standard Newton-Raphson solvers. This work addresses these computational challenges through two algorithmic innovations: an enhanced Limited-memory Broyden–Fletcher–Goldfarb–Shanno (L-BFGS) method with a novel quasi-Newton line search strategy, and the BORAM algorithm that combines L-BFGS with Over-Relaxed Alternating Minimization (ORAM). The enhanced L-BFGS incorporates a gradient-based line search method that ensures algorithmic robustness by dynamically adjusting search directions with adaptive step sizes, preventing divergence during critical crack propagation events. The BORAM algorithm provides an adaptive solution strategy that employs convergence rate detection to automatically switch between L-BFGS and ORAM methodologies based on real-time assessment of crack evolution dynamics. Comprehensive numerical experiments covering brittle and quasi-brittle fracture scenarios demonstrate that both algorithms achieve substantial computational efficiency gains, with average performance improvements of approximately five-fold compared to traditional alternating minimization approaches, while maintaining high accuracy and robustness across diverse fracture patterns and mixed-mode loading conditions.

Keywords: Phase-field. L-BFGS. Line search. Fracture mechanics. Quasi-Newton.

RESUMO

RAMOS, C. S. **Estratégias numérico-computacionais eficientes para solução de modelos de campos de fase na análise de fratura**. 2025. Tese (Doutorado em Ciências) - Escola de Engenharia de São Carlos, Universidade de São Paulo, São Carlos, 2025.

Os modelos de campo de fase para fratura emergiram como estruturas computacionais poderosas que fornecem uma formulação variacional da mecânica da fratura tipo Griffith, descrevendo a competição entre os potenciais de energia elástica e de fratura. Esses modelos incorporam naturalmente a evolução da fratura nas equações governantes, permitindo que as trincas se propaguem ao longo de caminhos de menor resistência energética sem exigir algoritmos explícitos de rastreamento de trincas ou critérios de propagação *ad hoc*. No entanto, as simulações de fratura por campo de fase são computacionalmente caras devido à natureza não-convexa e altamente não-linear do funcional de energia, que leva ao baixo desempenho do solucionador Newton-Raphson padrão. Este trabalho aborda esses desafios computacionais através de duas inovações algorítmicas: um método aprimorado de Limited-memory Broyden–Fletcher–Goldfarb–Shanno (L-BFGS) com uma nova estratégia de busca linear quasi-Newton, e o algoritmo BORAM que combina L-BFGS com Minimização Alternada Super-Relaxada (ORAM). O L-BFGS aprimorado incorpora um método de busca linear baseado em gradiente que garante robustez algorítmica ao ajustar dinamicamente as direções de busca com tamanhos de passo adaptativos, prevenindo a divergência durante eventos críticos de propagação de trincas. O algoritmo BORAM fornece uma estratégia de solução adaptativa que emprega detecção de taxa de convergência para alternar automaticamente entre as metodologias L-BFGS e ORAM com base na avaliação em tempo real da dinâmica de evolução das trincas. Experimentos numéricos abrangentes cobrindo cenários de fratura frágil e quasi-frágil demonstram que ambos os algoritmos alcançam ganhos substanciais de eficiência computacional, com melhorias de desempenho médias de aproximadamente cinco vezes comparadas às abordagens tradicionais de minimização alternada, mantendo alta precisão e robustez em diversos padrões de fratura e condições de carregamento.

Palavras-chave: Campos de fase. L-BFGS. Busca linear. Fratura mecânica. Quasi-Newton.

LIST OF FIGURES

LIST OF TABLES

CONTENTS

1 INTRODUCTION

The mechanics of damage and failure in engineering applications are essential for safety. An accurate assessment of crack propagation behavior can enhance the prediction of limit load capacity, preventing the collapse of structures and optimize the shape and topology dimensions of the structural components.

Griffith [1] proposed the first theory for brittle crack evolution, which states that upon violation of the critical energy release rate, the crack can propagate. Since then, aiming to account for the complexity of the crack processes, several numerical methods have been developed to model crack propagation in solids. Essentially, these methods can be classified into two categories: (i) discrete crack approaches, where the crack is explicitly modeled as a discontinuity in the displacement field, and (ii) continuous crack approaches, where the crack is implicitly modeled through a continuous field variable. In the case of discrete cracks, the discontinuities are discretized either by re-meshing strategies or by enriching the displacement field with discontinuous functions using, for example, a partition of unity method [2–4]. Although such approaches are able to capture the crack path and the crack opening displacement, rigorous additional criteria are required to predict whether a crack propagates or initiates, as well as the orientation of the new crack increments. Among the continuous approach, the phase-field model has gained popularity in recent years due to its ability to model complex crack configurations without needing *ad hoc* criterion or extrinsic tracking algorithm.

Phase-field models for fracture are energy-based frameworks [5–7] that provide a variational formulation of Griffith-type fracture mechanics by describing the competition between elastic and fracture energy potentials. This approach naturally incorporates fracture evolution into the governing equations, allowing cracks to propagate along paths of least energy resistance. In these models, sharp crack discontinuities are approximated as diffuse regions characterized by a scalar variable, so called phase-field, which enables a smooth mathematical transition between the intact and fractured states of the material.

The theoretical foundation of phase-field models for fracture originates from the variational approach to quasi-static brittle fracture introduced by [5]. Subsequently, [6, 7] established the numerical implementation framework for this approach, introducing a regularization length scale parameter that controls the bandwidth of the diffuse damage zone. As this parameter approaches zero, the diffuse solution converges to the original sharp crack problem, ensuring mathematical consistency.

Since its initial development, the phase-field approach has been significantly enhanced and successfully applied to numerous complex problems in computational fracture

mechanics. Notable extensions include coupled phenomena such as elastoplasticity [8], dynamic fracture [9, 10], thermo-mechanical coupling [11, 12], finite deformation fracture [13], stress corrosion cracking [14], hydrogen embrittlement [15, 16], and hydraulic fracturing [17, 18], among many others. The versatility of phase-field models has been demonstrated through their successful application to complex crack pattern prediction in brittle and quasi-brittle materials, including concrete, ceramics, and metals. Furthermore, these models have been extended to accurately capture mixed-mode fracture scenarios, where cracks can initiate and propagate under combined loading conditions involving multiple fracture modes simultaneously.

A well-known limitation of phase-field models is their prohibitive computational cost, which stems from two primary sources. First, the necessity of extremely refined meshes in finite element discretizations to accurately resolve the steep damage gradients within the narrow fracture zone results in large-scale systems with high number of degrees of freedom. To address this computational challenge, adaptive mesh refinement techniques [19, 20] and multiscale methods [21–23] have been developed and have demonstrated significant success in minimizing the required degrees of freedom while maintaining solution accuracy.

The second major contributor to computational expense is the non-convex and highly nonlinear nature of the energy functional with respect to both displacement and phase-field variables [6]. Under these conditions, standard Newton-Raphson monolithic solvers exhibit poor performance and convergence characteristics. The iterative solution process frequently diverges, particularly during instances of rapid crack propagation, commonly referred to as "brutal crack evolution" [19, 24].

To address these convergence challenges, numerous solution strategies have been proposed in the literature. Gerasimov and Lorenzis [24] introduced a specialized line search algorithm that is activated when energy increases are detected between consecutive iterations. Wick [25] developed an error-oriented Newton algorithm combined with augmented Lagrangian techniques, where the Newton convergence criterion adapts based on the outer augmented Lagrangian error. Additional approaches include a modified Newton method capable of switching between full Newton and Newton-like systems through residual monitoring [26], an inertial correction technique incorporating Armijo backtracking line search [27], and a recursive multi-level trust-region method [28].

Despite these advances, none of these monolithic approaches have emerged as the standard solver for phase-field fracture problems. This situation likely arises from their inherent complexity, variable robustness across different problem types, and problem-dependent computational efficiency, which collectively limit their widespread adoption in the computational fracture mechanics community.

Due to the convex nature of the energy functional with respect to each individual argument (displacement and phase-field variables), the most widely adopted approach

involves decoupling the weak formulation through alternating updates of the displacement and phase-field variables based on separate minimization subproblems [29–31]. This technique, known as alternating minimization (AM) or the staggered algorithm, demonstrates excellent robustness but requires substantial computational resources.

The AM algorithm exhibits reduced performance at critical loading stages, necessitating a considerable number of iterations to achieve convergence [24, 32]. Furthermore, very small load increments are required to maintain equilibrium path tracking [33]. To address the computational limitations of the AM algorithm, various acceleration techniques have been developed. These include a linearized staggered scheme incorporating stabilizing parameters [34], a hybrid approach combining over-relaxed AM with monolithic Newton methods [35], and a hybrid algorithm utilizing over-relaxed AM with Anderson's acceleration [36]. A comprehensive review of existing acceleration techniques for phase-field fracture models is available in [37].

The fundamental principle underlying these acceleration techniques involves enhancing AM algorithm convergence through modifications to the incremental solution of the minimization problem. Alternative improvements to AM algorithm performance can be achieved through adaptive load increment strategies, as demonstrated in [38], where load increments vary dynamically between predefined minimum and maximum values. Within the framework of monolithic methods, displacement increment control based on phase-field variables and their increments has been implemented [33, 39], alongside load control strategies utilizing arc-length methods [40].

However, these methods typically require numerical parameter calibration or time step convergence studies, resulting in additional computational overhead while maintaining the inherent decoupling between displacement and damage fields.

Within a monolithic computational framework, this work explores the application of a quasi-Newton method of Broyden–Fletcher–Goldfarb–Shanno (BFGS) type, specifically its Limited-memory variant (L-BFGS), within the framework of phase-field models for fracture analysis. The BFGS approach has been identified as a promising alternative due to its computational efficiency and algorithmic robustness [32, 33, 39, 41]. However, these previous studies utilized BFGS implementations available within the commercial software ABAQUS [42], which lacks open-source accessibility and restricts user modifications to the underlying algorithm.

This study proposes a modified BFGS variant specifically designed for phase-field analysis, which accommodates non-convex energy functionals through the introduction of a novel quasi-Newton line search strategy to enhance the robustness of monolithic solution approaches. Despite Jin, Li and Chen [20] recently developed their own BFGS implementation, this and similar studies employing BFGS methods have not adequately addressed the critical importance of line search strategies and their impact on algorithmic

robustness within phase-field modeling contexts. This thesis intends to fill that gap and the primary contributions of the hereby proposed modified BFGS have been published in a peer-reviewed journal article [43].

Furthermore, this work presents a hybrid algorithm that combines the BFGS method with an over-relaxed alternating minimization (ORAM) approach, thereby integrating the computational advantages of both methodologies. This novel hybrid algorithm is designated as BORAM (Hybrid L-**B**FGS **ORAM**), representing a comprehensive solution strategy for phase-field fracture problems.

Numerical simulations and computational analyses demonstrate that the proposed algorithms are not only robust for non-variational phase-field models, but also exhibit significantly higher computational efficiency compared to standard AM.

1.1 Objective

The main aim is to develop and implement efficient numerical algorithms for phase-field fracture models that overcome the computational limitations of existing solution methods while maintaining accuracy and robustness in simulating complex crack propagation phenomena.

1.2 Specific objectives

The specific objectives of this research are: (I) develop a modified L-BFGS method with a novel quasi-Newton line search strategy specifically designed for non-convex energy functionals in phase-field fracture analysis; (II) create the BORAM algorithm that combines L-BFGS with Over-Relaxed Alternating Minimization (ORAM) through convergence rate detection mechanisms for automatic switching based on real-time crack evolution assessment; (III) enhance algorithmic robustness and stability to address convergence challenges during critical crack propagation events and brutal crack evolution scenarios; (IV) develop an open-source computational implementation of the proposed algorithms to provide accessible and modifiable solutions that overcome limitations of commercial software and contribute to the computational fracture mechanics community; (V) conduct comprehensive numerical validation through extensive experiments covering brittle and quasi-brittle fracture scenarios to demonstrate accuracy preservation and quantify performance improvements across diverse fracture patterns and mixed-mode loading conditions.

1.3 Methodology

The computational framework for this doctoral research was developed through programming work conducted by the author within existing object-oriented C++ platforms maintained by the research groups of Prof. Proença (USP) and Prof. Duarte (UIUC). These software environments were initially designed exclusively for Linear Elastic Fracture Mechanics applications utilizing various Generalized Finite Element Method (GFEM) formulations.

To address the research objectives of this thesis, additional computational capabilities were required beyond the existing GFEM functionality. Phase-field modeling features were implemented, including the mathematical formulation and numerical solution algorithms for the corresponding system of equations. These additions extended the software's capabilities to enable phase-field-based fracture simulations.

All newly developed algorithms were verified against benchmark problems featuring either closed-form analytical solutions or well-established numerical results documented in the scientific literature. This verification process ensured the accuracy and reliability of the computational methods before their application to the research problems.

The numerical simulations and computational analyses presented throughout this document, along with additional preliminary studies not included herein, were executed on an Intel(R) Core(TM) i7-8750H CPU @ 2.20GHz with 16 GB RAM. This computational environment provided adequate performance for the complex numerical procedures required by the phase-field implementations.

1.4 Outline

The remaining of this document is organized as follows:

Chapter 2 presents the theoretical foundations of fracture mechanics, covering the principles of Linear Elastic Fracture Mechanics (LEFM) and the transition from discrete to regularized approaches. In Chapter 3, the phase-field approach to fracture mechanics is introduced, including the regularized fracture energy functionals and their variational formulations. The chapter details the `AT2` and cohesive zone models (`CZM`) used throughout this Ph.D. thesis, including the mathematical formulation of the coupled displacement-phase-field system and the treatment of irreversibility constraints through history variables.

The solution algorithms for the nonlinear system of equations arising from phase-field fracture problems are described in Chapter 4, presenting the traditional alternating minimization (AM) approach and introducing the Limited-memory Broyden-Fletcher-Goldfarb-Shanno (L-BFGS) method with a quasi-Newton line search strategy for phase-field

applications. The chapter also presents the BORAM algorithm.

In Chapter 5 numerical experiments covering both brittle and quasi-brittle fracture scenarios are presented. Multiple benchmark problems are analyzed. Performance comparisons between AM, L-BFGS, and BORAM algorithms are presented, analyzing computational efficiency and convergence characteristics for different crack propagation patterns.

Finally, Chapter 6 presents the main conclusions of the present Ph.D. research, summarizing the contributions of the L-BFGS method and the BORAM algorithm. The chapter discusses the applicability of these methodologies and proposes topics for future investigation.

2 CONTINUOUS AND DISCONTINUOUS FRACTURE MODELS

2.1 Fracture Mechanics in a Nutshell

Cracks represent the macroscopic manifestation of microstructural defect evolution – such as dislocation accumulation in ductile metals, microvoid coalescence in porous solids, or interfacial decohesion in composite systems [44–46] – governed by material-specific failure mechanisms. For instance, ductile materials (e.g., metals) exhibit energy dissipation through plastic (inelastic) deformation prior to fracture, whereas brittle materials (e.g., ceramics, glass) and quasi-brittle materials (e.g., concrete, rock, or polymers like polymethylmethacrylate (PMMA)) exhibit minimal energy absorption, failing catastrophically. Quasi-brittle materials, distinct from purely brittle ones, demonstrate limited inelastic deformation (e.g., microcrack networks or fiber bridging [44]) prior to failure.

Fig. 1 illustrates the near-tip behavior of brittle and ductile fractures. Brittle fracture is characterized by globally elastic behavior, except within a small region termed the fracture process zone, where nonelastic mechanisms (e.g., plasticity, damage) dominate [44]. This regime, known as the small-scale yielding condition, reflects the predominance of elasticity in governing structural response and crack propagation. In contrast, ductile fracture is defined by extensive plasticity, with a large plastic zone enveloping the crack tip [44]. Here, inelastic material behavior (e.g., plasticity, damage) becomes critical to accurately predict crack evolution and structural integrity, as plasticity governs both the near-tip mechanics and the overall deformation of the cracked body. This study focuses on brittle and quasi-brittle fracture, where crack propagation under tensile stress dominates, and plastic deformation is negligible or confined to a small fracture process zone.

Figure 1 – Near-tip behavior of fracture mechanics. (a) Brittle material. (b) Ductile material.

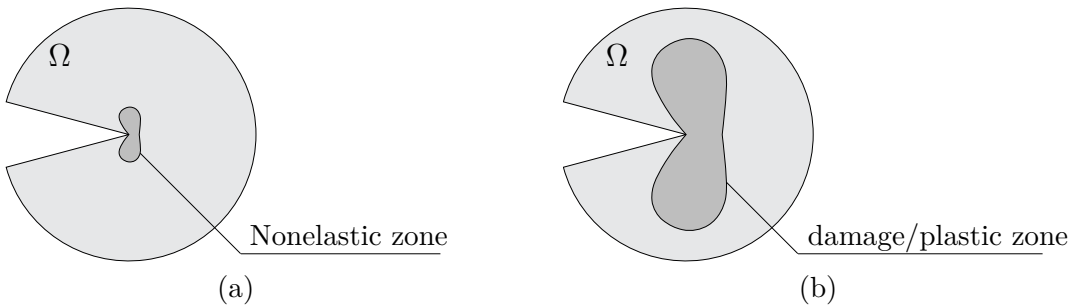

Source: The author.

The evolution of cracks in materials can be analyzed through two complementary perspectives: temporal evolution, which describes when and how cracks develop over time, and spatial evolution, which focuses on where and how cracks propagate geometrically.

The temporal evolution examines the sequence of stages in crack formation and growth:

- **Nucleation:** Formation of a new crack in a previously flawless material under external stress.
- **Initiation:** Activation of growth in an existing defect or macro-crack.
- **Propagation:** The most critical phase for structural safety, propagation (stable or unstable) involves energy dissipation governed by the material's fracture toughness – the energy required to extend a crack per unit area. This energy loss balances the release of stored mechanical energy.

While spatial evolution characterizes the physical path and geometry of the crack:

- **Curving/Kinking:** Gradual curvature or abrupt angular deviations in the crack path.
- **Branching:** Splitting of a single crack into multiple branches, altering topology by creating new crack tips.
- **Coalescence:** Merging of separate cracks into a unified fracture.

Together, these dimensions provide a holistic understanding of crack behavior, essential for predicting structural failure and optimizing material design.

2.1.1 Griffith's theory of fracture

From a kinematic perspective, cracks $\Gamma_t \subset \mathbb{R}^{d-1}$ (with $d \in \{1, 2, 3\}$) are conventionally modeled within the reference configuration as propagating interfaces in the initially intact domain $\bar{\Omega} = \Omega \cup \partial\Omega$ in $\mathbb{R}^d$. Under load applied to the external boundary $\partial\Omega$, the deformed configuration $\mathcal{F}_t(\Omega \setminus \Gamma_t)$ of the fractured body is kinematically described for a given point $\boldsymbol{x} \in \Omega \setminus \Gamma_t$ by the vector displacement field $\boldsymbol{u}_t = \boldsymbol{u}(\boldsymbol{x},t)$. Away from the crack, the displacement field satisfies the classical local equilibrium momentum equation, which in the absence of body forces reads

$$\begin{aligned} \nabla \cdot \boldsymbol{\sigma}_t &= 0 \qquad \text{in } \Omega \setminus \Gamma_t, \\ \boldsymbol{\sigma}_t \cdot \boldsymbol{n} &= \bar{\boldsymbol{F}}_t \quad \text{on } \partial\Omega_{\boldsymbol{F}}, \\ \boldsymbol{u}_t &= \bar{\boldsymbol{u}}_t \quad \text{on } \partial\Omega_u. \end{aligned} \tag{2.1}$$

where $\boldsymbol{n}$ is the outward unit normal vector to $\partial\Omega$, $\bar{\boldsymbol{F}}_t$ and $\bar{\boldsymbol{u}}_t$ are prescribed surface tractions and displacements applied on $\partial\Omega_{\boldsymbol{F}}$ and $\partial\Omega_u$, respectively, such that $\partial\Omega_u \cup \partial\Omega_{\boldsymbol{F}} = \partial\Omega$ and $\partial\Omega_u \cap \partial\Omega_{\boldsymbol{F}} = \varnothing$. Considering homogeneous and isotropic materials, the Cauchy stress

tensor $\boldsymbol{\sigma}_t$ is related to the displacement field $\boldsymbol{u}_t$ through the constitutive law, which can be expressed in terms of Lamé's coefficients λ and μ as follows

$$\boldsymbol{\sigma}_t = \lambda \text{tr}(\boldsymbol{\varepsilon}_t)\mathbf{I} + 2\mu\boldsymbol{\varepsilon}_t, \tag{2.2}$$

with $\mathbf{I}$ being the identity tensor of rank d. The hypothesis of small displacements and strains for britlle and quasi-brittle materials leads to the definition of the linearized infinitesimal strain tensor $\boldsymbol{\varepsilon}_t = \boldsymbol{\varepsilon}(\boldsymbol{u}_t) = \frac{1}{2}\left(\nabla \boldsymbol{u}_t + (\nabla \boldsymbol{u}_t)^T\right)$.

The foundational premise of Griffith's fracture theory centers on the energy dissipation associated with a propagating crack Γ_t. This crack is modeled as a sharp interface within the bulk material Ω. Griffith [1] postulates that crack formation necessitates an energy expenditure proportional to the crack's surface area $|\Gamma_t|$. This proportionality reflects the energy required to rupture atomic bonds at the microscale along the crack interface. Consequently, the crack surface can be interpreted as possessing a surface energy density, expressed as

$$\Upsilon(\Gamma_t) = \mathcal{G}_c|\Gamma_t|, \tag{2.3}$$

where $\mathcal{G}_c$ is a material property known as the critical energy release rate. This parameter quantifies the energy required to create a unit area of crack surface within the material, i.e., the fracture toughness. By using the principle of energy conservation, the total balance of energy $\mathcal{E}$ of the cracked body can be expressed as

$$\mathcal{E}(\boldsymbol{u}_t, \Gamma_t) = \Psi(\boldsymbol{u}_t, \Gamma_t) + \Upsilon(\Gamma_t) - \mathcal{P}(\boldsymbol{u}_t), \tag{2.4}$$

where $\mathcal{P}(\boldsymbol{u}_t)$ denotes the external potential energy and $\Psi(\boldsymbol{u}_t)$ represents the elastic potential energy stored within the body, defined respectively as

$$\mathcal{P}(\boldsymbol{u}_t) = \int_{\partial\Omega_{\boldsymbol{F}}} \bar{\boldsymbol{F}}_t \cdot \boldsymbol{u}_t \, \mathrm{d}s, \tag{2.5}$$

and

$$\Psi(\boldsymbol{u}_t,\Gamma_t) = \int_{\Omega/\Gamma_t} \psi(\boldsymbol{\varepsilon}_t) \, \mathrm{d}\Omega, \tag{2.6}$$

with the elastic strain energy density function given by $\psi(\boldsymbol{\varepsilon}) = \frac{1}{2}\lambda \text{tr}^2(\boldsymbol{\varepsilon}) + \mu \text{tr}(\boldsymbol{\varepsilon}^2)$. In this context, the Griffith's fracture criteria can be reformulated based on energy minimization concepts, such that the rate of change of the total energy $\mathcal{E}$ is given by

$$\frac{\partial}{\partial t}\left(\Psi(\boldsymbol{u}_t,\Gamma_t) + \Upsilon(\Gamma_t) - \mathcal{P}(\boldsymbol{u}_t)\right) = 0. \tag{2.7}$$

Considering conservative external forces, it is possible to attribute a potential that decreases with the external energy, $\Pi(\boldsymbol{u}_t,\Gamma_t) = \Psi(\boldsymbol{u}_t,\Gamma_t) - \mathcal{P}(\boldsymbol{u}_t)$. Therefore, the rate of change of the total energy $\mathcal{E}$ can be expressed as

$$\frac{\partial \Pi(\boldsymbol{u}_t,\Gamma_t)}{\partial t} + \frac{\partial \Upsilon(\Gamma_t)}{\partial t} = 0. \tag{2.8}$$

The Griffith model posits that cracks propagate progressively through incremental extensions over time. Consequently, for an infinitesimal monotonic crack area extension $\mathrm{d}\Gamma$ along a prescribed crack path, Eq. (2.8) is rewritten as

$$\left(\frac{\partial \Pi(\boldsymbol{u}_t,\Gamma_t)}{\partial \Gamma_t} + \frac{\partial \Upsilon(\Gamma_t)}{\partial \Gamma_t}\right)\frac{\partial \Gamma_t}{\partial t} = 0. \tag{2.9}$$

By defining the energy release rate

$$\mathcal{G}_t = -\frac{\partial \Pi(\boldsymbol{u}_t,\Gamma_t)}{\partial \Gamma_t}, \tag{2.10}$$

considering Eq. (2.3), the energy balance equation becomes

$$(\mathcal{G}_t - \mathcal{G}_c)\dot{\Gamma} = 0 \tag{2.11}$$

Griffith [1] postulated that the critical force necessary for crack propagation is governed by the equilibrium between the energy released during crack growth and the energy required to form new surfaces. When $\mathcal{G}_t < \mathcal{G}_c$, the crack exhibits stable behavior, as the released energy remains below the threshold needed for propagation. The Griffith criterion thus asserts that quasi-static crack propagation initiates only when the available energy release rate reaches the critical value, i.e., $\mathcal{G}_t = \mathcal{G}_c$. In other words, crack growth becomes feasible precisely when the energy release rate equals the critical fracture energy required to create new surfaces. If the energy release rate exceeds the critical threshold ($\mathcal{G}_t > \mathcal{G}_c$), the crack becomes dynamically unstable, and classical fracture mechanics frameworks can no longer predict its evolution [47].

Chambolle, Francfort and Marigo [48] demonstrate that the Griffith fracture model aligns with the Clausius-Duhem inequality, thereby establishing the thermodynamic admissibility of fracture irreversibility and the time-dependent evolution of the crack surface. Their framework reformulates the evolution law for the crack surface using Karush-Kuhn-Tucker conditions, which

- Irreversibility condition: $\dot{\Gamma} \geq 0$,
- Griffith's criterion: $\mathcal{G}_t - \mathcal{G}_c \leq 0$,
- Energy conservation: $(\mathcal{G}_t - \mathcal{G}_c)\dot{\Gamma} = 0$.

Although the Griffith energy fracture criterion has been foundational in Linear Elastic Fracture Mechanics (LEFM), it faces limitations in predicting crack trajectories and nucleation [5]. Moreover, Griffith demonstrate that the critical tensile stress σ_{cr} required to propagate a pre-existing crack of length a in an infinite domain is expressed as

$$\sigma_{\mathrm{cr}} = \sqrt{\frac{EG_c}{\pi a}}, \tag{2.12}$$

where E is the Young's modulus. This model aligns well with experimental observations for large cracks [1], as the inverse dependence on crack length accurately captures size effects. However, for microscale or vanishingly small cracks ($a \to 0$), the predicted stress tends to infinity – a result inconsistent with real materials, which exhibit finite tensile strength governed by atomic cohesion or defect-driven failure mechanisms.

The inequality $\mathcal{G}_t - \mathcal{G}_c \leq 0$ constitutes a scalar criterion governing the temporal evolution of crack length. This constraint arises directly from Griffith's foundational assumption regarding crack topology: the model presumes a single, non-branching crack propagating along a predefined path. Crucially, Griffith's framework does not inherently predict the crack trajectory; instead, path determination requires supplementary physics-based criteria (e.g., the $\mathcal{G}$-max criterion [49] and the $\sigma_{\theta\theta}$-max criterion [50]). Furthermore, crack propagation introduces material separation, rendering the displacement field – defined in the reference configuration – to become discontinuous across the crack surfaces.

2.1.2 Modeling approaches and their numerical aspects

Based on the kinematic description of cracks in the continuum body, fracture mechanics employs two primary numerical approaches to model the failure of solids: discontinuous (discrete) and continuous methods.

In the discontinuous approach, fractures are explicitly represented as sharp interfaces where the displacement field becomes discontinuous across crack surfaces, enabling direct tracking of crack surfaces and their evolution. Key advantages include unambiguous quantification of crack growth and suitability for scenarios requiring precise fracture topology. This category includes classical frameworks such as Linear Elastic Fracture Mechanics (LEFM) [1, 51] and the Cohesive Zone Model (CZM) [52].

Numerically resolving displacement discontinuities across sharp-interface remains challenging in conventional mesh-based methods. In traditional LEFM, cracks are constrained to align with element edges, requiring frequent remeshing to accommodate topology change of the initial mesh due to crack geometric evolution [53]. CZM bypass remeshing by embedding zero-thickness interface elements along predefined potential crack paths [54–56]. These elements are governed by a traction-separation law, which enforces a critical traction threshold corresponding to the material's maximum cohesive strength, thereby simulating crack initiation and propagation. However, these approaches fail to adequately resolve stress singularities at crack tips, a limitation shared by classical C^0-continuous Finite Element Methods (FEM), where convergence rates degrade due to poor singularity representation. The Generalized FEM (GFEM) [4, 57, 58] or eXtended FEM (XFEM) [3, 59] – recently named as G/XFEM [60, 61] – overcomes these issues by embedding strong discontinuities within elements via enriched shape functions, decoupling crack geometry

from mesh topology. This approach enables fixed-mesh modeling of arbitrary crack paths while capturing tip singularities, thereby restoring optimal convergence rates [60–64].

Despite these advancements, a fundamental limitation persists across discontinuous (discrete) approaches: they require externally defined criteria to govern crack initiation, propagation direction, branching behavior, and magnitude [65, 66]. Furthermore, explicit geometric tracking of discontinuities becomes computationally prohibitive when modeling complex, arbitrary crack networks – particularly in three-dimensional analyses [67, 68]. In contrast, the continuous approach maintains displacement continuity but incorporates stress degradation to simulate material softening. In this manner, strong discontinuities are regularized as strain localization bands, avoiding explicit crack representation. This method simplifies handling complex phenomena like crack branching but approximates fracture topology.

The Continuum Damage Mechanics (CDM), pioneered by Kachanov [69], falls into the continuous approach category. This approach models the phenomenological behavior of microdefects (e.g., microcracks and microvoids) through damage variables that quantify the progressive loss of material stiffness. Unlike fracture mechanics, which explicitly addresses macroscopic cracks, CDM emphasizes the collective evolution of microscopic damage and its impact on material behavior [70]. To address mesh dependency and localization issues inherent in classical CDM [71], regularized non-local extensions have been developed. These include gradient-enhanced damage models [72] as well as gradient damage formulations [73, 74], which incorporate non-local terms to ensure numerical stability and mesh objectivity.

Still in the context of continuous approaches, two methodologies have gained prominence in recent decades: phase-field models [5] and peridynamics [75]. Phase-field models, rooted in the variational approach to brittle fracture proposed by [5], generalize Griffith's theory by simultaneously determining the displacement field and crack geometry through energy minimization. These models fall into two broad lineages: those developed within the mechanics community (e.g., [9, 29, 76]) and those arising from physics-based perspectives (e.g., [77, 78]). Both lineages employ a diffuse damage zone to represent crack evolution, inheriting core conceptual principles from Francfort and Marigo [5]. In contrast to these phase-field methodologies, peridynamics reformulates continuum mechanics by replacing partial differential equations with integral-based governing equations. This non-local framework inherently avoids spatial derivatives, allowing seamless modeling of displacement discontinuities such as cracks without supplemental criteria.

The primary limitation of continuous fracture modeling lies in its inability to fully represent true displacement discontinuities. This challenge led to the development of hybrid continuous-discontinuous approaches, which combine nonlocal damage formulations (e.g., integral or gradient-based models) to simulate progressive damage until final failure,

followed by discontinuous methods to capture discrete cracking (see, e.g., [22, 79–82]). An alternative unified framework is the Thick Level Set approach [83–85], which embeds a discontinuous crack within a continuous strain-softening zone. Despite these advances, no universally accepted criterion exists for transitioning between continuous and discontinuous representations, particularly in cases where crack-induced anisotropy dominates the fracture process.

3 PHASE-FIELD APPROACH FOR FRACTURE MODELING

The primary limitation of Griffith's theory – and other classical sharp-interface fracture models such as the cohesive zone model – stems from their reliance on an *a priori* assumption of crack topology, which underpins the concept of energy release rates. To address this constraint, Francfort and Marigo [5] proposed a reformulation of crack description in which the set of admissible cracks are considered to be an arbitrary closed subdomain of the body Ω whose dimension is not greater than $d-1$. Essentially, aside from this dimensional constraint, no assumptions are imposed on the geometry or morphology of potential cracks. This approach diverges fundamentally from classical fracture mechanics, where analyses are typically restricted to infinitesimal perturbations of preexisting crack geometries. Consequently, a generalization of the Griffith's surface energy Eq. (2.3) is achieved by

$$\mathcal{S}(\Gamma_t) = \int_{\Gamma_t} \mathcal{G}_c \mathrm{d}\mathcal{H}^{d-1}(\Gamma_t), \tag{3.1}$$

where $\mathcal{H}^{d-1}$ denotes the $d-1$-dimensional Hausdorff measure, which is equivalente to the usual surface measurement for sufficiently smooth hypersurfaces. Accordingly, the variational formulation proposed by Francfort and Marigo [5] relies on the principle of global minimality of the total energy of the cracked body, which is the sum of the strain energy, the surface crack energy and the potential energy of external forces, read as

$$\mathcal{E}(\boldsymbol{u}_t, \Gamma_t) = \int_{\Omega/\Gamma_t} \psi(\boldsymbol{\varepsilon}(\boldsymbol{u}_t))\ \mathrm{d}\Omega + \int_{\Gamma_t} \mathcal{G}_c \mathrm{d}\mathcal{H}^{d-1}(\Gamma_t) - \int_{\partial\Omega_{\boldsymbol{F}}} \bar{\boldsymbol{F}}_t \cdot \boldsymbol{u}_t\ \mathrm{d}s. \tag{3.2}$$

Minimizing the functional Eq. (3.2) yields an admissible crack set $\Gamma_t \subset \Omega$ satisfying the irreversibility condition $\dot{\Gamma} \geq 0$ and a displacement field $\boldsymbol{u}$ that fulfills Eq. (2.1) while exhibiting discontinuities across Γ_t. Griffith [1] examines the energy relationship in Eq. (2.11) under the restrictive assumption of stable crack growth ($\mathcal{G}_t = \mathcal{G}_c$), where propagation occurs as a steady, monotonic process involving only incremental extensions of preexisting cracks over time. In contrast, the variational formulation generalizes this framework by permitting brutal crack growth ($\mathcal{G}_t > \mathcal{G}_c$), enabling sudden, non-gradual propagation events. While this flexibility enhances the applicability of the model to complex fracture scenarios, such abrupt transitions inherently strain the assumptions of quasi-static equilibrium. Specifically, dynamic effects—such as those arising when a mode I crack's velocity approaches the Rayleigh wave speed—must be carefully accounted for to ensure physical fidelity.

In the variational formulation, the crack evolution—including kinking, branching, or nucleation of new cracks, as well as abrupt structural failure—is governed solely by the global energy minimization of Eq. (3.2) and the irreversibility condition. Crack nucleation in initially intact structures becomes possible even under Griffith's surface energy model

Eq. (2.3) through energy comparisons between the elastic energy of the uncracked body and the total energy of a test cracked configuration. Furthermore, the variational approach rigorously recovers Griffith's criterion when the crack path is constrained to a predefined surface.

A direct numerical implementation of the variational formulation Eq. (3.2) poses significant technical challenges due to the implicit dependence on Γ_t, which is not known *a priori* [7], i.e., the minimization of the total energy with respect to the displacement field requires prior knowledge of the crack path. To make the problem computationally tractable, Bourdin–Francfort–Marigo [6, 7, 86, 87] define a elliptic regularization of Eq. (3.2) by introducing a auxiliar continuous scalar phase-field or damage field $\phi(\boldsymbol{x})$ to the kinematics of the body, rendering the regularized total energy

$$\tilde{\mathcal{E}}(\boldsymbol{u}_t, \phi_t) = \int_\Omega \tilde{\psi}(\boldsymbol{\varepsilon}_t,\phi_t)\ \mathrm{d}\Omega + \mathcal{G}_c \int_\Omega \gamma(\phi_t,\nabla\phi_t)\ \mathrm{d}\Omega - \int_{\partial\Omega_{\boldsymbol{F}}} \bar{\boldsymbol{F}}_t \cdot \boldsymbol{u}_t\ \mathrm{d}s, \tag{3.3}$$

where $\gamma(\phi_t, \nabla\phi_t)$ is called the crack surface density function [29], responsible for approximating the set of sharp cracks Γ_t by a localized band $\Omega_\phi \subseteq \Omega$. The approximation of the discrete crack is parametrized by a small numerical parameter ℓ. The additional scalar field ϕ_t is diffuse and continuously interpolates between intact ($\phi_t = 0$) and cracked ($\phi_t = 1$) regions , such that $\phi_t(\boldsymbol{x}) = 1$ when $\boldsymbol{x} \in \Gamma_t$ and $\phi_t(\boldsymbol{x}) = 0$ otherwise. The main advantage of this two-field approach lies in its ability to represent cracks independently of mesh or geometric constraints. This enables the use of classical C^0 finite element methods to spatially discretize both displacement and scalar field.

The second integral of the Eq. (3.3) represents an approximation of the length or surface area of Γ_t if $d = 2$ or $d = 3$, respectively, such that

$$\begin{aligned} \Gamma_t &\simeq \Omega_\phi \\ \int_{\Gamma_t} \mathrm{d}\mathcal{H}^{d-1}(\Gamma_t) &\simeq \int_\Omega \gamma(\phi_t,\nabla\phi_t)\ \mathrm{d}\Omega, \end{aligned} \tag{3.4}$$

as shown Fig. 2. Furthermore, $\tilde{\psi}(\boldsymbol{\varepsilon}_t,\phi_t)$ is the degraded elastic strain energy and, due to the smeared nature of the phase-field, depends on both displacement and damage fields, read as follows

$$\tilde{\psi}(\boldsymbol{\varepsilon}_t, \phi_t) = g(\phi_t)\psi(\boldsymbol{\varepsilon}_t), \tag{3.5}$$

where $g(\phi_t)$ is responsible for the stiffness degradation such that it must be a continuous monotonically decreasing function that attends to the requirements: $g(0) = 1$ (intact state), $g(1) = 0$ (completely broken state), $g'(\phi_t) < 0$ for $\phi_t \in [0, 1]$ (force monotonically decreasing), and $g'(1) = 0$. Pham *et al.* [74] provide a detailed argumentation on these requirements. Consequently, a thermodynamically consistent material law can be obtained as

$$\tilde{\boldsymbol{\sigma}}(\boldsymbol{\varepsilon}_t, \phi_t) = \frac{\partial\tilde{\psi}(\boldsymbol{\varepsilon}_t, \phi_t)}{\partial\boldsymbol{\varepsilon}} = g(\phi_t)\frac{\partial\psi(\boldsymbol{\varepsilon}_t)}{\partial\boldsymbol{\varepsilon}}, \tag{3.6}$$

with $\tilde{\boldsymbol{\sigma}}$ being the damage-dependent stress tensor associated with $\tilde{\psi}(\boldsymbol{\varepsilon}_t, \phi_t)$.

Figure 2 – (a) Sketch of a solid body Ω with a set of internal sharp cracks Γ. (b) Representation of localized band Ω_ϕ where the diffuse damage field $\phi(\boldsymbol{x})$ approximate the internal discontinuities.

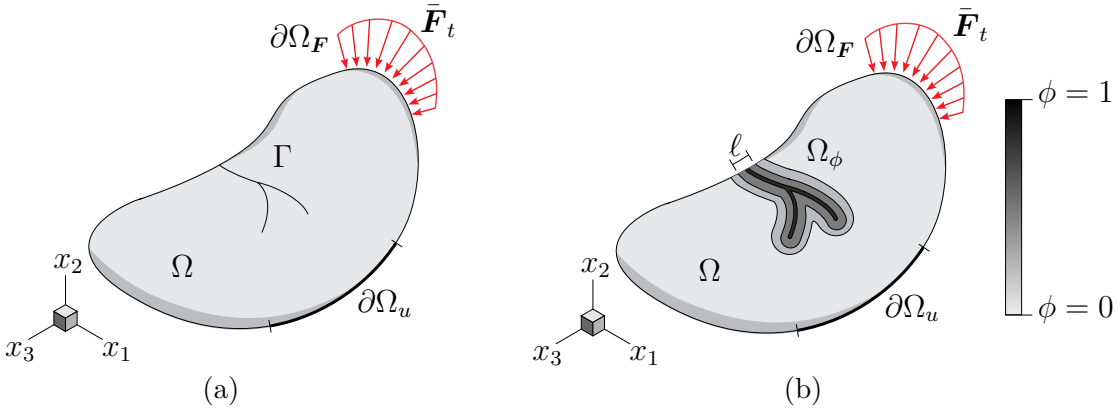

Source: The author.

Concerning the crack surface contribution to the total energy, several approaches can be found in the literature to express the regularized sharp crack topology. These approaches are discussed in detail in section 3.3, including the definition of the stiffness degradation function $g(\phi_t)$. At this point it is important to highlight the following expression as a generalization of the crack surface density function

$$\gamma(\phi_t, \nabla\phi_t) = \frac{1}{c_w}\left(\frac{w(\phi_t)}{\ell} + \ell|\nabla\phi_t|^2\right), \tag{3.7}$$

where $w(\phi_t)$ is a monotonic continuous function, called the local part of the dissipated fracture energy density [74], that must fulfill the following properties: $w(0) = 0$, $w(1) = 1$ and $w'(\phi_t) \geq 0$ for $\phi_t \in [0,\, 1]$. Using the notion of Γ-convergence, the normalization constant $c_w = \int_0^1 \sqrt{w(z)}\, \mathrm{d}z$ is introduced in order to ensure that when $\ell \to 0$ a relationship between Eq. (3.3) and Eq. (3.2) is established [88–90].

3.1 Incremental Variational Formulation

Assume a quasi-static loading process at every pseudo-time t_n where $n \in I_N$, with $I_N := \{i \in \mathbb{N} : 1 < i \leq N\}$ and N representing the number of discrete pseudo-time steps. Given a load step $n \geq 1$, the state of the system described by $(\boldsymbol{u}, \phi)$ is represented by the solution of the following minimization problem

$$\arg\min\{\tilde{\mathcal{E}}(\boldsymbol{u}, \phi) \mid \boldsymbol{u} \in \boldsymbol{\mathcal{C}}_n,\ \phi \in \mathcal{D}_{n-1}\}, \tag{3.8}$$

which is built into the definition of the kinematic admissible displacement and damage spaces $\boldsymbol{\mathcal{C}}_n$ and $\mathcal{D}_{n-1}$, respectively, given by

$$\begin{aligned} \boldsymbol{\mathcal{C}}_n &:= \left\{\boldsymbol{u} \in \mathbf{H}^1(\Omega) \mid \boldsymbol{u} = \bar{\boldsymbol{u}}_n \text{ on } \partial\Omega_u\right\} \\ \mathcal{D}_{n-1} &:= \left\{\phi \in H^1(\Omega) \mid \phi \in [0,\, 1],\ \phi \geq \phi_{n-1} \text{ in } \Omega\right\}. \end{aligned} \tag{3.9}$$

with $\mathbf{H}^1(\Omega) = H^1(\Omega, \mathbb{R}^d)$ and $H^1(\Omega)$ being the Sobolev space of functions with square integrable derivatives. Observe that $\phi \geq \phi_{n-1}$ prevents self-healing of the damage field, ensuring that the crack path is irreversible.

Assuming that the displacement field $\boldsymbol{u}$ and the damage field ϕ are sufficiently regular in time and space, the incremental variational formulation of the coupled two-field phase-field problem can be expressed in terms of the following conditions:

1. **Irreversibility**: the damage field ϕ is a non-decreasing function of time

$$\phi_n \geq \phi_{n-1}. \tag{3.10}$$

2. **First-order stability**: considering the virtual admissible function space $\boldsymbol{\mathcal{C}}_0 := \left\{\delta\boldsymbol{u} \in \mathbf{H}^1(\Omega) \mid \delta\boldsymbol{u} = \mathbf{0} \text{ on } \partial\Omega_u\right\}$, the incremental energy variation is non-negative for any arbitrary admissible virtual displacement and damage fields evolution

$$\begin{cases} \tilde{\mathcal{E}}_{\boldsymbol{u}}(\boldsymbol{u}, \phi; \delta\boldsymbol{u}) = \mathbf{0}, & \forall\ \delta\boldsymbol{u} \in \boldsymbol{\mathcal{C}}_0, \\ \tilde{\mathcal{E}}_{\phi}(\boldsymbol{u}, \phi; \delta\phi - \phi) \geq 0, & \forall\ \delta\phi \in \mathcal{D}_{n-1}. \end{cases} \tag{3.11}$$

   Herein $\tilde{\mathcal{E}}_{\boldsymbol{u}}$ and $\tilde{\mathcal{E}}_{\phi}$ denotes the Gateaux derivatives of the energy functional with respect to $\boldsymbol{u}$ and ϕ, respectively, given by

$$\begin{aligned} \tilde{\mathcal{E}}_{\boldsymbol{u}}(\boldsymbol{u}, \phi; \delta\boldsymbol{u}) &= \int_\Omega g(\phi) \left(\frac{\partial \psi(\boldsymbol{\varepsilon})}{\partial \boldsymbol{\varepsilon}} : \frac{\partial \boldsymbol{\varepsilon}(\boldsymbol{u})}{\partial \boldsymbol{u}} \delta\boldsymbol{u} \right) \mathrm{d}\Omega - \int_{\partial\Omega_{\boldsymbol{F}}} \bar{\boldsymbol{F}}_n \cdot \delta\boldsymbol{u}\ \mathrm{d}s, \\ \tilde{\mathcal{E}}_{\phi}(\boldsymbol{u}, \phi; \delta\phi) &= \int_\Omega g'(\phi)\psi(\boldsymbol{\varepsilon})\delta\phi\ \mathrm{d}\Omega + \frac{\mathcal{G}_c}{c_w} \int_\Omega \left(\frac{w'(\phi)}{\ell}\delta\phi + 2\ell \nabla\phi \cdot \nabla\delta\phi \right) \mathrm{d}\Omega. \end{aligned} \tag{3.12}$$

3. **Energy conservation**: The energy dissipated within the system during the time interval Δt_n is solely attributable to crack propagation

$$\dot{\tilde{\mathcal{E}}}_n = \int_{\partial\Omega_u} (\tilde{\boldsymbol{\sigma}} \cdot \boldsymbol{n}) \cdot \dot{\bar{\boldsymbol{u}}}_n\ \mathrm{d}s - \int_{\partial\Omega_{\boldsymbol{F}}} \dot{\bar{\boldsymbol{F}}}_n \cdot \boldsymbol{u}\ \mathrm{d}s, \tag{3.13}$$

   where $\boldsymbol{n}$ is the outward normal vector to the boundary and $\dot{(\,)}_n = ((\,)_n - (\,)_{n-1})/\Delta t_n$.

3.2 Local governing equations

The governing equations of the elastic problem are derived by applying the divergence theorem to the Gâteaux derivative of the total energy with respect to the displacement field $\boldsymbol{u}$, illustrated in Eq. (3.12), yielding

$$-\int_\Omega \nabla \cdot \tilde{\boldsymbol{\sigma}} \cdot \delta\boldsymbol{u}\ \mathrm{d}\Omega + \int_{\partial\Omega_{\boldsymbol{F}}} \left(\tilde{\boldsymbol{\sigma}} \cdot \boldsymbol{n} - \bar{\boldsymbol{F}} \right) \cdot \delta\boldsymbol{u}\ \mathrm{d}s = 0, \tag{3.14}$$

due to arbitrariness of $\delta\boldsymbol{u}$ we obtain

$$\begin{aligned} \nabla \cdot \tilde{\boldsymbol{\sigma}} &= 0 \qquad \text{in } \Omega, \\ \tilde{\boldsymbol{\sigma}} \cdot \boldsymbol{n} &= \bar{\boldsymbol{F}}_n \quad \text{on } \partial\Omega_{\boldsymbol{F}}, \\ \boldsymbol{u} &= \bar{\boldsymbol{u}}_n \quad \text{on } \partial\Omega_u. \end{aligned} \tag{3.15}$$

Unlike the classical elastic equation Eq. (2.1), the stress tensor $\tilde{\boldsymbol{\sigma}}$ in this formulation is damage-dependent, see Eq. (3.6).

The governing equations of damage evolution is deduced with the same approach, but now considering the Gâteaux derivative of the total energy with respect to the damage field ϕ, illustrated in Eq. (3.12), yielding

$$\int_\Omega \left(g'(\phi)\psi(\boldsymbol{\varepsilon}) + \frac{2\mathcal{G}_c}{c_w \ell} \left(\frac{w'(\phi)}{2} - \ell^2 \nabla \cdot \nabla \phi \right) \right) \delta\phi \, \mathrm{d}\Omega + \int_{\partial\Omega} \frac{2\ell\mathcal{G}_c}{c_w} \left(\nabla\phi \cdot \boldsymbol{n} \right) \delta\phi \, \mathrm{d}s \geq 0, \quad (3.16)$$

due to the arbitrariness of $\delta\phi$ we obtain the strong form, which serves as the local damage criterion at a particular material point,

$$\begin{aligned} Y - \nabla \cdot \boldsymbol{q} &\leq 0 \quad \text{in } \Omega, \\ \boldsymbol{q} \cdot \boldsymbol{n} &\geq 0 \quad \text{on } \partial\Omega, \end{aligned} \quad (3.17)$$

with the following dual variables

$$\begin{aligned} Y &= g'(\phi)\psi(\boldsymbol{\varepsilon}) + \frac{\mathcal{G}_c w'(\phi)}{c_w \ell}, \\ \boldsymbol{q} &= \frac{2\ell\mathcal{G}_c}{c_w} \nabla\phi, \end{aligned} \quad (3.18)$$

where Y represents the energy release rate density with respect to damage and $\boldsymbol{q}$ the damage flux vector, see [91]. The global energy balance Eq. (3.3) leads to the following consistency condition

$$\begin{aligned} \left(Y - \nabla \cdot \boldsymbol{q} \right) \dot{\phi} &= 0 \quad \text{in } \Omega, \\ \left(\boldsymbol{q} \cdot \boldsymbol{n} \right) \dot{\phi} &= 0 \quad \text{on } \partial\Omega, \end{aligned} \quad (3.19)$$

where $\dot{\phi}$ is the time derivative of the damage field, which enforces the condition that the damage process is irreversible, i.e., $\phi_n \geq \phi_{n-1}$. Thus, the damage evolution law can be expressed in terms of Karush-Kuhn-Tucker (KKT) conditions, given by

- Irreversibility condition: $\dot{\phi} \geq 0$,
- Damage criterion: $Y - \nabla \cdot \boldsymbol{q} \leq 0$,
- Energy conservation: $\left(Y - \nabla \cdot \boldsymbol{q} \right) \dot{\phi} = 0$.

Hence damage growth is possible until a certain non-local threshold is reached.

Considering a homogeneous damage evolution process (such that $\nabla \cdot \boldsymbol{q} = 0$) and an undamaged region of the domain Ω ($\phi = 0$), the consistency condition Eq. (3.19) requires

$$Y = 0 \quad \Rightarrow \quad g'(\phi)\psi(\boldsymbol{\varepsilon}) + \frac{\mathcal{G}_c w'(\phi)}{c_w \ell} = 0, \quad (3.20)$$

which when written in the stress-space using Eq. (3.6) leads to the following condition

$$-\frac{1}{2} s'(\phi) \boldsymbol{\sigma} : \mathfrak{D} : \boldsymbol{\sigma} + \frac{\mathcal{G}_c w'(\phi)}{c_w \ell} = 0, \quad (3.21)$$

where $\mathfrak{D} = \mathfrak{C}^{-1}$, which is the compliance tensor associated with the elastic stiffness tensor $\mathfrak{C}$, and the monotonically increasing function $s(\phi) = g^{-1}(\phi)$.

To elucidate this behavior, consider Eq. (3.21) applied in a homogeneous uniaxial traction test under displacement-controlled boundary conditions, which leads to the following expression

$$\frac{s'(\phi)\sigma^2}{2E} - \frac{\mathcal{G}_c w'(\phi)}{c_w \ell} = 0. \tag{3.22}$$

In the context of strain-softening - which ensures that the elastic domain in stress space is a decreasing function as damage evolves - [74] shows that the evolution process exhibits two regimes:

- **Elastic phase**: The material exhibits a linear elastic behavior, limited by the critical stress σ_c, beyond which the damage field initiates:

$$\sigma_c = \sqrt{\mathrm{w}_1 \frac{w'(0)}{s'(0)}} \tag{3.23}$$

  where $\mathrm{w}_1 = 2E\mathcal{G}_c/c_w\ell$.

- **Softening phase**: Where the ratio $w'(\phi)/s'(\phi)$ must be a monotonic increasing function. Thus, stress decreases with displacement, leading to a peak stress σ_m representing the maximum stress the material can sustain before failure:

$$\sigma_m = \max_{\beta \in [0,1]} \sqrt{\mathrm{w}_1 \frac{w'(\beta)}{s'(\beta)}}. \tag{3.24}$$

3.3 Phase-field models

The stiffness degradation function $g(\phi)$ along with the damage dissipation function $w(\phi)$ plays an important role for ensuring certain constitutive properties which characterize the regularized total energy described in the Eq. (3.3). The material and structural behaviors could be quantitatively or even qualitatively different depending on the choice of these functions. Among widely used phase-field models for damage evolution, the `AT1` and `AT2` models are particularly prominent. `AT` refer to *Ambrosio–Tortorelli* [88]. Introduced by [74], the `AT1` model is defined as

$$g(\phi) = (1-\phi)^2, \quad w(\phi) = \phi. \tag{3.25}$$

This model is notable due to its important property for modeling brittle fracture: the damage field ϕ does not evolve until the material reaches the critical stress, i.e., the material exhibits a linear elastic behavior before the critical strength. Therefore, a strain-softening behavior is observed for $\phi \in [0, 1]$, which based on Eq. (3.23) implies that

$$\sigma_m = \sigma_c = \sqrt{\frac{\mathrm{w}_1}{2}} = \sqrt{\frac{E\mathcal{G}_c}{c_w \ell}}. \tag{3.26}$$

Conversely, the AT2 model, proposed by [6] and defined as follows

$$g(\phi) = (1-\phi)^2, \quad w(\phi) = \phi^2, \tag{3.27}$$

leads to a damage evolution in the whole computation domain as soon as the material starts to be loaded, i.e., there is no prior linear elastic behavior. Therefore, $\sigma_c = 0$ and the strain-softening behavior is verified only for $\phi \in [\frac{1}{4}, 1]$, where at $\phi = \frac{1}{4}$ the material reaches the peak strength [74], given by

$$\sigma_m = \frac{3\sqrt{6}}{16}\sqrt{\frac{\mathrm{w}_1}{2}} = \sqrt{\frac{27E\mathcal{G}_c}{128c_w\ell}}. \tag{3.28}$$

Equations (3.26) and (3.28) demonstrate that the peak strength σ_m depends intrinsically on the characteristic length ℓ. This functional relationship establishes ℓ as a material parameter, not merely a numerical one, since σ_m, as a material property, must arise from the physical attributes of the material itself. Treating ℓ as a numerical parameter would inappropriately link the material's strength to computational mesh resolution, which lacks physical basis.

Despite their widespread adoption in computational mechanics, variational phase-field models such as AT1/2 exhibit fundamental limitations in describing fracture nucleation accurately. As demonstrated in [92–94], these models can only account for two of the three intrinsic macroscopic material properties that govern fracture nucleation in elastic brittle materials: elasticity and fracture toughness. Critically, they fail to properly represent the material's strength as an independent macroscopic property. Instead, the strength surfaces predicted by these models are inherently subordinate to the elastic energy and toughness, rather than being truly independent material characteristics as observed experimentally. This fundamental shortcoming means that while AT1/2 models may provide reasonable approximations in specific loading scenarios where only a limited portion of the strength surface is relevant, they cannot serve as general descriptors of fracture nucleation across arbitrary stress states. The dependence of critical stress on the regularization parameter ℓ (as shown in the equations above) further illustrates this limitation, as the material strength becomes artificially coupled to the numerical discretization rather than being determined solely by intrinsic material properties.

In AT1/2 models, ℓ is inversely determined using the material failure strength f_t (via Equations (3.26) and (3.28)). This approach results in damage zones that are disproportionately large relative to the computational domain size [95, 96]. Although reducing ℓ enhances the numerical accuracy of crack topology, it simultaneously causes the predicted peak load to diverge from experimental results [95]. To overcome this issue, [97] introduced the phase-field regularized cohesive zone model (CZM), which incorporates two key components:

- A generalized stiffness degradation function (Motivated by [98]):

$$g(\phi) = \frac{(1-\phi)^p}{(1-\phi)^p + Q(\phi)}, \qquad Q(\phi) = a_1\phi + a_1a_2\phi^2 + a_1a_2a_3\phi^3 + \dots, \tag{3.29}$$

  where $p > 0$ and $a_i > 0$ ($i = 1, 2, 3, \dots$) are coefficients calibrated to represent material softening curves. Oberve that by considering $p = 2$, $a_1 = 2$, $a_2 = -\frac{1}{2}$ and $a_3 = 0$ the stiffness degradation function for `AT1/2` models is recovered.

- A generic damage dissipation function:

$$w(\phi) = \xi\phi + (1-\xi)\phi^2, \tag{3.30}$$

  where $\xi \in [0, 2]$, which allows to interpolate between the `AT1` ($\xi = 1$) and `AT2` ($\xi = 0$) models.

Upon these considerations, [97] derived a model that contains the key features of `AT1`: a elastic phase prior to the peak stress σ_m, and a strain-softening behavior for $\phi \in [0, 1]$, which based on Eq. (3.23) implies that

$$\sigma_m = \sigma_c = \sqrt{\mathrm{w}_1 \frac{w'(0)}{s'(0)}} = \sqrt{\mathrm{w}_1 \frac{\xi}{a_1}} = \sqrt{\frac{2E\mathcal{G}_c}{c_w\ell}\frac{\xi}{a_1}}. \tag{3.31}$$

Irreversibility of the damage process is ensured for general softening laws by setting $\xi = 2$ [97], which leads to $w(\phi) = 2\phi - \phi^2$. Defining $\sigma_m = f_t$ in Eq. (3.31), we obtain

$$a_1 = \frac{4E\mathcal{G}_c}{c_w\ell f_t^2} = \frac{4\ell_{\mathrm{ch}}}{c_w\ell}, \tag{3.32}$$

where $\ell_{\mathrm{ch}} = E\mathcal{G}_c/f_t^2$ corresponds to the characteristic length of the fracture process zone [54], also known as Irwin's characteristic length [97]. This formulation embeds both material properties and the length scale parameter into the parameter a_1, ensuring a length-scale-insensitive global response as long as the sharp crack topology is well-resolved by Eq. (3.4) [99]. According to [100], the $g(\phi)$ function must be convex to ensure local stability. To satisfy this requirement, [99] demonstrate that $a_1 \geq \frac{3}{2}$, which constrains $\ell \leq 8\ell_{\mathrm{ch}}/3\pi \approx 0.85\ell_{ch}$. However, practical resolution of the regularized crack topology Eq. (3.4) demands $\ell \ll \ell_{ch}$, establishing the condition $\ell \leq 0.85\ell_{\mathrm{ch}}$ as an upper bound.

The length-scale independence of the peak stress σ_m enables the definition of a crack-opening displacement function and softening law free from explicit ℓ-dependence [97]. Consequently, the framework naturally recovers a traction-separation law akin to Barenblatt's cohesive zone model [54, 101]. Aiming to estabilish a general softening law, [97] determined the following expressions for the remaining parameters

$$\begin{aligned} a_2 &= 2\left(-2k_0\frac{\mathcal{G}_c}{f_t^2}\right)^{\frac{2}{3}} - \left(p + \frac{1}{2}\right), \\ a_3 &= \begin{cases} 0 & p > 2, \\ \dfrac{1}{a_2}\left[\dfrac{1}{8}\left(\dfrac{\delta_c f_t}{\mathcal{G}_c}\right)^2 - (1+a_2)\right] & p = 2, \end{cases} \end{aligned} \tag{3.33}$$

where k_0 is the initial stiffness of the softening law, δ_c is the ultimate crack opening displacement. Observe that a_2 and a_3 are only dependent of material properties, allowing to calibrate them to reproduce a specific softening curves, as follows

1. Linear softening: $p = 2$, $a_2 = -\frac{1}{2}$, $a_3 = 0$

$$\sigma(\delta) = f_t \max\left(1 - \frac{f_t}{2\mathcal{G}_c}\delta, 0\right), \quad k_0 = -\frac{f_t^2}{2\mathcal{G}_c}, \quad \delta_c = \frac{2\mathcal{G}_c}{f_t}. \tag{3.34}$$

2. Exponential softening: $p = \frac{5}{2}$, $a_2 = 2^{\frac{5}{3}} - 3$, $a_3 = 0$

$$\sigma(\delta) = f_t \exp\left(-\frac{f_t}{\mathcal{G}_c}\delta\right), \quad k_0 = -\frac{f_t^2}{\mathcal{G}_c}, \quad \delta_c = +\infty. \tag{3.35}$$

3. Hyperbolic softening: $p = 4$, $a_2 = 2^{\frac{7}{3}} - \frac{9}{2}$, $a_3 = 0$

$$\sigma(\delta) = f_t \left(1 + \frac{f_t}{\mathcal{G}_c}\delta\right)^{-2}, \quad k_0 = -\frac{2f_t^2}{\mathcal{G}_c}, \quad \delta_c = +\infty. \tag{3.36}$$

4. Cornelissen, Hordijk and Reinhardt [102] softening curve for normal concrete: $p = 2$, $a_2 = 1.3868$, $a_3 = 0.6567$

$$\begin{aligned} \sigma(\delta) &= f_t \left((1 + \eta_1^3 r^3)\exp(-\eta_2 r) - r(1 + \eta_1^3)\exp(-n_2)\right), \\ k_0 &= -\frac{1.3546 f_t^2}{\mathcal{G}_c}, \quad \delta_c = 5.1361\frac{\mathcal{G}_c}{f_t}, \end{aligned} \tag{3.37}$$

   where $r = \delta/\delta_c$ is the normalized crack opening displacement, and $\eta_1 = 3.0$ and $\eta_1 = 6.93$ are the parameters that control the shape of the softening curve.

Here $\sigma(\delta)$ is the traction accross the crack opening displacement δ. Therefore, while the `AT1/2` models are limited to brittle and quasi-brittle fracture, the CZM model can be applied to both brittle and cohesive fracture.

Despite the significant improvements offered by the `CZM` model over standard `AT1/2` formulations, it is important to acknowledge that this approach, like other existing cohesive models of fracture [52], still faces fundamental limitations in describing fracture nucleation. While these cohesive models do predict that nucleation does not occur unless a strength surface criterion is violated, they cannot account for an arbitrary strength surface as observed in real materials [94].

As established in Chapter 3, the connection between phase-field damage model and fracture can be rigorously formulated through Γ-convergence theory. Within this framework, the damage dissipation energy Eq. (3.7) serves as a regularized approximation of the classical Griffith crack surface energy functional. Therefore, the effective fracture toughness $\mathcal{G}_c$ — defined as the energy required to form a unit area of Griffith crack —

can be quantified by analyzing the energy dissipation associated with the evolution of an optimal damage profile ϕ_* during a uniaxial tensile failure process [74]. This optimal profile corresponds to the damage distribution at fracture in a uniaxially loaded bar centered at $x = 0$. The governing equation for ϕ_* is derived by enforcing the consistency condition Eq. (3.19) at the critical fracture instant, where the stress vanishes, i.e $\sigma = 0$, due to complete loss of material integrity. Mathematically, the profile ϕ_* satisfies the boundary value problem defined by the following differential equation

$$\frac{1}{2}w'(\phi_*(x)) - \ell^2\phi_*''(x) = 0, \quad \text{for } x \in (-D,\, D), \tag{3.38}$$

with the boundary conditions $\phi_*(\pm D) = 0$ and $\phi_*'(\pm D) = 0$ where D measures the half-damage band or the support of the damage field where $\phi > 0$. Readers are referred to [74,97] for a detailed derivation. In this context, each phase-field model can be characterized by the following optimal damage profile

- `AT1` [74]:

$$\phi_*(x) = \left(1 - \frac{|x|}{2\ell}\right)^2, \quad D = 2\ell, \quad c_w = \frac{8}{3}. \tag{3.39}$$

- `AT2` [6]:

$$\phi_*(x) = \exp\left(-\frac{|x|}{\ell}\right), \quad D = \pm\infty, \quad c_w = 2. \tag{3.40}$$

- `CZM` [97]:

$$\phi_*(x) = 1 - \sin\left(\frac{|x|}{\ell}\right), \quad D = \frac{\pi}{2}\ell, \quad c_w = \pi. \tag{3.41}$$

These damage profiles are illustrated in Fig. 3. Observe that the `AT1` and `CZM` models are limited to a finite support, while the `AT2` model has an infinite support. The parameter c_w is a constant that depends on the phase-field model and is used to normalize the energy dissipation function.

It is worth noting there are several other definitions of $g(\phi)$ and $w(\phi)$ available in the literature, see e.g., [10, 103–105]. The last note concerns the boundedness of $\phi \in$ [0,1]. Among all described phase-field models, only the `AT2` intrinsically remains in the admissible range, requiring explicit impose the boundedness condition for `AT1` and `CZM`. A few options are available to deal with this constraint, e.g., using a bounded-constrain quadratic optimization solver [31, 106] or the penalization approach suggested by Gerasimov and Lorenzis [107]. Although the non-negative damage field can be captured by `AT1` and `CZM` models (see section 3.4 for further details), only the `CZM` rarely violate the condition $\phi \leq 1$ [95]. Hence, in this work, the analyzes are restricted to `AT2` and `CZM` models, and no special treatment is applied to deal with the boundedness condition. Tab. 1 presents a summary of the described phase field models and their properties

Figure 3 – Optimal damage profiles $\phi_*(x)$ for the `AT1`, `AT2`, and `CZM` models.

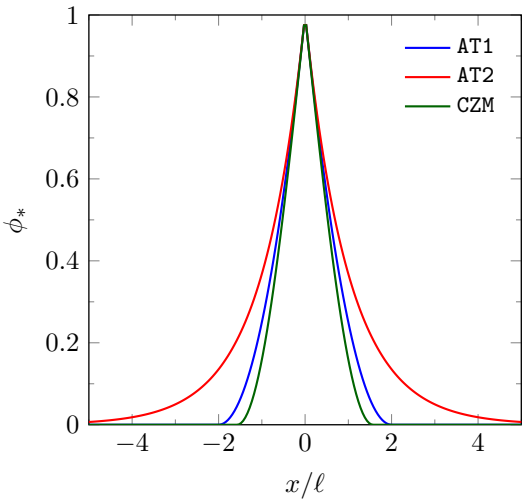

Source: The author.

Table 1 – Summary of phase-field models used in the literature for brittle and quasi-brittle fracture analysis.

Model	$g(\phi)$	$w(\phi)$	c_w	ℓ	$\phi \in [0,1]$
`AT1`	$(1-\phi)^2$	ϕ	$\frac{8}{3}$	$\frac{3\ell_{\text{ch}}}{8}$	no
`AT2`		ϕ^2	2	$\frac{27\ell_{\text{ch}}}{256}$	yes
`CZM`	$\frac{(1-\phi)^p}{(1-\phi)^p + Q(\phi)}$	$2\phi - \phi^2$	π	$\leq \frac{8\ell_{\text{ch}}}{3\pi}$	no

Source: The author.

3.4 Treating the irreversibility constraint

An important aspect of phase-field damage models is ensuring that no crack healing occurs between loading steps, as is represented by the variational inequality $\tilde{\mathcal{E}}_\phi \geq 0$ in the Eq. (3.11). To achieve this, several special solution algorithms are available in the literature, e.g, penalization [34, 107], bound-constrained optimization solver [31, 35, 106], active-set Newton method [19, 108], and the augmented Lagrangian method [98, 109]. A widely adopted approach is to use a monotonic history field $\mathcal{H}$ to implicitly impose the irreversibility constraint. Miehe, Hofacker and Welschinger [30] proved that such an approach is thermodynamically consistent, leading to a phase-field evolution driven by the maximum accumulated strain energy within the loading history, denoted as

$$\mathcal{H}_n(\boldsymbol{x}) := \max_{n\geq 1}\{\mathcal{H}_{n-1},\, \bar{\mathcal{H}}\}, \tag{3.42}$$

where $\bar{\mathcal{H}}$ is called *driving force*. However, such an approximation is no longer variationally consistent, resulting in a modification of the first variation of the Eq. (3.3) with respect to ϕ to

$$\tilde{\mathcal{E}}_\phi(\boldsymbol{u},\phi,\delta\phi) = \int_\Omega g'(\phi)\mathcal{H}_n\delta\phi \,\mathrm{d}\Omega + \frac{\mathcal{G}_c}{c_w}\int_{\Gamma_\phi}\left(\frac{w'(\phi)}{\ell}\delta\phi + 2\ell\nabla\phi\cdot\nabla\delta\phi\right)\mathrm{d}\Gamma_\phi. \tag{3.43}$$

Now, the solution $(\boldsymbol{u},\phi) \in \mathbf{V}_n \times \mathcal{D}_{n-1}$ at loading step $n \geq 1$ must satisfy the following system of equations

$$\begin{aligned} \mathcal{E}_{\boldsymbol{u}}(\boldsymbol{u},\phi,\delta\boldsymbol{u}) &= 0, \quad \forall\ \delta\boldsymbol{u} \in \mathbf{V}_0 \\ \tilde{\mathcal{E}}_\phi(\boldsymbol{u},\phi,\delta\phi) &= 0, \quad \forall\ \delta\phi \in \mathcal{D}_0. \end{aligned} \tag{3.44}$$

The driving force variable, $\bar{\mathcal{H}}$, dictated how the phase-field damage evolves. In simple cases, it can be computed as the non-damaged strain energy density $\psi(\boldsymbol{\varepsilon})$, rendering an isotropic deterioration where the fracture behavior is identical under tensile or compressive stress, as is expressed by energy density function in Eq. (3.5) and stress field in Eq. (3.6). In such approach, the driving force is given by

$$\bar{\mathcal{H}} = \psi(\boldsymbol{\varepsilon}). \tag{3.45}$$

However, this approach is not suitable for modeling crack propagation under compression, as it does not account for the anisotropic nature of fracture. To address this limitation, a additive decomposition of the strain energy density function is employed, such that

$$\psi(\boldsymbol{\varepsilon}) = \psi^+(\boldsymbol{\varepsilon}) + \psi^-(\boldsymbol{\varepsilon}), \tag{3.46}$$

with $\psi^+(\boldsymbol{\varepsilon})$ and $\psi^-(\boldsymbol{\varepsilon})$ being the strain energy density of the tensile and compressive parts of $\psi(\boldsymbol{\varepsilon})$, respectively. Under this decomposition, an anisotropic model is obtained, where the degradation function $g(\phi)$ is applied only to the tensile part of the strain energy, modifying the Eq. (3.5) to

$$\tilde{\psi}(\boldsymbol{\varepsilon},\phi) = g(\phi)\psi^+(\boldsymbol{\varepsilon}) + \psi^-(\boldsymbol{\varepsilon}), \tag{3.47}$$

rendering the stress field

$$\tilde{\boldsymbol{\sigma}}(\boldsymbol{\varepsilon},\phi) = \frac{\partial\tilde{\psi}(\boldsymbol{\varepsilon},\phi)}{\partial\boldsymbol{\varepsilon}} = g(\phi)\frac{\partial\psi^+(\boldsymbol{\varepsilon})}{\partial\boldsymbol{\varepsilon}} + \frac{\partial\psi^-(\boldsymbol{\varepsilon})}{\partial\boldsymbol{\varepsilon}}, \tag{3.48}$$

and the driving force

$$\bar{\mathcal{H}} = \psi^+(\boldsymbol{\varepsilon}). \tag{3.49}$$

This results in a more accurate representation of crack propagation behavior under different loading conditions.

Several anisotropic models are available in the literature, e.g., [30,31,99,110]. Amor, Marigo and Maurini [31] proposed a decomposition of the strain energy density function

based on the volumetric and deviatoric contributions, where the positive and negative parts of the strain energy density are given by

$$\begin{aligned}\psi^{+}(\boldsymbol{\varepsilon}) &= \frac{1}{2}K_d \left\langle \mathrm{tr}(\boldsymbol{\varepsilon})\right\rangle_{+}^{2} + \mu\left(\boldsymbol{\varepsilon}^{\mathrm{dev}} : \boldsymbol{\varepsilon}^{\mathrm{dev}}\right),\\ \psi^{-}(\boldsymbol{\varepsilon}) &= \frac{1}{2}K_d \left\langle \mathrm{tr}(\boldsymbol{\varepsilon})\right\rangle_{-}^{2},\end{aligned} \tag{3.50}$$

where $\langle a\rangle_{\pm} = (|a| \pm a)/2$, $K_d = \lambda + \dfrac{2\mu}{d}$ denotes the bulk modulus in d-dimensional space, and

$$\boldsymbol{\varepsilon}^{\mathrm{dev}} = \boldsymbol{\varepsilon} - \frac{1}{3}\mathrm{tr}(\boldsymbol{\varepsilon})\mathbf{I}, \tag{3.51}$$

with $\mathbf{I}$ being the identity tensor.

This approaches has been shown to be effective in preventing crack propagation under compressive stresses, see [31,111]. Additionally, [31] highlighted that this formulation is also able to prevent crack face penetration in case of crack closure.

Miehe, Hofacker and Welschinger [30] proposed a similar approach, but a spectral decomposition is built in terms of the strain tensor in its principal orientation $\boldsymbol{\varepsilon} = \sum_{i=1}^{3} \bar{\varepsilon}_i \mathbf{n}_i \otimes \mathbf{n}_i$, with $\bar{\varepsilon}_i$ and $\mathbf{n}_i$ being the principal strains and principal strain directions, respectively. Then, the strain energy decomposition is denoted as

$$\psi^{\pm}(\bar{\boldsymbol{\varepsilon}}) = \frac{1}{2}\lambda \left\langle \sum_{i=1}^{3} \bar{\varepsilon}_i \right\rangle_{\pm}^{2} + \mu \sum_{i=1}^{3} \langle \bar{\varepsilon}_i \rangle_{\pm}^{2}. \tag{3.52}$$

Then, the degraded strain energy density function defined in terms of principal strains is given by

$$\tilde{\psi}(\bar{\boldsymbol{\varepsilon}}, \phi) = \frac{1}{2}\lambda \tilde{g}(\phi, \sum_{i=1}^{3} \bar{\varepsilon}_i) \left(\sum_{i=1}^{3} \bar{\varepsilon}_i \right)^{2} + \mu \sum_{i=1}^{3} \tilde{g}(\phi, \bar{\varepsilon}_i) \bar{\varepsilon}_i^{2}, \tag{3.53}$$

where $\tilde{g}(\phi, \beta) = (1 - H(\beta)\phi)^2$ is a degradation function that depends on the phase-field and the strain, with $H(\beta)$ being the Heaviside function, i.e., $H(\beta) = 1$ if $\beta \geq 0$ and $H(\beta) = 0$ if $\beta < 0$. The degraded stress field is then defined as

$$\tilde{\boldsymbol{\sigma}}(\bar{\boldsymbol{\varepsilon}}, \phi) = \frac{\partial \tilde{\psi}(\bar{\boldsymbol{\varepsilon}}, \phi)}{\partial \boldsymbol{\varepsilon}} = \frac{\partial \tilde{\psi}(\bar{\boldsymbol{\varepsilon}}, \phi)}{\partial \bar{\boldsymbol{\varepsilon}}} \frac{\partial \bar{\boldsymbol{\varepsilon}}}{\partial \boldsymbol{\varepsilon}} = \bar{\boldsymbol{\sigma}}^{T}(\bar{\boldsymbol{\varepsilon}}, \phi) \frac{\partial \bar{\boldsymbol{\varepsilon}}}{\partial \boldsymbol{\varepsilon}}, \tag{3.54}$$

with $\bar{\boldsymbol{\sigma}}$ being the stress field defined in the principal orientation, such that

$$\bar{\boldsymbol{\sigma}}(\bar{\boldsymbol{\varepsilon}}, \phi) = \mathbf{L}(\bar{\boldsymbol{\varepsilon}}, \phi)\bar{\boldsymbol{\varepsilon}}, \tag{3.55}$$

where

$$\mathbf{L}_{ij} = \lambda \tilde{g}(\phi, \sum_{k=1}^{3} \bar{\varepsilon}_k)_{ij} + 2\mu \tilde{g}(\phi, \bar{\varepsilon}_j)\delta_{ij}. \tag{3.56}$$

To define the stiffness matrix, it is required to compute the derivative of the stress field with respect to the strain field, which is given by

$$\begin{aligned}\mathfrak{C} = \frac{\partial \bar{\boldsymbol{\sigma}}(\bar{\boldsymbol{\varepsilon}}, \phi)}{\partial \boldsymbol{\varepsilon}} &= \left(\frac{\partial \bar{\boldsymbol{\varepsilon}}}{\partial \boldsymbol{\varepsilon}}\right)^T \mathbf{L} \frac{\partial \bar{\boldsymbol{\varepsilon}}}{\partial \boldsymbol{\varepsilon}} + \bar{\boldsymbol{\sigma}}^T(\bar{\boldsymbol{\varepsilon}}, \phi) \frac{\partial^2 \bar{\boldsymbol{\varepsilon}}}{\partial \boldsymbol{\varepsilon}^2} \\ &= \left(\frac{\partial \bar{\boldsymbol{\varepsilon}}}{\partial \boldsymbol{\varepsilon}}\right)^T \mathbf{L} \frac{\partial \bar{\boldsymbol{\varepsilon}}}{\partial \boldsymbol{\varepsilon}} + \sum_{i=1}^{3} \bar{\sigma}_i \frac{\partial^2 \bar{\varepsilon}_i}{\partial \boldsymbol{\varepsilon}^2}\end{aligned} \tag{3.57}$$

To compute the derivatives of the principal strains with respect to the strain field we can take advantage of the closed form solution of the eigenvalue problem for the strain tensor $\boldsymbol{\varepsilon}$, which for 2D problems is given by

$$\begin{aligned}\bar{\varepsilon}_{1,2} &= \frac{\operatorname{tr}(\boldsymbol{\varepsilon}) \pm \sqrt{\operatorname{tr}(\boldsymbol{\varepsilon})^2 - 4\det(\boldsymbol{\varepsilon})}}{2} = \frac{\operatorname{tr}(\boldsymbol{\varepsilon}) \pm r}{2}, \\ \varepsilon_{11} - \varepsilon_{22} &= r\cos\theta, \\ 2\varepsilon_{12} &= r\sin\theta,\end{aligned} \tag{3.58}$$

yielding the following expressions for the first and second derivatives, respectively

$$\frac{\partial \bar{\boldsymbol{\varepsilon}}}{\partial \boldsymbol{\varepsilon}} = \frac{1}{2}\begin{bmatrix} 1+\cos\theta & 1-\cos\theta & \sin\theta \\ 1-\cos\theta & 1+\cos\theta & -\sin\theta \end{bmatrix}, \tag{3.59}$$

$$\frac{\partial^2 \bar{\varepsilon}_1}{\partial \boldsymbol{\varepsilon}^2} = \frac{1}{2r}\begin{bmatrix} 1-\cos^2\theta & -1+\cos^2\theta & -\sin\theta\cos\theta \\ -1+\cos^2\theta & 1-\cos^2\theta & \sin\theta\cos\theta \\ -\sin\theta\cos\theta & \sin\theta\cos\theta & 1-\sin^2\theta \end{bmatrix} = -\frac{\partial^2 \bar{\varepsilon}_2}{\partial \boldsymbol{\varepsilon}^2}. \tag{3.60}$$

Similarly to [31], crack face penetration can also be prevented by the spectral decomposition. The main difference between the two approaches is observed when all three principal strains are negative. In this case, the deviatoric part of the strain energy density function is still degraded, producing a phase-field damage in the corresponding regions [111].

Although the anisotropic models allows crack propagation only under tensile stresses, the sub-system $\mathcal{E}_{\boldsymbol{u}} = 0$ in the Eq. (3.44) becomes nonlinear, bringing an extra computational cost. In this work, the hybrid phase-field model proposed by Ambati, Gerasimov and Lorenzis [111] is considered, where linear equilibrium equations are maintained by using an isotropic constitutive relation for the displacement sub-system (see Eq. (3.5)) and an anisotropic driving force for the phase-field. Due to its flexibility, the hybrid model allows the user to choose several different phase-field evolution laws. Here, the driving force proposed by Miehe, Hofacker and Welschinger [29, 30] is applied for `AT2` model, whereas a Rankine-based driving force is used for the `CZM` model [97], read as

$$\begin{aligned}\bar{\mathcal{H}} &= \psi_0^+(\boldsymbol{\varepsilon}) \qquad \text{for } \texttt{AT2} \\ \bar{\mathcal{H}} &= \frac{1}{2E}\langle \bar{\sigma}_1 \rangle \quad \text{for } \texttt{CZM}\end{aligned} \tag{3.61}$$

with $\bar{\sigma}_1$ being the major principal stress of $\boldsymbol{\sigma} = \partial\psi/\partial\boldsymbol{\varepsilon}$, and $\langle a \rangle = \max(0, a)$. Although hybrid model also can prevent crack face penetration by using the constraint $\phi = 0$ where $\psi_0^+ \leq \psi_0^-$ [111], since only monotonic loadings are considered in this work, no special treatment is applied to this matter.

Finally, to ensure non-negative damage field $\phi(\boldsymbol{x}) \geq 0$ an initial history value $\mathcal{H}_0$ can be computed by setting $\phi = 0$ and solving the Eq. (3.43), yielding $\mathcal{H}_0^{\texttt{AT1}} = 3\mathcal{G}_c/16\ell$, $\mathcal{H}_0^{\texttt{AT2}} = 0$, and $\mathcal{H}_0^{\texttt{CZM}} = 2\mathcal{G}_c/\pi a\ell = f_t^2/2E$ for `AT1`, `AT2`, and `CZM` models, respectively. Such initial history value is an important parameter for crack nucleation, since until the driving force exceeds this parameter, the material remains linear elastic.

It is noteworthy that neither theoretical nor numerical results prove that the global constraint Eq. (3.42) yields an equivalence between Eq. (3.44) and Eq. (3.11). Although Ambati, Gerasimov and Lorenzis [111] reinterpreted the hybrid model through a gradient-enhanced damage formulation, imposing irreversibility constraint using history variable may not lead to the correct damage profile [112]. Due to its wide employing, Eq. (3.42) is imposed in this work to facilitate the comparison with other solution methods available in the literature.

3.5 Galerkin finite element discretization

Consider $d = 2$ and a decomposition of $\bar{\Omega} = \Omega \cup \partial\Omega$ in closed quadrilateral elements $\mathcal{Q}_s$ such that $\bar{\Omega} \subset \bigcup_{s\in\mathcal{Q}_h} \mathcal{Q}_s$, with $\mathcal{Q}_h$ being the index set of the elements and h representing the size of the elements. The set of finite element nodes associated with the discretization is denoted as $\{\boldsymbol{x}_i := (x_i, y_i) \mid i \in I_h\}$, where I_h is the index set of the nodes. An approximated solution pair $(\boldsymbol{u}^h, \phi^h)$ to Eq. (3.8) can be described using the standard Galerkin method in a finite element discretization as

$$\boldsymbol{u}^h(\boldsymbol{x}) = \sum_{i\in I_h} \boldsymbol{\varphi}_i(\boldsymbol{x})\mathbf{a}_i, \qquad \phi^h(\boldsymbol{x}) = \sum_{i\in I_h} \varphi_i(\boldsymbol{x})\mathrm{b}_i, \tag{3.62}$$

where $\mathbf{a}_i \in \mathbb{R}^2$ and $\mathrm{b}_i \in \mathbb{R}$ are the unknown coefficients of displacement and phase-field, respectively, whereas $\boldsymbol{\varphi}_i(\boldsymbol{x}) = \varphi_i(\boldsymbol{x})\mathbf{I}$ with $\varphi_i(\boldsymbol{x})$ being the standard bilinear finite element shape functions associated with node $\boldsymbol{x}_i$, and $\mathbf{I}$ the identity matrix of order 2. Considering the arbitrariness of the test functions, the system of equations Eq. (3.44) can be written in terms of the approximations $\boldsymbol{u}_h$ and ϕ_h as

$$\begin{aligned}
\mathbf{r}_i^{\boldsymbol{u}} &= \int_\Omega g(\phi^h)\boldsymbol{\sigma}(\boldsymbol{u}^h) : \boldsymbol{\varepsilon}(\boldsymbol{\varphi}_i)\ \mathrm{d}\Omega - \int_{\partial\Omega_{\boldsymbol{F}}} \boldsymbol{\varphi}_i \bar{\boldsymbol{F}}_n\ \mathrm{d}s = \mathbf{0} \\
\mathrm{r}_i^{\phi} &= \int_\Omega g'(\phi^h)\varphi_i\mathcal{H}(\boldsymbol{u}^h)\ \mathrm{d}\Omega + \frac{\mathcal{G}_c}{c_w}\int_\Omega \left(\frac{w'(\phi^h)}{\ell}\varphi_i + 2\ell\nabla\phi^h\cdot\nabla\varphi_i\right)\mathrm{d}\Omega = 0,
\end{aligned} \tag{3.63}$$

where $\mathbf{r}_i^{\boldsymbol{u}}$ and r_i^{ϕ} are the residual vector for the displacement and phase-field, respectively.

In this work, the initial set of cracks is discretely represented through geometric discretization, i.e., double nodes, rather than depicting them as an initial damage diffuse zone Ω_ϕ by imposing the Dirichlet condition $\phi(\boldsymbol{x}) = 1$, e.g. [113].

4 SOLUTION ALGORITHMS

Let $\mathbf{z} := \{\boldsymbol{u}^h, \phi^h\}$ and $\mathbf{g} := \{\mathbf{r}^{\boldsymbol{u}}, \mathbf{r}^{\phi}\}$ be the solution and the residual vector of Eq. (3.63), respectively. Considering the system of nonlinear equations Eq. (3.63) subjected to an incrementally applied load such that $\mathbf{z} := \mathbf{z}_{n-1} + \Delta\mathbf{z}$ with $n \geq 1$, the residual vector can be approximated through a Taylor series expansion around the previous $\mathbf{z}_{n-1}$ as

$$\mathbf{g}(\mathbf{z}) = \mathbf{g}(\mathbf{z}_{n-1}) + \left.\frac{\partial \mathbf{g}}{\partial \mathbf{z}}\right|_{\mathbf{z}_{n-1}} \Delta\mathbf{z} + \mathcal{O}^2(\Delta\mathbf{z}) = \mathbf{0}. \tag{4.1}$$

Truncating the above equation in its first-order term, a correction increment $\Delta\mathbf{z}$ of the previously estimated solution is given by

$$\begin{aligned} \Delta\mathbf{z} &= -\left(\left.\frac{\partial \mathbf{g}}{\partial \mathbf{z}}\right|_{\mathbf{z}_{n-1}}\right)^{-1} \mathbf{g}(\mathbf{z}_{n-1}) \\ &= -\mathbf{K}_{n-1}^{-1}\mathbf{g}(\mathbf{z}_{n-1}), \end{aligned} \tag{4.2}$$

with $\mathbf{K}$, called tangent matrix, denoted by the following structure

$$\mathbf{K} = \begin{pmatrix} \mathbf{K}^{\boldsymbol{uu}} & \mathbf{K}^{\boldsymbol{u}\phi} \\ \mathbf{K}^{\phi\boldsymbol{u}} & \mathbf{K}^{\phi\phi} \end{pmatrix}, \tag{4.3}$$

whereas its components are given by

$$\begin{aligned} \mathbf{K}_{ij}^{\boldsymbol{uu}} &= \frac{\partial \mathbf{r}_i^{\boldsymbol{u}}}{\partial \mathbf{a}_j} = \int_\Omega g(\phi^h)\boldsymbol{\sigma}(\boldsymbol{\varphi}_j) : \boldsymbol{\varepsilon}(\boldsymbol{\varphi}_i)\ \mathrm{d}\Omega \\ \mathbf{K}_{ij}^{\boldsymbol{u}\phi} &= \frac{\partial \mathbf{r}_i^{\boldsymbol{u}}}{\partial \mathrm{b}_j} = \int_\Omega g'(\phi^h)\varphi_j\boldsymbol{\sigma}(\boldsymbol{u}^h) : \boldsymbol{\varepsilon}(\boldsymbol{\varphi}_i)\ \mathrm{d}\Omega \\ \mathbf{K}_{ij}^{\phi\boldsymbol{u}} &= \frac{\partial \mathrm{r}_i^{\phi}}{\partial \mathbf{a}_j} = \int_\Omega g'(\phi^h)\varphi_i\frac{\partial \mathcal{H}(\boldsymbol{u}^h)}{\partial \boldsymbol{\varepsilon}} : \boldsymbol{\varepsilon}(\boldsymbol{\varphi}_j)\ \mathrm{d}\Omega \\ \mathbf{K}_{ij}^{\phi\phi} &= \frac{\partial \mathrm{r}_i^{\phi}}{\partial \mathrm{b}_j} = \int_\Omega g''(\phi^h)\varphi_i\varphi_j\mathcal{H}(\boldsymbol{u}^h)\ \mathrm{d}\Omega + \frac{\mathcal{G}_c}{c_w}\int_\Omega \left(\frac{w''(\phi^h)}{\ell}\varphi_i\varphi_j + 2\ell\nabla\varphi_j\cdot\nabla\varphi_i\right)\mathrm{d}\Omega. \end{aligned} \tag{4.4}$$

Starting from the $\mathbf{z}_{n-1}$ found in the previous load step, the standard Newton-Raphson algorithm consists of solving the linear system of equation Eq. (4.2) iteratively until convergence is achieved at a given loading step n. In this manner, the boundary conditions for $\Delta\mathbf{z}_k$ are

$$\begin{aligned} \Delta\mathbf{z}_0 &= \mathbf{0} \text{ on } \partial\Omega_t \\ \Delta\mathbf{z}_0 &= \{\bar{\boldsymbol{u}}_n - \bar{\boldsymbol{u}}_{n-1}, 0\} \text{ on } \partial\Omega_{\boldsymbol{u}}, \end{aligned} \tag{4.5}$$

for the first iteration, and for $k \geq 1$

$$\Delta\mathbf{z}_k = \mathbf{0} \text{ on } \partial\Omega. \tag{4.6}$$

However, due to the non-convexity of the underlying energy functional, the tangent matrix in Newton-Raphson method becomes indefinite. Furthermore, due to the phase-field hybrid model and history variable $\mathcal{H}$ the tangent matrix also no longer holds symmetry, i.e, $\mathbf{K}^{u\phi} \neq \left(\mathbf{K}^{\phi u}\right)^T$. Despite the fact that Wu *et al.* [41] proposed a numerical parameter to ensure positive definiteness and symmetry to the tangent matrix, herein a weak coupling is adopted, where the inter-field coupling is neglected, leading to

$$\mathbf{K} = \begin{pmatrix} \mathbf{K}^{uu} & \mathbf{0} \\ \mathbf{0} & \mathbf{K}^{\phi\phi} \end{pmatrix}. \tag{4.7}$$

On the other hand, while the weakly coupled matrix Eq. (4.7) is symmetric – since $\mathbf{K}^{uu}$ and $\mathbf{K}^{\phi\phi}$ are always symmetric – it may still be non-positive definite. In fact, the block matrix $\mathbf{K}^{uu}$ is always positive definite, but $\mathbf{K}^{\phi\phi}$ is not necessarily so. A sufficient condition to ensure positive definiteness of $\mathbf{K}^{\phi\phi}$ is

$$\frac{\partial \mathbf{r}^{\phi}}{\partial \mathbf{b}} \geq 0. \tag{4.8}$$

This condition is automatically satisfied for the `AT1` and `AT2` models. However, for the `CZM` model, depending on the softening law, it must be ensured that $\ell \leq (0.64 \sim 0.33)\ell_{\text{ch}}$ to satisfy the above requirement [32]. Following Wu, Huang and Nguyen [32], in this work, the length scale parameter for the `CZM` model is always set to $\ell \leq \ell_{\text{ch}}/3$.

However, simply employing Eq. (4.7) may not be suitable for problems in which the mechanical behavior is strongly coupled with the phase-field [26]. To overcome this issue, the next sections introduce alternative methods to solve the nonlinear system of equations.

In numerous implementations and theoretical papers [6, 7, 31, 86, 87], a model parameter $0 < \eta \ll 1$ is introduced in the degradation function, such that $\tilde{g}(\phi) = g(\phi) + \eta$ to ensure a residual stiffness, avoiding ill-posedness of the tangent matrix. However, all numerical experiments in this work were performed with $\eta = 0$. In the dynamic analysis context, Borden *et al.* [9] also mentioned the unnecessary use of η to guarantee well-conditioning.

4.1 Alternating minimization solver (AM)

Although solving the discrete governing equations Eq. (3.44) simultaneously is challenging due to its strong coupling and lack of convexity, it can be alleviated by solving one field at a time. In fact, Bourdin, Francfort and Marigo [6] show that each field in the functional Eq. (3.3) is convex if the other field is fixed. Based on this statement, the alternating minimization solver (AM), also known as staggered solver, is a two-step iterative method where each field is solved sequentially until convergence is achieved for both $\boldsymbol{u}^h$ and ϕ^h. The algorithm is detailed in Alg. 1.

Algorithm 1: Alternating minimization solver

Given $(\boldsymbol{u}^h_{n-1},\, \phi^h_{n-1})$, $\mathcal{H}_{n-1}$ and $\bar{\boldsymbol{u}}_n$.
Initialize $k = 0$, $\boldsymbol{u}_0 = \boldsymbol{u}^h_{n-1}$, $\phi_0 = \phi^h_{n-1}$.
while *not converged (see Eq. (4.30))* **do**
    Compute $\Delta\boldsymbol{u}_k = -[\mathbf{K}^{\boldsymbol{uu}}(\boldsymbol{u}_k,\, \phi_k)]^{-1}\mathbf{r}^{\boldsymbol{u}}(\boldsymbol{u}_k,\, \phi_k)$
    Set $\boldsymbol{u}_{k+1} = \boldsymbol{u}_k + \Delta\boldsymbol{u}_k$
    Compute $\mathcal{H}_{k+1} = \max\{\mathcal{H}_{n-1},\, \bar{\mathcal{H}}(\boldsymbol{u}_{k+1})\}$
    Compute $\Delta\phi_k = -[\mathbf{K}^{\phi\phi}(\boldsymbol{u}_{k+1},\, \phi_k)]^{-1}\mathbf{r}^{\phi}(\boldsymbol{u}_{k+1},\, \phi_k)$
    Set $\phi_{k+1} = \phi_k + \Delta\phi_k$
    $k = k + 1$
end
Set $(\boldsymbol{u}^h,\, \phi^h) = (\boldsymbol{u}_k,\, \phi_k)$, and $\mathcal{H} = \mathcal{H}_k$

4.2 Over-relaxed alternate minimization solver (ORAM)

The alternating minimization solver offers robustness and stability, but it also requires high computational costs to achieve convergence for both fields. According to Farrell and Maurini [35], the alternated minimization solver can be accelerated by over-relaxation. The method consists of scaling the search direction of each field by a factor $\omega \in [1,\, 2]$ and then updating the solution as described below.

Algorithm 2: Over-relaxed alternate minimization solver

Given $(\boldsymbol{u}^h_{n-1},\, \phi^h_{n-1})$, $\mathcal{H}_{n-1}$ and $\bar{\boldsymbol{u}}_n$.
Initialize $\boldsymbol{u}_0 = \boldsymbol{u}^h_{n-1}$, $\phi_0 = \phi^h_{n-1}$, $k = 0$.
while *not converged* **do**
    Compute $\Delta\boldsymbol{u}_k = -\mathbf{K}^{\boldsymbol{uu}}(\boldsymbol{u}_k,\, \phi_k)\mathbf{r}^{\boldsymbol{u}}(\boldsymbol{u}_k,\, \phi_k)$
    Set $\boldsymbol{u}_{k+1} = \boldsymbol{u}_k + \omega\Delta\boldsymbol{u}_k$
    Compute $\mathcal{H}_{k+1} = \max\{\mathcal{H}_{n-1},\, \bar{\mathcal{H}}(\boldsymbol{u}_{k+1})\}$
    Compute $\Delta\phi_k = -\mathbf{K}^{\phi\phi}(\boldsymbol{u}_{k+1},\, \phi_k)\mathbf{r}^{\phi}(\boldsymbol{u}_{k+1},\, \phi_k)$
    Set $\phi_{k+1} = \phi_k + \omega\Delta\phi_k$
    $k = k + 1$
end
Set $(\boldsymbol{u}^h_n,\, \phi^h_n) = (\boldsymbol{u}_k,\, \phi_k)$, and $\mathcal{H}_n = \mathcal{H}_k$

Defining an optimal ω factor requires a spectral analysis of the tangent matrix [114], which brings additional complexity and computational costs to the solver. Instead, Storvik *et al.* [36] prove through several numerical analyses that high values of ω can improve the convergence rate of the alternating minimization solver in phase-field analysis. For this work, several numerical experiments were performed and $\omega = 1.8$ (see Fig. 4) provides the best trade-off between convergence rate and computational costs for steps where the crack propagates, which is consistent with the results of Storvik *et al.* [36]. It is worth noting that phase-field models that are not self-contained require additional treatment to avoid

the update $\phi_{k+1} = \phi_k + \omega\delta\phi_{k+1}$ violates the boundness $\phi \in [0,1]$ [35]. Since the analysis are limited to `AT2` and `CZM` models, nothing is done concerning this issue.

Figure 4 – **Bar under tension** (see section 5.1 for further details)**:** Number of iterations per load increment to reach convergence for the over-relaxed alternate minimization solver with different values of ω. The standard alternating minimization solver is represented by $\omega = 1.0$. These results refer to the `AT2` model, see section 5.1 for further details. Similarly, the same conclusion is reached for `CZM` model.

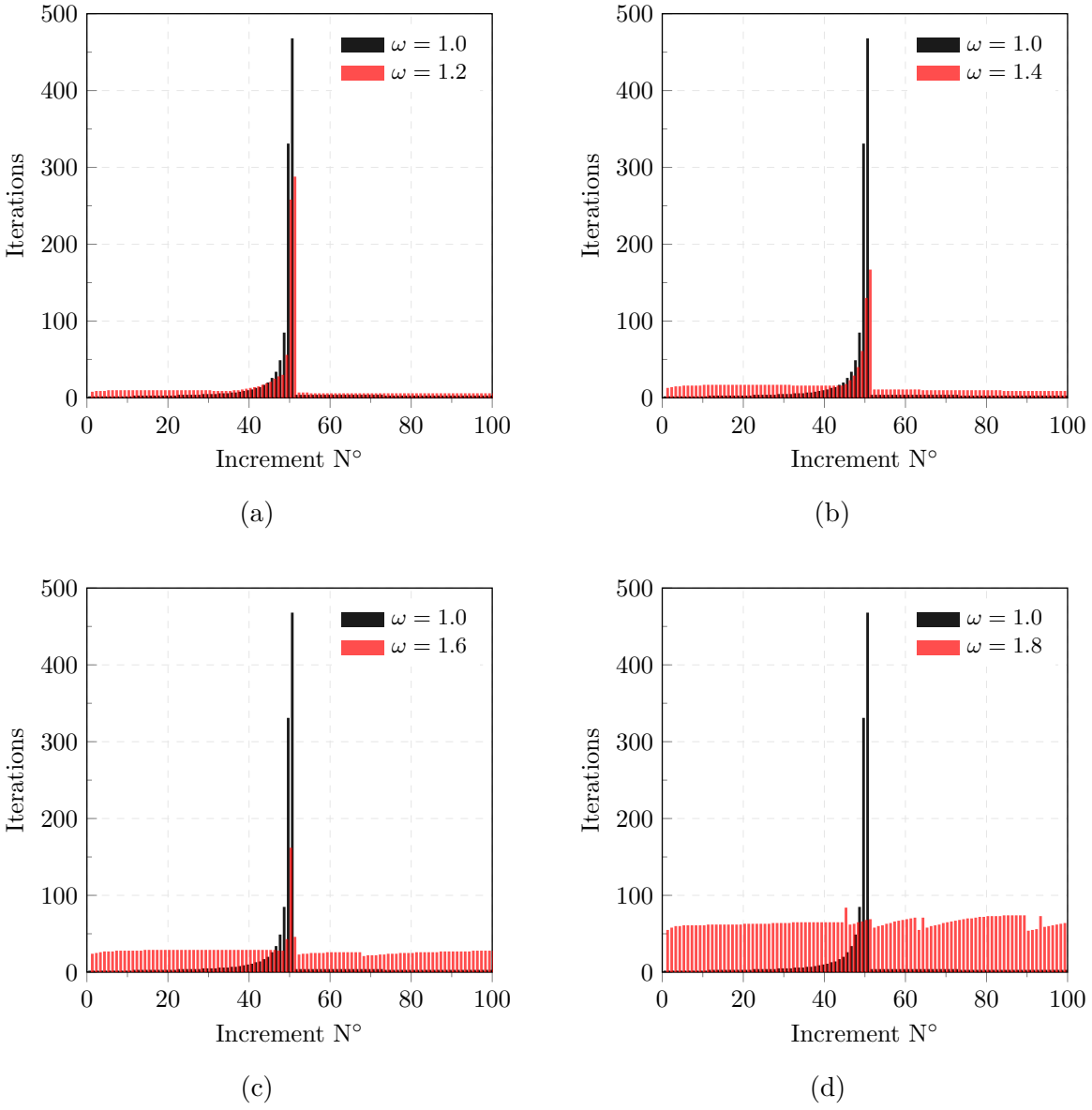

Source: The author.

In an overall view, the over-relaxed alternate minimization solver usually slows down the convergence rate, increasing the number of iterations in quasi-static load steps and accelerating when the crack propagation occurs [36], see Fig. 4. On the other hand, in subsection 4.3.2 a composite algorithm is proposed in which the over-relaxed alternate minimization can be enabled only when brutal crack propagation occurs.

4.3 Limited-memory Broyden-Fletcher-Goldfarb-Shanno solver (L-BFGS)

Quasi-Newton methods have been widely used in a variety of optimization problems due to their computational economy and efficiency. While for each iteration Newton's method requires a computational effort of $\mathcal{O}(\text{dim}^2)$ to build and factorize the tangent matrix, quasi-Newton methods approximate the curvature information based on differencing two consecutive gradients, which demands $\mathcal{O}(\text{dim})$, where dim represents the size of $\mathbf{z}$. Therefore, by taking advantage of the second-order behavior, quasi-Newton methods provide a lower computational effort per iteration than Newton's method. In general, the convergence rate of quasi-Newton methods is slower than Newton's method, but the computational savings can make quasi-Newton methods more efficient in situations where the tangent matrix is either unavailable or challenging to compute.

For a given load step n, let the updated solution $\mathbf{z}_{k+1} := \mathbf{z}_k + \lambda_k \Delta \mathbf{z}_k$ at the k^{th} iteration, where λ_k is the step size along the descent direction $\Delta \mathbf{z}_k$. To avoid computing the tangent matrix at each iteration k, quasi-Newton methods rearrange the Taylor expansion Eq. (4.1) such that updates provided by recent gradient evaluations build an approximated global matrix $\tilde{\mathbf{K}}_k$, read as following

$$\mathbf{g}_{k+1} = \mathbf{g}_k + \lambda_k \tilde{\mathbf{K}}_{k+1} \Delta \mathbf{z}_k. \tag{4.9}$$

Considering $\mathbf{s}_k := \mathbf{z}_{k+1} - \mathbf{z}_k = \lambda_k \Delta \mathbf{z}_k$ and $\mathbf{y}_k := \mathbf{g}_{k+1} - \mathbf{g}_k$, the new approximate $\tilde{\mathbf{K}}_{k+1}$ can be interpreted as a mapping of the solution increment $\mathbf{s}_k$ into the gradient difference $\mathbf{y}_k$, in other words

$$\tilde{\mathbf{K}}_{k+1} \mathbf{s}_k = \mathbf{y}_k. \tag{4.10}$$

This expression is called *secant condition* and can also be written in terms of the approximate inverse of the tangent matrix, rendering

$$\tilde{\mathbf{K}}_{k+1}^{-1} \mathbf{y}_k = \mathbf{s}_k. \tag{4.11}$$

A variety of quasi-Newton methods are available, where extra constraints are added to the *secant condition*, leading to different ways of updating the tangent matrix at each iteration. Among them, the Broyden-Fletcher-Goldfarb-Shanno (BFGS) method [115–118] is the most popular one. Such an approach gives the most conservative change relative to $\tilde{\mathbf{K}}_k^{-1}$ by solving the following optimization problem

$$\begin{aligned} &\min_{\tilde{\mathbf{K}}_{k+1}^{-1}} \left\{ ||\tilde{\mathbf{K}}_{k+1}^{-1} - \tilde{\mathbf{K}}_k^{-1}||^2 \right\} \\ &\text{subject to } \tilde{\mathbf{K}}_{k+1}^{-1} = (\tilde{\mathbf{K}}_{k+1}^{-1})^T \\ &\text{and } \tilde{\mathbf{K}}_{k+1}^{-1} \mathbf{y}_k = \mathbf{s}_k. \end{aligned} \tag{4.12}$$

where $||\cdot||$ denotes the weighted Frobenius norm, where $||\boldsymbol{A}|| = \sqrt{\sum_i^m \sum_j^n |a_{ij}|^2}$. The minimizer of the above problem leads to the BFGS update formula

$$\tilde{\mathbf{K}}_{k+1}^{-1} = \left(\mathbf{I} - \rho_k \mathbf{s}_k \mathbf{y}_k^T\right) \tilde{\mathbf{K}}_k^{-1} \left(\mathbf{I} - \rho_k \mathbf{y}_k \mathbf{s}_k^T\right) + \rho_k \mathbf{s}_k \mathbf{s}_k^T, \tag{4.13}$$

where $\rho_k = 1/\mathbf{s}_k^T\mathbf{y}_k$ is called curvature parameter. Due to the constraints on the optimization problem Eq. (4.12), the initial guess $\tilde{\mathbf{K}}_0$ must be symmetric and positive definite. In many cases, an identity matrix is used as an initial guess, but the better the initial guess matrix, the better the convergence rate [119]. In this manner, the optimum scenario is to employ the full tangent matrix Eq. (4.3), however, it can give a non-symmetric and non-positive definite matrix. Therefore, the initial guess matrix $\tilde{\mathbf{K}}_0$ is computed by using the weakly coupled matrix Eq. (4.7).

Although the finite element discretization leads to a sparse $\tilde{\mathbf{K}}_0$, after several consecutive k updates given by Eq. (4.13), the $\tilde{\mathbf{K}}_{k+1}$ gradually becomes dense[1]. From a computational perspective, storing such a matrix leads to a quadratic memory demand, which is challenging for large-scale problems.

In contrast, the limited memory version of BFGS (L-BFGS) [120, 121] stores a history of the m updates of the $\mathbf{s}_k$ and $\mathbf{y}_k$ vectors, rendering an implicit representation of the approximated tangent matrix without explicitly storing $\tilde{\mathbf{K}}_{k+1}$. Resulting in a linear memory requirement, the L-BFGS method preserves the matrix sparsity, being more suitable for large problems.

The fundamental strength of L-BFGS stems from its ability to construct the inverse tangent matrix implicitly through a hierarchical expansion framework. This methodology enables the representation of $\tilde{\mathbf{K}}_{k+1}^{-1}$ after $k+1$ iterations in the following manner:

$$\begin{aligned}\tilde{\mathbf{K}}_{k+1}^{-1} = (\boldsymbol{V}_k \cdots \boldsymbol{V}_0)\tilde{\mathbf{K}}_0^{-1}(\boldsymbol{V}_k \cdots \boldsymbol{V}_0)^T + (\boldsymbol{V}_k \cdots \boldsymbol{V}_1)\rho_0\mathbf{s}_0\mathbf{s}_0^T(\boldsymbol{V}_k \cdots \boldsymbol{V}_1)^T \\ + (\boldsymbol{V}_k \cdots \boldsymbol{V}_2)\rho_1\mathbf{s}_1\mathbf{s}_1^T(\boldsymbol{V}_k \cdots \boldsymbol{V}_2)^T + \cdots + \rho_k\mathbf{s}_k\mathbf{s}_k^T\end{aligned} \tag{4.14}$$

where $\boldsymbol{V}_k = (\mathbf{I} - \rho_k\mathbf{s}_k\mathbf{y}_k^T)$ represents the transformation operator for the kth update. The search direction for the $(k+1)$th iteration is then computed as $\Delta\mathbf{z}_{k+1} = -\tilde{\mathbf{K}}_{k+1}^{-1}\mathbf{g}_{k+1}$, where the inverse matrix $\tilde{\mathbf{K}}_{k+1}^{-1}$ is never explicitly assembled but rather evaluated using the hierarchical formulation presented in Eq. (4.14).

The computational implementation employs a two-stage iterative procedure that efficiently handles the matrix-vector product between $\tilde{\mathbf{K}}_{k+1}^{-1}$ and the residual $\mathbf{g}_{k+1}$. This algorithm exhibits linear scaling with respect to both the problem dimension and the memory parameter, specifically $\mathcal{O}(\text{dim} \times m)$, where m denotes the number of vector pairs retained in memory.

In practice, the $\tilde{\mathbf{K}}_0^{-1}$ is updated until the m^{th} iteration is reached without convergence. Then, the matrix is rebuilt for the current solution $\mathbf{z}_k$, restarting the update process. Since storing several vectors is not memory attractive, generally $m = (2 \sim 8)$. For a detailed description of the L-BFGS algorithm, the reader is referred to [120].

[1] Looking in Eq. (4.13), we observe that the tangent matrix is both pre- and post-multiplied by matrices. These matrices are dense because the operation $\rho_k\mathbf{y}_k\mathbf{s}_k^T$ produces a dense matrix.

To ensure that the update $\tilde{\mathbf{K}}_{k+1}^{-1}$ inherits the initial guess matrix properties, the *curvature condition* must be satisfied, which is given by

$$\frac{1}{\rho_k} > 0 \quad \text{or} \quad \mathbf{s}_k^T \mathbf{y}_k > 0. \tag{4.15}$$

In general, this condition is fulfilled by a step size λ_k given by an exact line search or a Wolfe-type inexact line search. Such cases are achieved by convex minimization problems, rendering global and superlinear convergence to the BFGS method [122–124]. Many modified BFGS methods have been proposed to deal with non-convex objective functions [125–127], among them was selected the simplest one [127], in which the update formula Eq. (4.13) becomes

$$\tilde{\mathbf{K}}_{k+1}^{-1} = \begin{cases} \left(\mathbf{I} - \rho_k \mathbf{s}_k \mathbf{y}_k^T\right) \tilde{\mathbf{K}}_k^{-1} \left(\mathbf{I} - \rho_k \mathbf{y}_k \mathbf{s}_k^T\right) + \rho_k \mathbf{s}_k \mathbf{s}_k^T, & \text{if } \mathbf{s}_k^T \mathbf{y}_k > 0 \\ \tilde{\mathbf{K}}_k^{-1}, & \text{otherwise.} \end{cases} \tag{4.16}$$

However, convergence is not guaranteed by just using either the standard Eq. (4.13) or the modified Eq. (4.16) BFGS method. In fact, in tests performed in this work, both BFGS approaches diverge in load steps with unstable crack propagation. To avoid the divergence, a line search is required to control the search direction $\Delta \mathbf{z}_k$ [120]. This issue is overcome by a new gradient-based line search method, which is discussed in subsection 4.3.1. Aided by this line search, Fig. 5 shows the effect of using the modified BFGS method in relation to its standard version. As is observed in Fig. 5, the only difference between both BFGS approaches occurs at the step where the crack propagates (step 50), which is when the non-convexity of the phase-field model becomes evident. In such situations, the modified BFGS method provides a better convergence rate.

The full L-BFGS algorithm employed in this work is presented in Alg. 3. For simplicity, for the rest of this work, the modified L-BFGS method is referred to L-BFGS.

The complete algorithm is openly available to the community in the `BORAM` repository [128]. This repository provides mostly self-contained examples of phase-field fracture problems that demonstrate the proposed solver. The implementation is written in `C++` and is designed for integration with other FEM codes. The only external dependency is the open-source `Eigen` library [129], which is used for matrix algebra operations. Configuration and compilation instructions are provided in the repository.

Algorithm 3: Modified Limited-memory Broyden-Fletcher-Goldfarb-Shanno (L-BFGS) algorithm

Given $(\boldsymbol{u}^h_{n-1},\, \phi^h_{n-1})$, $\mathcal{H}_{n-1}$, $\bar{\boldsymbol{u}}_n$ and m.
Initialize $\mathbf{z}_0 = (\boldsymbol{u}^h_{n-1},\, \phi^h_{n-1})$.
compute $\mathbf{g}_0 = \mathbf{g}(\mathbf{z}_0)$
compute $\tilde{\mathbf{K}}_0^{-1} = \tilde{\mathbf{K}}^{-1}(\mathbf{z}_0)$
$p = 0$, $h = 0$
for $k = 0,\, 1,\, 2,\, \ldots$ **do**
    $\mathbf{q}_p = \mathbf{g}_k$
    for $i = 0,\, 1,\, \ldots,\, p$ **do**
        $j = p - i - 1$
        compute and store $\alpha_j = \rho_{j+1}\mathbf{s}_{j+1}^T\mathbf{q}_{j+1}$
        compute $\mathbf{q}_j = \mathbf{q}_{j+1} - \mathbf{y}_{j+1}\alpha_j$
    end
    Solve $\mathbf{d}_0 = \tilde{\mathbf{K}}_0^{-1}\mathbf{q}_0$ through Cholesky factorization
    for $i = 0,\, 1,\, \ldots,\, p$ **do**
        $j = i + 1$
        compute $\beta_j = \rho_j\mathbf{y}_j^T\mathbf{d}_{j-1}$
        compute $\mathbf{d}_j = \mathbf{d}_{j-1} + \mathbf{s}_j\,(\alpha_{j-1} - \beta_j)$
    end
    $\Delta\mathbf{z}_k = -\mathbf{d}_p$
    compute λ_k (Alg. 4)
    update $\mathbf{z}_{k+1} = \mathbf{z}_k + \lambda_k\Delta\mathbf{z}_k$
    compute $\mathbf{g}_{k+1} = \mathbf{g}(\mathbf{z}_{k+1})$
    if *converged (see Eq. (4.30))* **then**
        break
    end
    if $p + h > m$ **then**
        compute $\tilde{\mathbf{K}}_0^{-1} = \tilde{\mathbf{K}}^{-1}(\mathbf{z}_{k+1})$
        $p = 0$, $h = 0$
    else
        compute $\mathbf{s}_{p+1}, \mathbf{y}_{p+1}, \rho_{p+1}$
        if $\mathbf{s}_{p+1}^T\mathbf{y}_{p+1} > 0$ **then**
            store $\mathbf{s}_{p+1}, \mathbf{y}_{p+1}, \rho_{p+1}$
            $p = p + 1$
        else
            $h = h + 1$
        end
    end
end
Set $(\boldsymbol{u}^h,\, \phi^h) = \mathbf{z}_{k+1}$, and $\mathcal{H} = \mathcal{H}_{k+1}$

Figure 5 – **Bar under tension** (see section 5.1 for further details)**:** Number of iterations per load increment to reach convergence. Comparison between standard L-BFGS Eq. (4.13) and the modified L-BFGS Eq. (4.16). These results refer to the `AT2` model, see section 5.1 for further details.

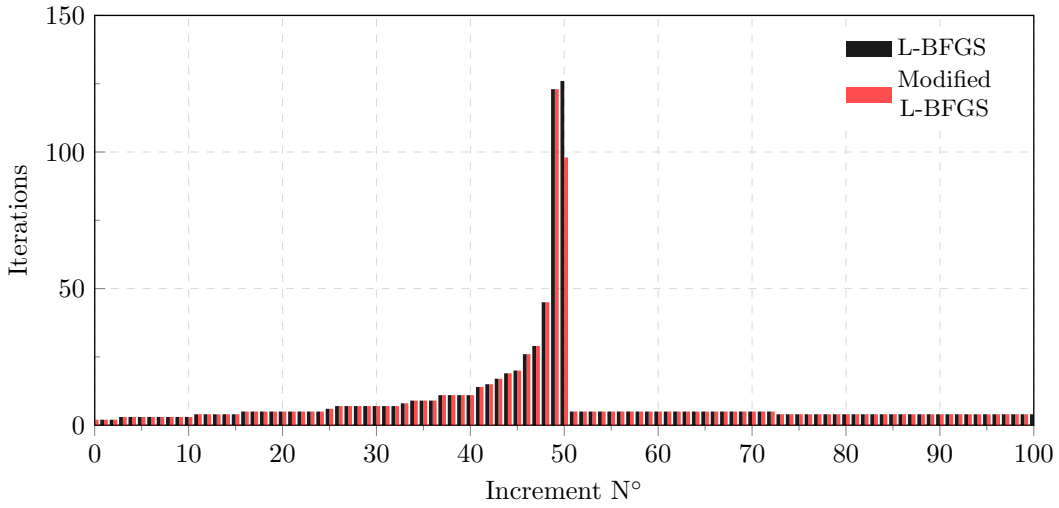

Source: The author.

4.3.1 Quasi-Newton line search

The use of line search methods to prevent divergence of phase-field analysis under the Newton-Raphson algorithm has been studied in a few works [24, 26, 27]. For instance, Gerasimov and Lorenzis [24] established that the Newton-Raphson algorithm diverges when an increase in energy is observed between two consecutive iterations, i.e., $\tilde{\mathcal{E}}(\mathbf{z}_k + \Delta\mathbf{z}_k) > \tilde{\mathcal{E}}(\mathbf{z}_k)$. To overcome this issue, they proposed a line search based on gradient monitoring, such that, at a fixed load step n and Newton-Raphson iteration k, the following condition must be fulfilled for the energy functional Eq. (3.3)

$$\tilde{\mathcal{E}}(\mathbf{z}_k + \lambda\Delta\mathbf{z}_k) < \tilde{\mathcal{E}}(\mathbf{z}_k), \tag{4.17}$$

where λ is the step size that provides the lowest energy. In a variational consistent formulation, the tendency of the energy functional is indicated by the signal of its gradient. Therefore, consider the first variation of Eq. (3.3) with respect to the line search parameter λ given by

$$\tilde{\mathcal{E}}_\lambda(\mathbf{z}_k + \lambda\Delta\mathbf{z}_k; \delta\lambda) = \mathbf{g}(\mathbf{z}_k + \lambda\Delta\mathbf{z}_k)^T\Delta\mathbf{z}_k. \tag{4.18}$$

Evaluating Eq. (4.18) at $\lambda = 0$ yields two different situations: (i) a positive curvature for $\tilde{\mathcal{E}}_\lambda < 0$, in which the energy is decreasing and $\lambda \in (0,\, 1]$, and (ii) a negative curvature for $\tilde{\mathcal{E}}_\lambda > 0$, which may not lead to energy decreasing for $\lambda \in (0,\, 1]$. In the latter case, Gerasimov and Lorenzis [24] proposed to also search for $\lambda \in [-1,\, 0)$, in contrast with a standard line search in which λ is restricted to $(0,\, 1]$. Accordingly, to find the optimal step size λ_k to be applied in the k^{th} Newton-Raphson iteration, they proposed to discretize the interval

$[-1, 1]$ in 20 uniform segments $[\lambda_l, \lambda_{l+1}]$, where $\lambda_l := -1 + l/10$ and $l = 0, 1, \ldots, 20$. For each segment, a cubic polynomial interpolation is constructed using the values of $\tilde{\mathcal{E}}$ and $\tilde{\mathcal{E}}_\lambda$ computed at the endpoints of the segment, leading to a global approximation of the energy functional in the interval $[-1, 1]$. The optimal step size λ_k is then directly determined by the minimum of this global approximation. If no negative curvature is detected at $\lambda = 0$, the above procedure is restricted to the interval $(0, 1]$ with 10 segments. Wick [26] successfully applied a similar approach, where the interval $[-1, 1]$ is discretized in 40 segments and no interpolation is applied to segments, the optimal λ_k is defined as the larger λ_l value that satisfies condition Eq. (4.17).

Although Gerasimov and Lorenzis [24] approach is able to prevent divergence of the Newton-Raphson algorithm, the evaluation of $\tilde{\mathcal{E}}$ and $\tilde{\mathcal{E}}_\lambda$ at each l can be expensive, especially for large-scale problems. Moreover, the energy monitoring approach is applicable only for variationally consistent formulations, since a global energy functional exists, which is not true for the phase-field models studied in this work, where history variables (see Eq. (3.43)) are applied, or in problems with only a free energy functional with dissipation as described in [17]. Indeed, as shown Figs. 8a, 8b, 8c, 8d and 8e the non-variational nature of the employed phase-field models becomes evident, since Eq. (3.3) becomes a *pseudo* energy functional, leading to behaviour that is not in agreement with its derivative. Lampron, Therriault and Lévesque [27] also applied a line search for a modified Newton method to avoid divergence, where an Armijo backtracking algorithm based on energy monitoring is employed, which falls into the same drawback. Recently, Jin, Li and Chen [20] implemented a linear search based on Wolfe conditions, but they did not provide details on how the non-variational nature of the phase-field model was handled to perform the energy functional interpolation required to find the optimal step size.

In many applications, the step size λ_k in the BFGS context is determined by Wolfe-type inexact line search conditions

$$\begin{cases} \tilde{\mathcal{E}}(\mathbf{z}_k + \lambda_k \Delta \mathbf{z}_k) \leq \tilde{\mathcal{E}}(\mathbf{z}_k) + \sigma_1 \lambda_k \mathbf{g}(\mathbf{z}_k)^T \Delta \mathbf{z}_k, \\ \mathbf{g}(\mathbf{z}_k + \lambda_k \Delta \mathbf{z}_k)^T \Delta \mathbf{z}_k \geq \sigma_2 \mathbf{g}(\mathbf{z}_k)^T \Delta \mathbf{z}_k, \end{cases} \tag{4.19}$$

in which σ_1, σ_2 are positive constants such that $\sigma_1 < \sigma_2 < 1$. If λ_k satisfies both conditions, then the step size is accepted and global convergence is guaranteed in convex problems. However, due to the non-variational consistency of the phase-field model employed in this work, the first condition of Eq. (4.19) can not be evaluated. In fact, the majority of the works currently available in the literature employing BFGS for phase-field analysis [32, 39, 130–132] use the implementation of ABAQUS [42], where the line search is not based on energy monitoring and convergence is evaluated either in the step size change, in the number of iterations, or in the residual vector. Our proposed line search consists of using a quasi-Newton method to find the optimal λ_k, in which, at a given load step n and

iteration k, it is determined by

$$\arg\min\{\tilde{\mathcal{E}}(\mathbf{z}_k + \lambda\Delta\mathbf{z}_k) \mid \mathbf{z}_k \in \boldsymbol{\mathcal{V}}_n \times \mathcal{D}_n,\ \Delta\mathbf{z}_k \in \boldsymbol{\mathcal{V}}_n \times \mathcal{D}_n,\ \lambda \in \mathbb{R}\}. \tag{4.20}$$

The minimizer of the above expression is such that $\tilde{\mathcal{E}}_\lambda = 0$, see Eq. (4.18). Invoking an iterative procedure, an approximation of $\tilde{\mathcal{E}}_\lambda$ can be expressed by a Taylor series expansion, denoted as

$$\begin{aligned}\mathbf{g}(\mathbf{z}_k + \lambda_{l+1}\Delta\mathbf{z}_k)^T\Delta\mathbf{z}_k &= \mathbf{g}(\mathbf{z}_k + \lambda_l\Delta\mathbf{z}_k)^T\Delta\mathbf{z}_k + \frac{\mathrm{d}}{\mathrm{d}\lambda}\left(\mathbf{g}(\mathbf{z}_k + \lambda_l\Delta\mathbf{z}_k)^T\Delta\mathbf{z}_k\right)\Delta\lambda_l + \mathcal{O}^2(\Delta\lambda_l) = 0 \\ &= \mathbf{g}(\mathbf{z}_k + \lambda_l\Delta\mathbf{z}_k)^T\Delta\mathbf{z}_k + (\Delta\mathbf{z}_k)^T\,\mathbf{K}(\mathbf{z}_k + \lambda_l\Delta\mathbf{z}_k)\Delta\mathbf{z}_k\Delta\lambda_l + \mathcal{O}^2(\Delta\lambda_l) = 0.\end{aligned} \tag{4.21}$$

Truncating in its first-order terms, the above equation can be rearranged as

$$\Delta\lambda_l = -\frac{\mathbf{g}(\mathbf{z}_k + \lambda_l\Delta\mathbf{z}_k)^T\Delta\mathbf{z}_k}{(\Delta\mathbf{z}_k)^T\,\mathbf{K}(\mathbf{z}_k + \lambda_l\Delta\mathbf{z}_k)\Delta\mathbf{z}_k}. \tag{4.22}$$

From a computational perspective, it is not convenient to compute the tangent matrix at each iteration. Instead, the second derivative of the energy with respect to λ is approximated using the secant method, in which

$$\frac{\mathrm{d}}{\mathrm{d}\lambda}\left(\mathbf{g}(\mathbf{z}_k + \lambda_l\Delta\mathbf{z}_k)^T\Delta\mathbf{z}_k\right) = \frac{\left(\mathbf{g}(\mathbf{z}_k + \lambda_l\Delta\mathbf{z}_k) - \mathbf{g}(\mathbf{z}_k + \lambda_{l-1}\Delta\mathbf{z}_k)\right)^T\Delta\mathbf{z}_k}{\lambda_l - \lambda_{l-1}}. \tag{4.23}$$

Let $\Delta\lambda_{l-1} = \lambda_l - \lambda_{l-1}$, and $\mathbf{y}_{l-1} = \mathbf{g}(\mathbf{z}_k + \lambda_l\Delta\mathbf{z}_k) - \mathbf{g}(\mathbf{z}_k + \lambda_{l-1}\Delta\mathbf{z}_k)$, then the above equation can be rewritten as

$$\frac{\mathrm{d}}{\mathrm{d}\lambda}\left(\mathbf{g}(\mathbf{z}_k + \lambda_l\Delta\mathbf{z}_k)^T\Delta\mathbf{z}_k\right) = \frac{\left(\mathbf{y}_{l-1}\right)^T\Delta\mathbf{z}_k}{\Delta\lambda_{l-1}}. \tag{4.24}$$

Finally, the updated step length is given by

$$\begin{aligned}\lambda_{l+1} &= \lambda_l + \Delta\lambda_l \\ &= \lambda_l - \Delta\lambda_{l-1}\frac{(\mathbf{g}_l)^T\Delta\mathbf{z}_k}{\left(\mathbf{y}_{l-1}\right)^T\Delta\mathbf{z}_k}.\end{aligned} \tag{4.25}$$

Summarizing, the line search procedure proposed here consists of, having at hand the solution $\mathbf{z}_k$ and the correction $\Delta\mathbf{z}_k$ at the k^{th} L-BFGS iteration, finding the lowest $|\tilde{\mathcal{E}}_\lambda(\mathbf{z}_k + \lambda_l\Delta\mathbf{z}_k)|$ along the descent direction $\Delta\mathbf{z}_k$, such that, in cases where a global energy functional exists, it will coincide with the minimum of $\tilde{\mathcal{E}}(\mathbf{z}_k + \lambda_l\Delta\mathbf{z}_k)$. Thus, the optimal $\lambda_k = \lambda_l$, is taken as guess for $(k+1)^{th}$ L-BFGS iteration. In this way, energy evaluation is not required to perform the line search, and less $\tilde{\mathcal{E}}_\lambda$ evaluations are required, compared to the Gerasimov and Lorenzis [24] approach. It is worth mentioning that our linear search is not limited to an interval, such that λ_k can be greater than one, which can accelerate the solution convergence.

Finally, to apply the line search only in critical iterations, a criterion of activation is required. Gerasimov and Lorenzis [24] proposed to activate the line search when $\tilde{\mathcal{E}}_{k+1} > \tilde{\mathcal{E}}_k$ is detected. However, since the global energy functional is not available in the phase-field models present in this work, we activate the line search based on the curvature condition. The curvature parameter ρ_k plays an important role in the convergence of the L-BFGS algorithm, such that, during equilibrium iterations, larger values of $\mathbf{s}_k^T\mathbf{y}_k$ lead to divergence. Examining Eq. (4.25) it is evident that at the first iteration $l = 1$, the denominator $\left(\mathbf{y}_{l-1}\right)^T \Delta\mathbf{z}_k = \mathbf{s}_k^T\mathbf{y}_k$. However, this same parameter is used to compute the step length, creating a potential issue when divergence is detected. To address this concern, the following criterion is proposed

$$\begin{cases} \mathbf{z}_{k+1} = \mathbf{z}_k + \lambda_k \Delta\mathbf{z}_k, & \mathbf{s}_k^T\mathbf{y}_k > \texttt{TOL}_{\texttt{LS}}^{\texttt{act}} \\ \mathbf{z}_{k+1} = \mathbf{z}_k + \Delta\mathbf{z}_k, & \text{otherwise,} \end{cases} \tag{4.26}$$

and convergence of the step size is reached when $\Delta\lambda_l \leq \texttt{TOL}_{\texttt{LS}}$. In this work, $\texttt{TOL}_{\texttt{LS}}^{\texttt{act}} = 10^{-5}$ and $\texttt{TOL}_{\texttt{LS}} = 10^{-4}$. The proposed line search procedure is summarized in Alg. 4.

Algorithm 4: Quasi-newton line search

```
Given z_k, Δz_k and g_k.
Set λ_k = 1
Compute g_{k+1} = g(z_k + λ_k Δz_k)
Compute s_k and y_k
if s_k^T y_k > TOL_LS^act then
    Set l = 1
    Set Δλ_{l-1} = 1
    Set g_l = g_{k+1}
    Set y_{l-1} = y_k
    for l = 1, 2, 3, ... do
        Compute Δλ_l = -Δλ_{l-1} (g_l)^T Δz_k / (y_{l-1})^T Δz_k
        Set λ_{l+1} = λ_l + Δλ_l
        if Δλ_l ≤ TOL_LS then
            Set λ_k = λ_{l+1}
            break
        else if l == l_max then
            Set λ_k = 1.0
            break
        Compute g_{l+1} = g(z_k + λ_{l+1} Δz_k)
        Compute y_l
    end
end
```

Figs. 6, 7 and 8 illustrate the line search performance in certain special situations. The maximum number of iterations of the line search algorithm is $l_{max} = 10$. The following observations can be highlighted:

Figure 6 – **Bar under tension** (see section 5.1 for further details): Convergence of the L-BFGS algorithm for steps close to nucleation and brutal crack propagation (step 51). $||\mathbf{g}_k||_2$ refers to the L2-norm of the residual vector. These results refer to the `AT2` model.

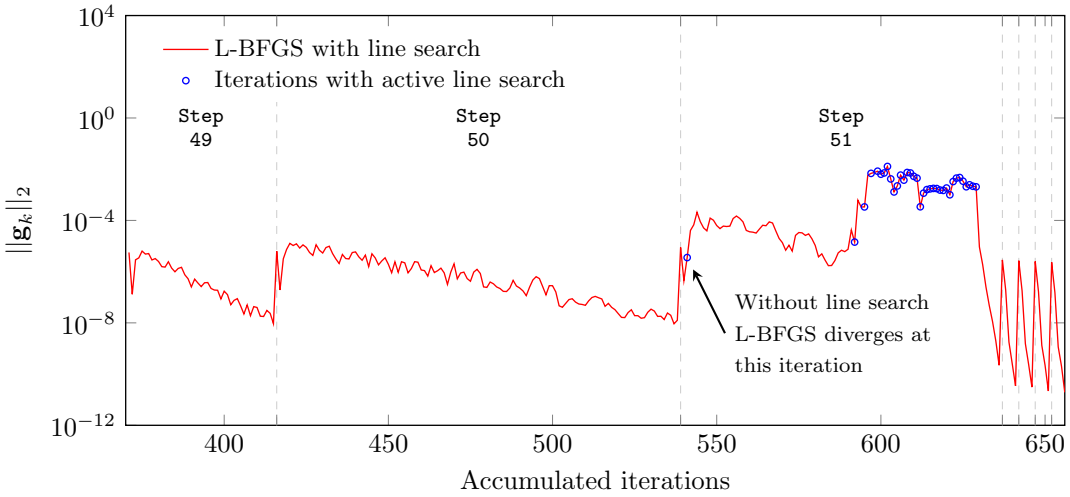

Source: The author.

- Although the L-BFGS algorithm presents oscillatory behavior during the convergence process, as shown in Fig. 6, the line search activation criterion is only triggered in iterations where either a high or an almost constant evolution of the residual is observed.

- Fig. 7a shows that the proposed line search is able to capture negative values, which is in agreement with Gerasimov and Lorenzis [24].

- In Figs. 7c, 8c and 8f is noted that the optimal λ_k can be larger than 1.0, exceeding even the search domain $[-1, 1]$.

- Figs. 8a-8d illustrate the non-variational nature of the phase-field model, where energy and derivative slopes disagree. The optimal λ_k minimizes $\tilde{\mathcal{E}}_\lambda$ rather than energy.

- The proposed line search performs satisfactorily even in extreme cases, such as shown in Figs. 7d and 8f, where is observed a high difference in $\tilde{\mathcal{E}}_k < \tilde{\mathcal{E}}_{k+1}$ for $\lambda = 1.0$.

- Since only gradients are required, this method is computationally more efficient than alternatives requiring energy information. Experiments showed an average of five iterations to find optimal λ_k.

- The L-BFGS algorithm (equations Eq. (4.13) or Eq. (4.16)) solely is not capable of solving problems at critical steps, as the one shown in Fig. 7 and 8. In such situations, the proposed line search is capable of giving control to the L-BFGS algorithm, avoiding divergence.

Figure 7 – **Bar under tension** (see section 5.1 for further details): The line search parameter computed for the step where the crack nucleates and propagates (step 51). The *pseudo* energy $\tilde{\mathcal{E}}$ is scaled by a factor of 10^3 to aid visual inspection. These results are for the `AT2` model.

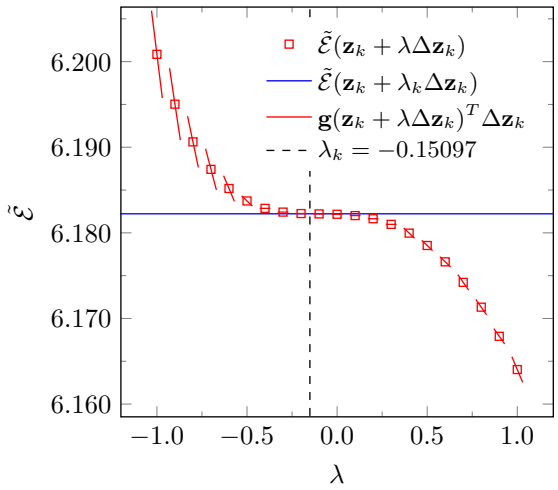

(a) Step 51: Iter. 53

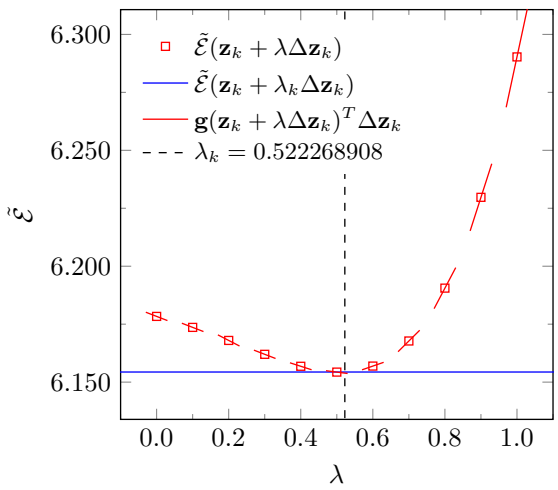

(b) Step 51: Iter. 57

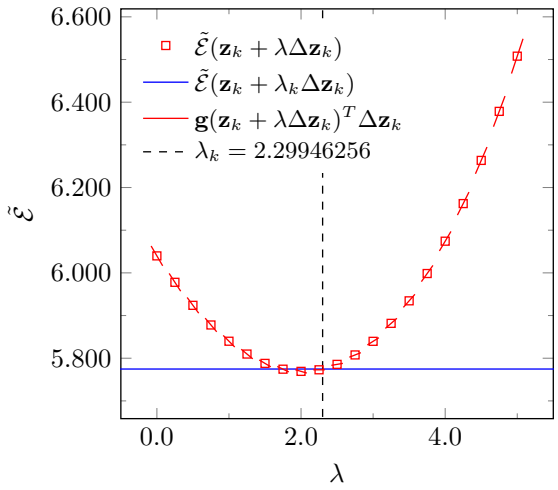

(c) Step 51: Iter. 61

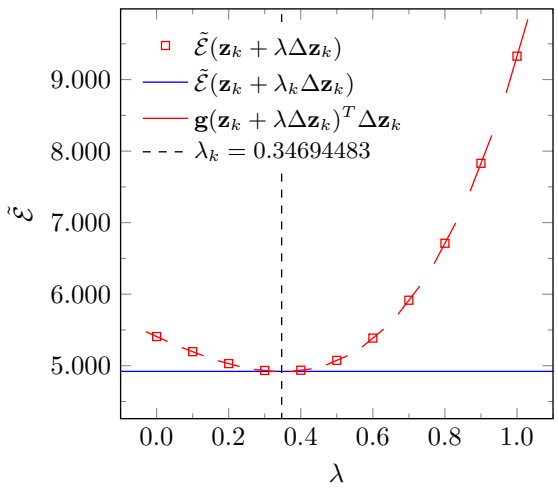

(d) Step 51: Iter. 63

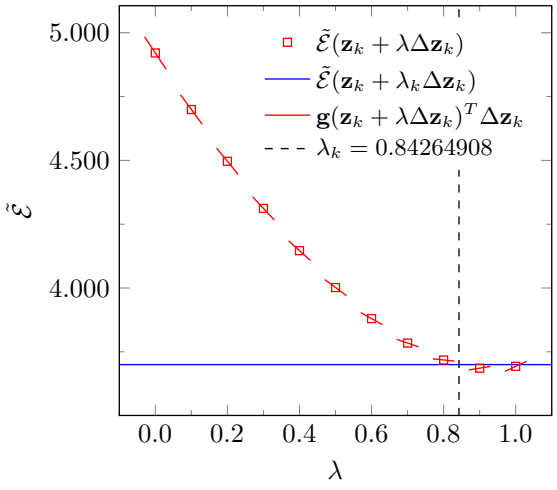

(e) Step 51: Iter. 64

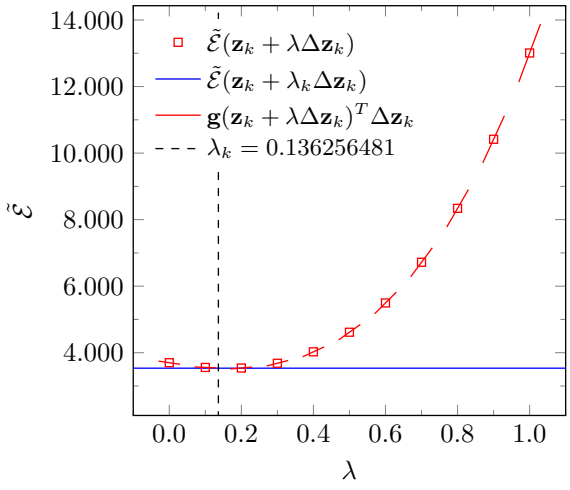

(f) Step 51: Iter. 65

Source: The author.

Figure 8 – **Bar under tension** (see section 5.1 for further details): The line search parameter computed for the step where the crack nucleates and propagates (step 51). The *pseudo* energy $\tilde{\mathcal{E}}$ is scaled by a factor of 10^3 to aid visual inspection. These results were obtained using the `AT2` model.

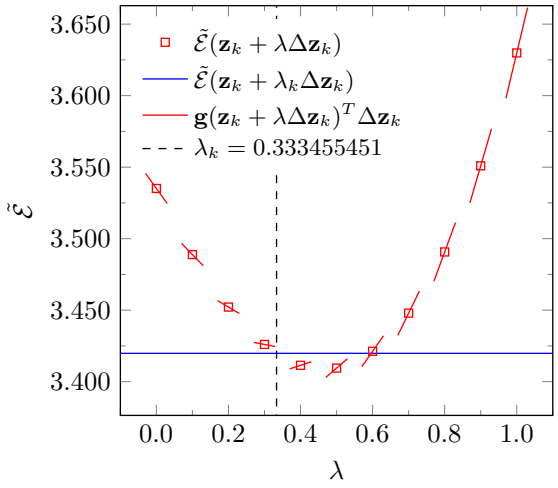

(a) Step 51: Iter. 66

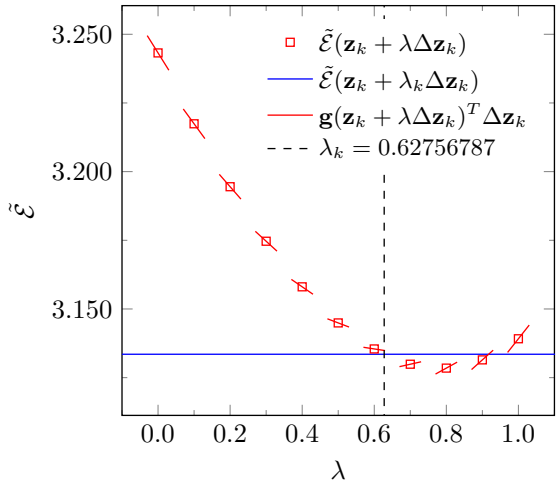

(b) Step 51: Iter. 68

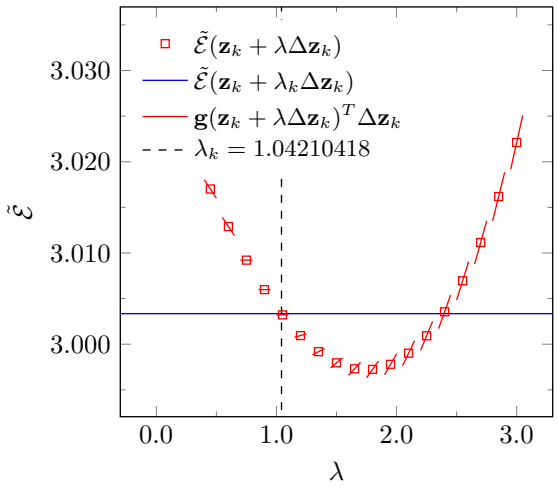

(c) Step 51: Iter. 73

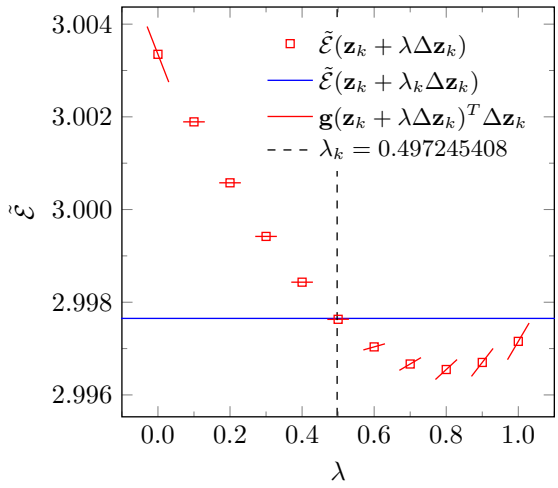

(d) Step 51: Iter. 74

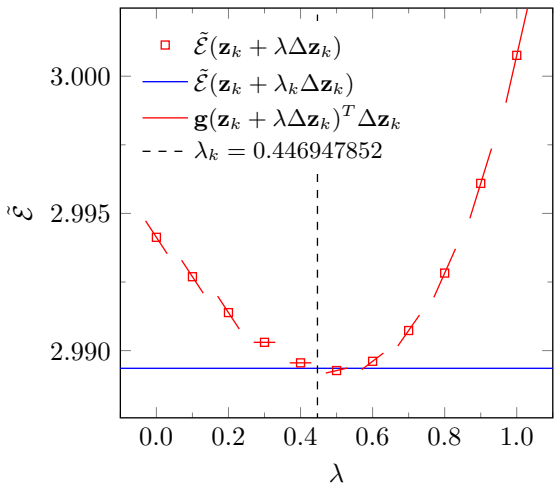

(e) Step 51: Iter. 76

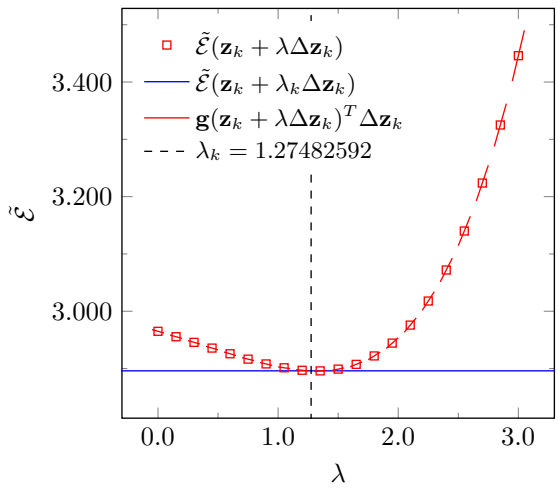

(f) Step 51: Iter. 82

Source: The author.

4.3.2 Combining the L-BFGS and ORAM

The Limited-memory Broyden-Fletcher-Goldfarb-Shanno method demonstrates excellent computational performance in terms of convergence speed and memory usage for phase-field fracture problems. However, its effectiveness diminishes significantly in the presence of unstable crack propagation phenomena. This limitation arises from the quasi-Newton approximation's inability to capture the rapid changes in the curvature of the objective function during critical loading steps where crack nucleation and propagation occur. For instance, analyzing Fig. 5 and 4d, it is observed that the Over-Relaxed Alternating Minimization (ORAM) method, with relaxation parameter $\omega = 1.8$, provides superior convergence characteristics for steps involving brutal crack propagation.

To harness the computational advantages of both methodologies, a novel hybrid solution scheme is proposed, termed BORAM (Hybrid L-**B**FGS **ORAM** algorithm). The fundamental principle underlying BORAM is the adaptive switching between L-BFGS and ORAM based on real-time convergence behavior analysis. This approach enables the algorithm to exploit the computational efficiency of L-BFGS during stable loading phases while automatically transitioning to the more robust ORAM methodology when challenging crack propagation scenarios are detected.

The BORAM algorithm draws inspiration from the work of Storvik *et al.* [36], where Anderson acceleration is combined with ORAM for enhanced computational performance. However, the present approach introduces methodological improvements specifically tailored for phase-field fracture mechanics. The algorithm employs L-BFGS as the default solver and activates ORAM based on intelligent detection of crack propagation events.

The switching mechanism is grounded in the fundamental observation that residual behavior patterns differ markedly between stable quasi-static loading and unstable crack propagation phases. While Storvik *et al.* [36] demonstrated that residuals of the alternating minimization method decrease monotonically during quasi-static steps, crack propagation stages exhibit increasing, oscillating, and stagnant behaviors [24] (see Fig. 9a). A key innovation in BORAM is the recognition that L-BFGS residual norms exhibit naturally oscillatory patterns, as illustrated in Fig. 9b, which precludes the direct application of strictly decreasing residual criteria used in previous approaches.

To overcome this limitation, BORAM implements a convergence rate analysis based on semi-logarithmic linear regression of residual norms. This approach provides a robust statistical foundation for detecting the onset of crack propagation, enabling seamless transitions between solution methodologies. The algorithm's adaptive nature ensures optimal computational efficiency across all loading phases, from initial elastic deformation through complex crack propagation scenarios.

The key idea is to perform a semi-log linear curve fitting using the previous N_s

Figure 9 – **Bar under tension** (see section 5.1 for further details): Convergence of the AM and L-BFGS algorithm for steps close to a brutal crack propagation (step 51). These results refer to the `AT2` model, see section 5.1 for further details.

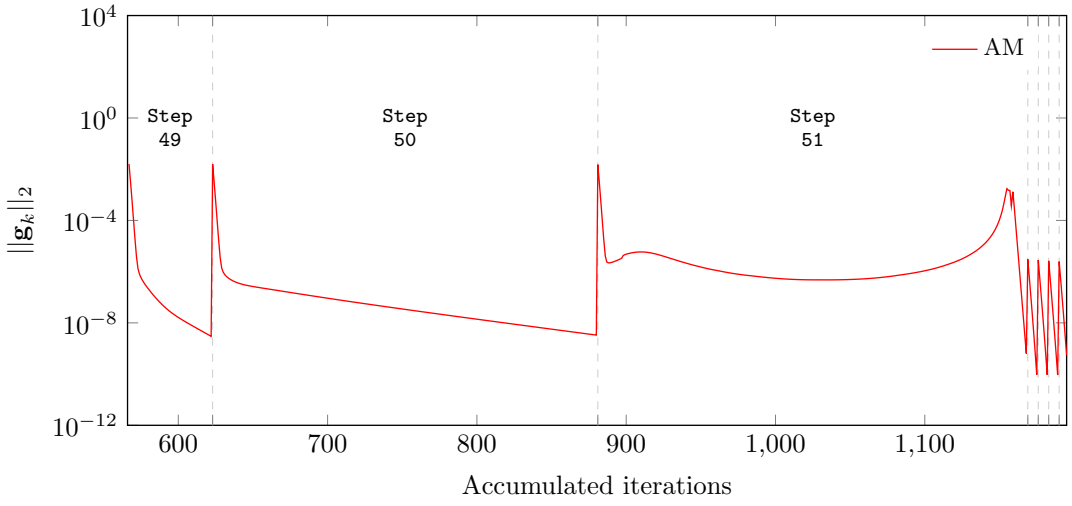

(a)

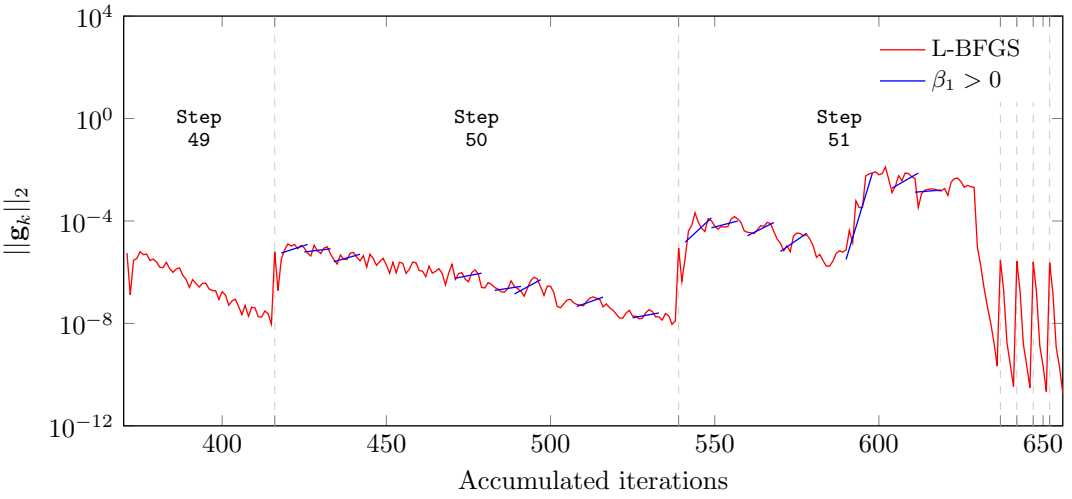

(b)

Source: The author.

residual norms and evaluate the slope parameter. Let us assume that, for a given step n, the residual norms convergence can be expressed as $f(\mathrm{It}) = 10^{(\beta_0+\beta_1 \mathrm{It})}$, where It refers to the iteration number. Applying the logarithm to the trend line function, we obtain that $\log(f(\mathrm{It})) = \beta_0 + \beta_1 \mathrm{It}$. The problem can be rewritten in algebric notation, such that

$$\begin{pmatrix} \bar{\mathrm{g}}_k \\ \bar{\mathrm{g}}_{k-1} \\ \vdots \\ \bar{\mathrm{g}}_{k-\mathrm{N}_s} \end{pmatrix} = \begin{pmatrix} 1 & \mathrm{It}_k \\ 1 & \mathrm{It}_{k-1} \\ \vdots & \vdots \\ 1 & \mathrm{It}_{k-\mathrm{N}_s} \end{pmatrix} \begin{pmatrix} \beta_0 \\ \beta_1 \end{pmatrix} \tag{4.27}$$

where $\bar{\mathrm{g}}_k := \log(||\mathbf{g}_k||_2)$. Let the sum of the squares of the errors function be described as

$$\begin{aligned} \mathrm{E}(\boldsymbol{\beta}) &:= (\bar{\mathbf{g}} - \mathbf{M}_{\mathrm{It}}\boldsymbol{\beta})^T(\bar{\mathbf{g}} - \mathbf{M}_{\mathrm{It}}\boldsymbol{\beta}) \\ &:= \bar{\mathbf{g}}^T\bar{\mathbf{g}} - \bar{\mathbf{g}}^T\mathbf{M}_{\mathrm{It}}\boldsymbol{\beta} - \boldsymbol{\beta}^T\mathbf{M}_{\mathrm{It}}^T\bar{\mathbf{g}} + \boldsymbol{\beta}^T\mathbf{M}_{\mathrm{It}}^T\mathbf{M}_{\mathrm{It}}\boldsymbol{\beta}, \end{aligned} \tag{4.28}$$

where $\bar{\mathbf{g}}$ is the vector of the logarithm of the residual norms, $\mathbf{M}_{\mathrm{It}}$ the matrix of the iteration values, and $\boldsymbol{\beta}$ the vector of unknowns. The parameters β_0 and β_1 are obtained by minimizing above equation, i.e.,

$$\begin{aligned} \frac{\partial \mathrm{E}(\boldsymbol{\beta})}{\partial \boldsymbol{\beta}} &= -2\mathbf{M}_{\mathrm{It}}^T\bar{\mathbf{g}} + 2\mathbf{M}_{\mathrm{It}}^T\mathbf{M}_{\mathrm{It}}\boldsymbol{\beta} = 0 \\ \boldsymbol{\beta} &= \left(\mathbf{M}_{\mathrm{It}}^T\mathbf{M}_{\mathrm{It}}\right)^{-1}\mathbf{M}_{\mathrm{It}}^T\bar{\mathbf{g}}. \end{aligned} \tag{4.29}$$

Fig. 9b shows regions on the convergence process of the L-BFGS where $\beta_1 > 0$, demonstrating that this parameter can be used to predict a possible crack propagation. By defining a user-defined convergence rate $\texttt{TOL}_{\texttt{conv}}$ to switch between the methods, the pseudo-code below describes the proposed algorithm, called BORAM (Hybrid L-**B**FGS **ORAM** algorithm).

Algorithm 5: BORAM algorithm

```
Given (u^h_{n-1}, φ^h_{n-1}), H_{n-1}, ū_n, m, ω, N_s, and tolerances.
Initialize k = 0, β_1 = TOL_conv − 1.
while not converged do
    if β_1 < TOL_conv then
        apply L-BFGS (Alg. 3)
    else
        apply ORAM (Alg. 2)
    end
    if k > N_s then
        compute β_1 (Eq. (4.29))
    end
    store ḡ_k
    k = k + 1
end
Set (u^h_n, φ^h_n) = (u_k, φ_k), and H_n = H_k
```

4.3.3 Stopping criterion

To avoid an inaccurate solution, an adequate stop or convergence criterion is necessary to terminate the iterative process. In the literature, several options have been considered. For instance, [24, 111] monitor an intricate norm of total energy to achieve convergence (see [111] for details). Furthermore, [6, 87] evaluate solely the variation of the nodal phase-field damage variable between two consecutive iterations and stop the process when the variation is below a certain threshold. In [24, 107, 133] the control of the residual norm is applied to ensure an accurate solution.

Following the ABAQUS [42] criterion for L-BFGS, where both the residue and solution are monitored, in this work, the iterative process terminates when both fields satisfy the following conditions:

$$\begin{aligned} \frac{||\boldsymbol{u}_k^h - \boldsymbol{u}_{k-1}^h||_2}{|||\boldsymbol{u}_1^h - \boldsymbol{u}_0^h||_2} \leq \texttt{TOL}_{\text{Inc}} \quad \frac{||\mathbf{r}^{\boldsymbol{u}}(\boldsymbol{u}_k^h,\, \phi_k^h)||_2}{||\mathbf{r}^{\boldsymbol{u}}(\boldsymbol{u}_0^h,\, \phi_0^h)||_2} \leq \texttt{TOL}_{\text{Res}}, \\ \frac{||\phi_k^h - \phi_{k-1}^h||_2}{|||\phi_1^h - \phi_0^h||_2} \leq \texttt{TOL}_{\text{Inc}} \quad \frac{||\mathbf{r}^{\phi}(\boldsymbol{u}_k^h,\, \phi_k^h)||_2}{||\mathbf{r}^{\phi}(\boldsymbol{u}_1^h,\, \phi_0^h)||_2} \leq \texttt{TOL}_{\text{Res}}. \end{aligned} \tag{4.30}$$

It is worth mentioning that all algorithms are subjected to the convergence criteria defined above, and implemented in the same programming environment.

5 NUMERICAL EXAMPLES

As the aim of this chapter is to demonstrate the effectiveness of the proposed algorithm, several numerical representative examples with both brittle and quasi-brittle failure in either mode-I and mixed-mode are considered. Both `AT2` and `CZM` phase-field damage models are applied, and the numerical performance of each model is compared for the AM, L-BFGS and BORAM algorithms. All algorithms are implemented in an in-house `C++` Finite Element code. The Tab. 2 shows the parameters used in the numerical examples for each algorithm. The performance of each algorithm is evaluated using a normalized time variable $\bar{T}$, given by the following equation:

$$\bar{T} = \frac{T_n}{T_{\text{AM}}}, \tag{5.1}$$

which T_n represents the accumulated time required for each algorithm to reach step n, and T_{AM} represents the total time used by AM algorithm to completely simulate a given problem. Furthermore, for L-BFGS and BORAM , each matrix updated is counted as an iteration. It is noted that this is not the case for the L-BFGS implementation available in ABAQUS [42], where the total number of iterations is based on an average using the m parameter. It is important to emphasize that the line search procedure is considered in all analyses with the L-BFGS algorithm.

Table 2 – Parameter values of the solution algorithms used in all examples.

Parameter	Symbol	Value	AM	L-BFGS	BORAM
Relative increment tol.	$\texttt{TOL}_{\text{Inc}}$	10^{-2}	✓	✓	✓
Relative residual tol.	$\texttt{TOL}_{\text{Res}}$	10^{-3}	✓	✓	✓
Relaxation parameter	ω	1.8			✓
Number of matrix updates	m	8		✓	✓
Line search activation tol.	$\texttt{TOL}_{\texttt{LS}}^{\texttt{act}}$	10^{-5}		✓	✓
Line search convergence tol.	$\texttt{TOL}_{\texttt{LS}}$	10^{-4}		✓	✓
Maximum convergence rate	$\texttt{TOL}_{\texttt{conv}}$	-0.05			✓
Iteration range to evaluate convergence rate	N_s	8			✓

Source: The author.

Plane stress state is assumed in all numerical examples, where E, ν, $\mathcal{G}_c$, ℓ are the material properties required for `AT2`, while `CZM` also requires f_t and a softening law, which is assumed to be linear in all cases, unless otherwise indicated. The energy criterion $\bar{\mathcal{H}} = \psi_0^+(\boldsymbol{\varepsilon})$ is applied to `AT2` model as the crack driving force, while `CZM` uses the Rankine criterion (see Eq. (3.61)). If strain energy decomposition is not required, the `AT2` crack driving force

is given by $\bar{\mathcal{H}} = \psi_0(\boldsymbol{\varepsilon})$. The computational domain is discretized in quadrilateral bilinear finite elements generated by Gmsh [134]. Unless otherwise indicated, all examples are 1 mm thick. The sub-domain where crack propagation is expected to occur is discretized by a fine mesh with size $h \leq \ell/5$, while the rest of the domain is discretized by a coarse mesh. If there is no *a priori* knowledge available of where the crack will propagate, a structured uniform discretization is applied to the whole computational domain. Following [95, 97, 99, 135], a single length scale is assumed for each example, such that $\ell \leq \ell_{\text{ch}}/3$. Initial cracks are modeled via geometry and mesh discretization. An Intel(R) Core(TM) i7-8750H CPU @ 2.20GHz with 16 GB RAM was used to run all numerical experiments.

5.1 Bar under tension - BUT

Consider a bar of length $L = 200$ mm and aspect ratio $L/H = 10$, subjected to a monotonically increasing and fixed displacement at the right and left edge, respectively, as shown in Fig. 10. Following [97], the material properties are $E = 30$ kN/mm^2, $\mathcal{G}_c = 1.2 \times 10^{-4}$ kN/mm, $\nu = 0.2$, and $f_t = 3 \times 10^{-3}$ kN/mm^2, leading to a $\ell_{\text{ch}} = 400$ mm. A length scale $\ell = 10$ mm is adopted, and a uniform structured mesh with 1000 elements of size $h = 2$ mm is adopted for all numerical experiments. Due to the load being strictly tensile, for this example, no decomposition of the strain energy into compressive and tensile parts is applied.

Figure 10 – **Bar under tension**: Geometry and boundary conditions.

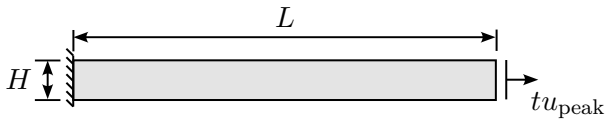

Source: The author.

The non-homogeneous Dirichlet boundary condition is defined based on the limit displacement u_{peak} computed using the peak stress σ_{peak} of each phase-field model. Invoking the analytical solution for a 1D bar under traction provided by the gradient-damage model proposed in [74] (see Eq. (3.28)), the $\sigma^{\texttt{AT2}}_{\text{peak}}$ and its displacement $u^{\texttt{AT2}}_{\text{peak}}$ for `AT2` model are given by

$$\sigma^{\texttt{AT2}}_{\text{peak}} = \sqrt{\frac{27E\mathcal{G}_c}{256\ell}}, \qquad u^{\texttt{AT2}}_{\text{peak}} = \frac{16}{9}\frac{\sigma^{\texttt{AT2}}_{\text{peak}} L}{E}. \tag{5.2}$$

Since the pre-peak behavior of the `CZM` model is linear (see Eq. (3.31)), the limit displacement can be computed directly by

$$u^{\texttt{CZM}}_{\text{peak}} = \frac{f_t L}{E}, \tag{5.3}$$

where f_t is the peak stress. A factor $0 < t \leq 3$ is used to scale the u_{peak} of each model and define the non-homogeneous Dirichlet boundary condition. The simulation is performed in

150 steps, which means that a propagation procedure is expected to start at step 50, i.e, $t = 1$. Fig. 11 depicts the normalized stress *versus* normalized displacement for `AT2` and `CZM` models. As observed, the peak stress is identical to the analytical solution for `AT2` model and the failure strength for `CZM` model. Additionally, the results for `CZM` obtained by [97] for this example are presented, and an agreement is observed. Only the results provided by BORAM algorithm are presented since the others two coincide. As shown next, the BORAM and L-BFGS algorithm requires fewer iterations and computation cost to converge than the AM algorithm.

In Fig. 12 is presented the number of iterations required by each algorithm to reach the convergence criterion. Only the first 100 increments are shown to facilitate the visualization. As observed, the AM algorithm requires more iterations than the others two. In general, the BORAM performs similarly to the L-BFGS, only activating the ORAM at increments around 50, where the crack propagation starts and the non-linearity of the problem is more pronounced.

Fig. 13 shows the relative computational cost of each algorithm. As observed, both the L-BFGS and BORAM algorithms are more efficient than the AM algorithm, being 5 times faster than the latter. Though the BORAM algorithm does not show a significant improvement in the computational cost compared to L-BFGS, the next examples provide a more significant difference.

Figure 11 – **Bar under tension**: Normalized stress *versus* normalized displacement.

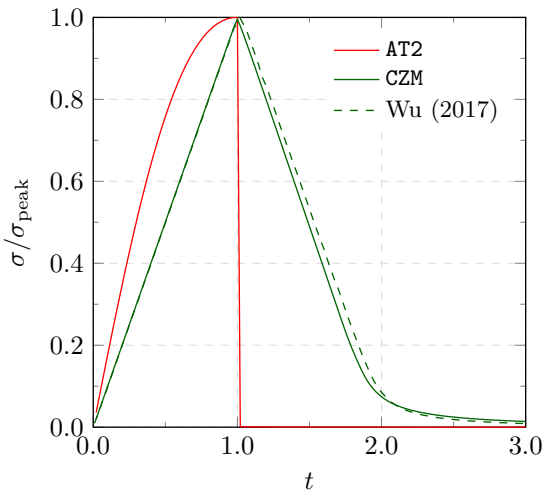

Source: The author.

Figure 12 – **Bar under tension**: Iteration number at each increment. Note that the crack starts to propagate at increment 51.

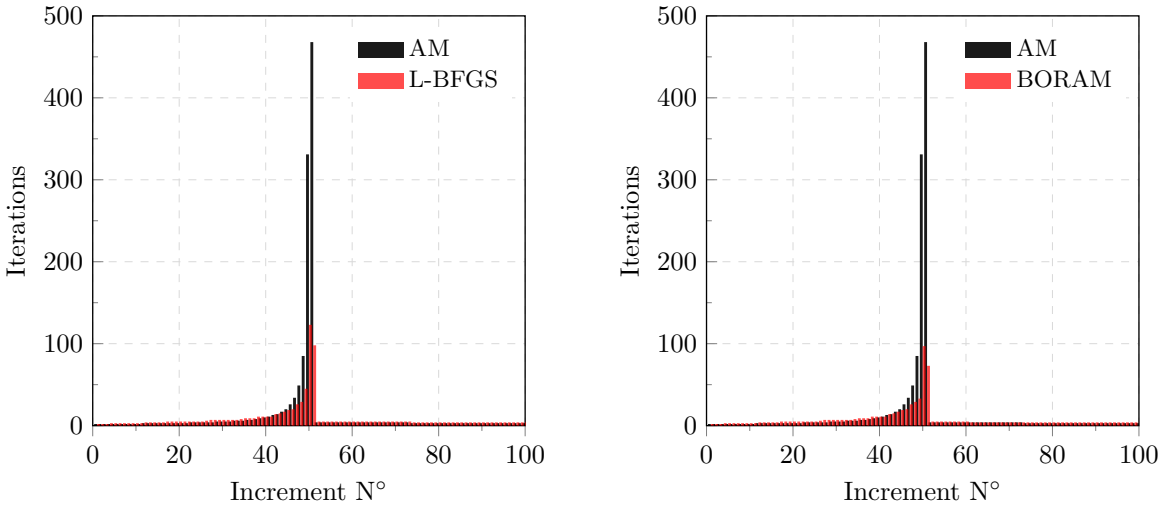

(a) `AT2` model

(b) `AT2` model

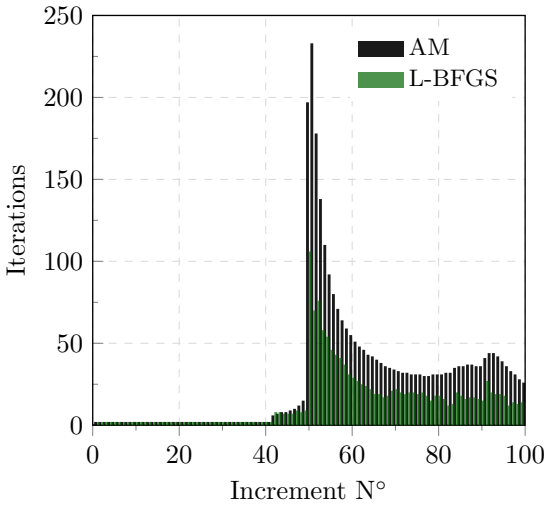

(c) `CZM` model

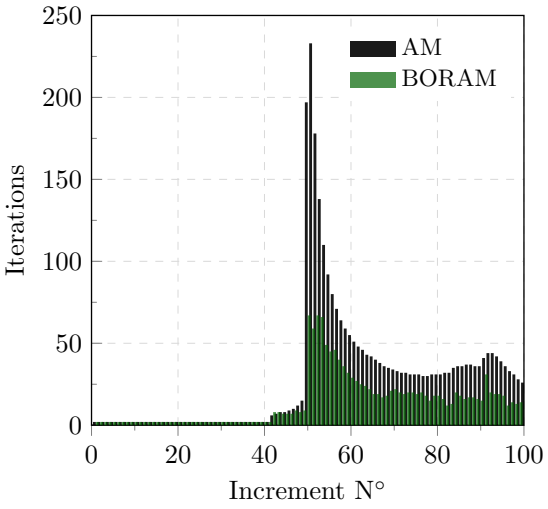

(d) `CZM` model

Source: The author.

Figure 13 – **Bar under tension**: Accumulated time at each increment.

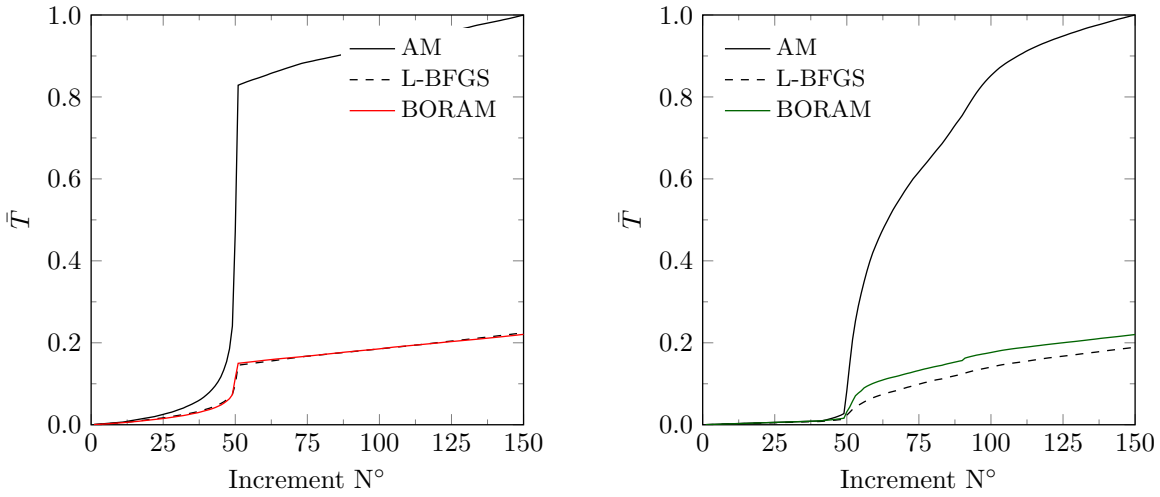

(a) `AT2` model (b) `CZM` model

Source: The author.

5.2 Single-edge notch plate

This section explores a popular benchmark to evaluate phase-field models in the context of brittle fracture [30, 99, 104]. As shown in Fig. 14, the problem consists of a square plate of length 1 mm with a pre-existing straight horizontal crack of length 0.5 mm located at the center of the left edge. The bottom edge is fixed, while the direction of the displacement applied to the top edge renders two problems: tension test subjected to a vertical displacement ($\theta = 90°$), and a shear test under horizontal displacement ($\theta = 0°$).

Figure 14 – **Single-edge notched plate**: Geometry (mm) and boundary conditions. The tensile and shear test cases are represented by $\theta = 90°$ and $\theta = 0°$, respectively.

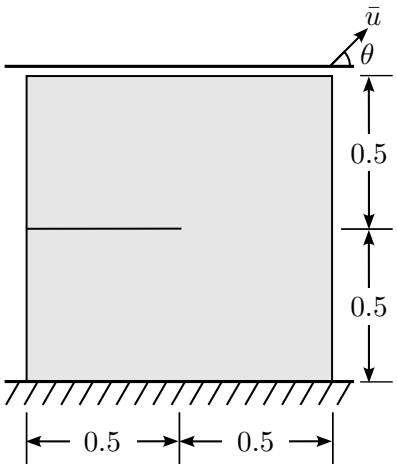

Source: The author.

The material properties are chosen as $E = 210$ kN/mm^2, $\mathcal{G}_c = 2.7 \times 10^{-3}$ kN/mm, $\nu = 0.3$, and $f_t = 2$ kN/mm^2 to match the parameters of the same example in [131], rendering $\ell_{\text{ch}} = 0.14$ mm. The mesh considers an *a priori* defined subdomain with a fine mesh of size $h = 0.001$ mm where the phase-field evolution is expected (see Fig. 15). A length scale $\ell = 0.005$ mm is adopted in all simulations.

Figure 15 – **Single-edge notched plate**: finite element discretizations. (a) Tensile test case (22,566 elements). (b) Shear test case (66,933 elements).

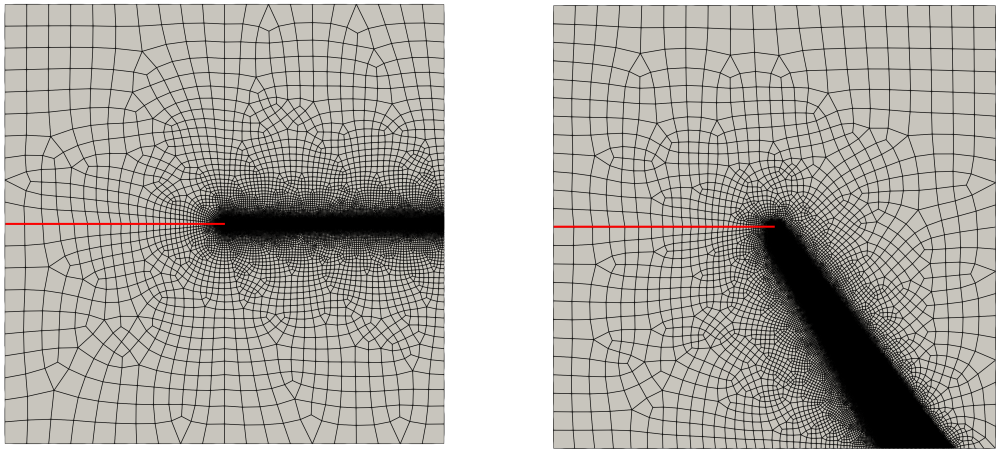

(a) (b)

Source: The author.

5.2.1 Tensile test case - SENPT

Let us first consider the tensile test case, where unstable crack growth through the specimen occurs instantaneously, as is shown in Fig. 16. In this test case, no split of the strain energy is required since the load is strictly tensile. Following [131], the prescribed vertical displacement $\bar{u} = 0.06$ mm is applied in two stages: the first 0.04 mm is applied in 20 equal increments, and the remaining 0.02 mm is applied in 100 equal increments.

The load-displacement curves are shown in Fig. 17, and it is observed they are in agreement with the results available in the literature [29, 131]. Moreover, since the results for all algorithms coincide, only the results of the BORAM algorithm are shown in Figs. 16 and 17.

Figure 16 – **Single-edge notched plate under tension**: Crack phase-field at displacement (a) $\bar{u} = 5.68 \times 10^{-3}$ mm and (b) $\bar{u} = 4.88 \times 10^{-3}$ mm

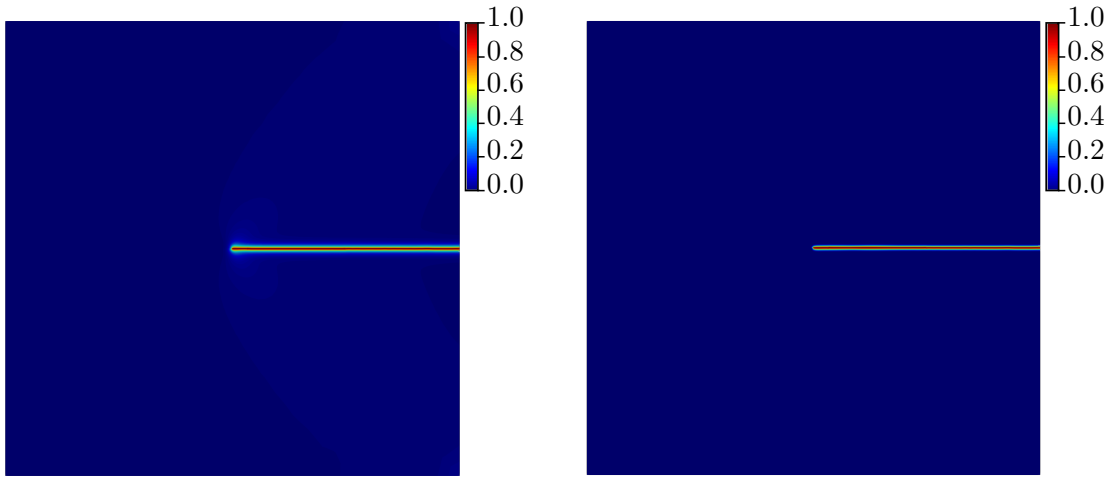

(a) `AT2` model (b) `CZM` model

Source: The author.

Figure 17 – **Single-edge notched plate under tension**: Load *versus* displacement curves.

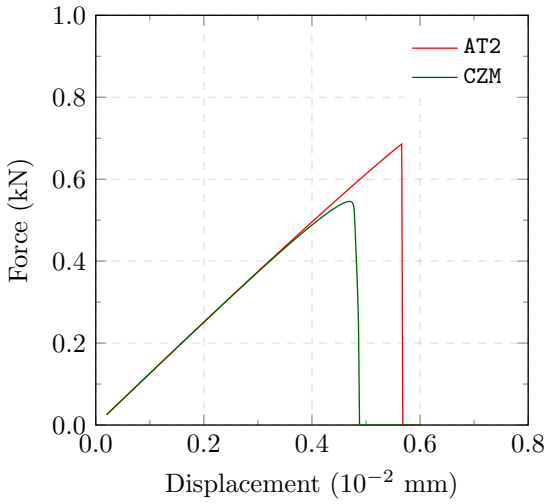

Source: The author.

Fig. 18 shows the number of iterations required by each algorithm to achieve convergence at each increment. Here, the BORAM algorithm provides an important reduction in the number of iterations required by `AT2` model to achieve convergence, mainly at the step with brutal crack propagation. The L-BFGS algorithm also leads to a reduction in the number of iterations, but not as significant as BORAM . However, for `CZM` model, the L-BFGS and BORAM algorithms show a similar performance, both requiring fewer iterations than the AM algorithm. In fact, the criteria employed to switch from L-BFGS to ORAM is not activated in this example, since the convergence rate is always positive.

Figure 18 – **Single-edge notched plate under tension**: Iteration number at each increment.

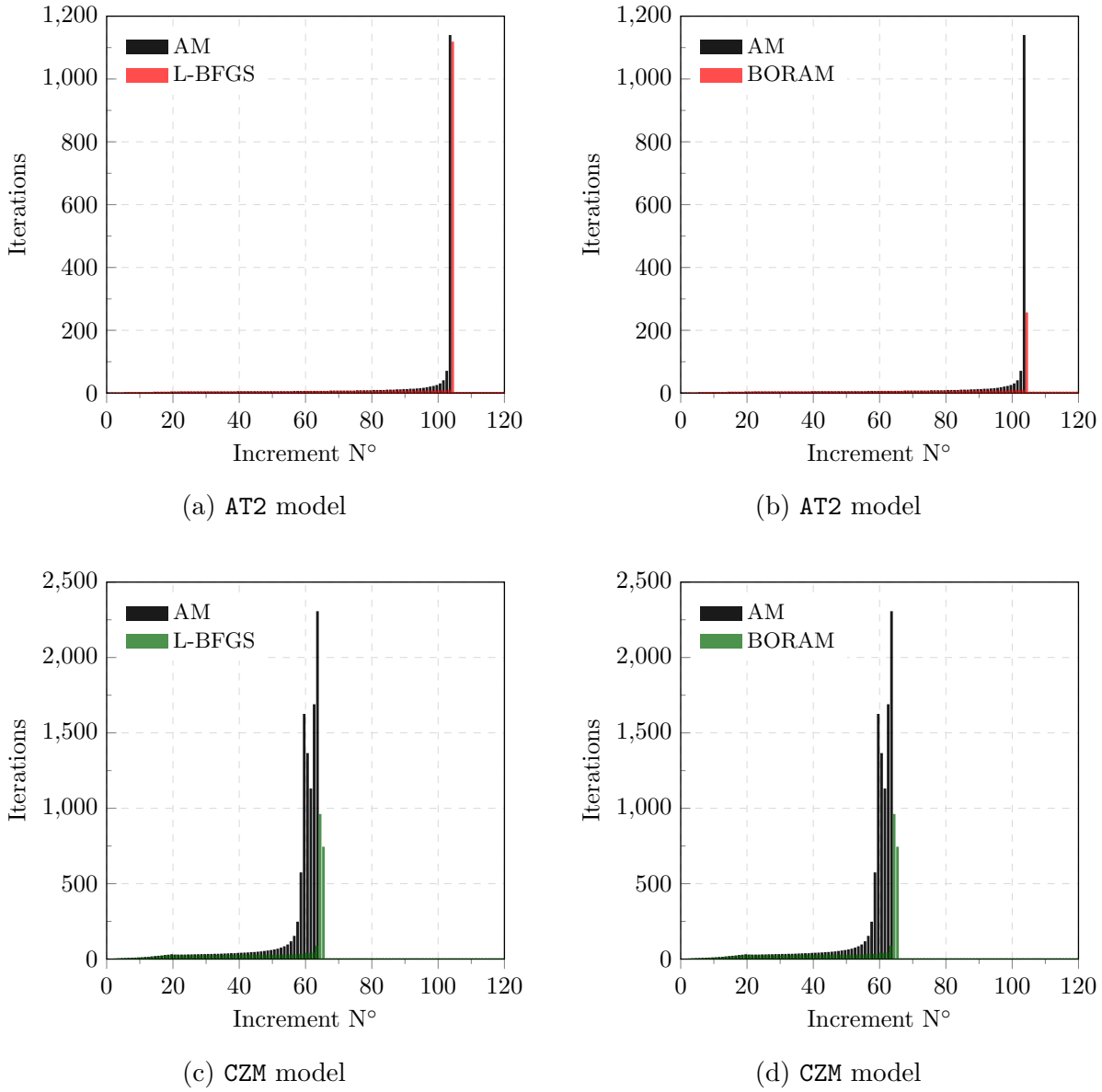

(a) `AT2` model

(b) `AT2` model

(c) `CZM` model

(d) `CZM` model

Source: The author.

The difference between all algorithms in terms of computational cost is shown in Fig. 19. As observed, the BORAM algorithm is about 5 times faster than the AM algorithm for `AT2` model, while L-BFGS is about 3 times faster than the AM algorithm. Interestingly, even though L-BFGS algorithm leads to a higher number of iterations than AM for the step with brutal crack propagation, the total time required to solve the problem is still lower. This is explained by the fewer reformations of the stiffness matrix per increment for the L-BFGS. For `CZM` model, the BORAM and L-BFGS algorithms are about 10 times faster than the AM algorithm.

Figure 19 – **Single-edge notched plate under tension**: Accumulated time at each increment.

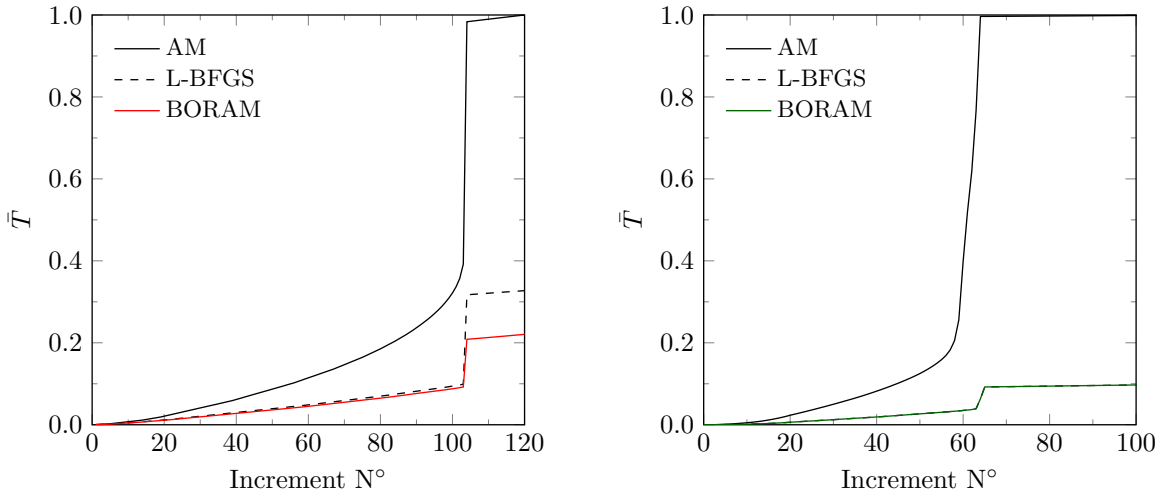

(a) `AT2` model (b) `CZM` model

Source: The author.

5.2.2 Shear test case - SENPS

The same specimen is now subject to shear loading, leading to a stable crack growth where the mixed-mode tip conditions produce a damage evolution towards the lower part of the sample. The crack pattern, shown in Fig. 20, is in agreement with results available in the literature [29, 104, 135].

Figure 20 – **Single-edge notched plate under shear**: Damage profile at displacement $\bar{u} = 0.02$ mm.

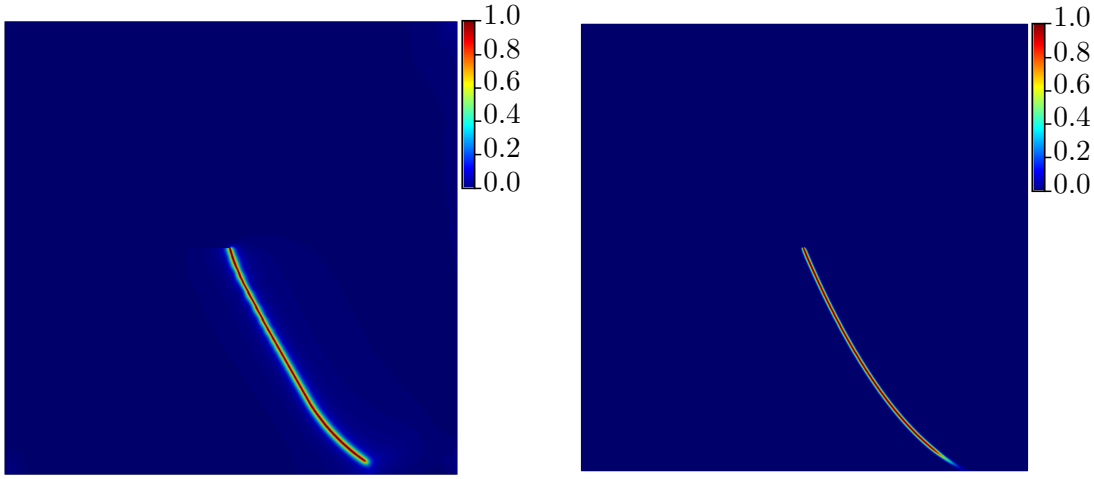

(a) `AT2` model (b) `CZM` model

Source: The author.

In this test case, a prescribed horizontal displacement $\bar{u} = 0.02$ mm is applied in 100 equal increments, as done by [131]. As is observed in Fig. 21, the load *versus*

displacement curves are consistent with those available in the literature [104, 135]. As the results of all algorithm options are the same, in Figs. 20 and 21 only the results of the BORAM algorithm are shown. Such observation demonstrates that the BORAM algorithm is able to solve the problem with the same accuracy as the L-BFGS and AM algorithms, only affecting the convergence properties of the algorithm, even in cases with complex crack patterns.

Figure 21 – **Single-edge notched plate under shear**: Load *versus* displacement curves.

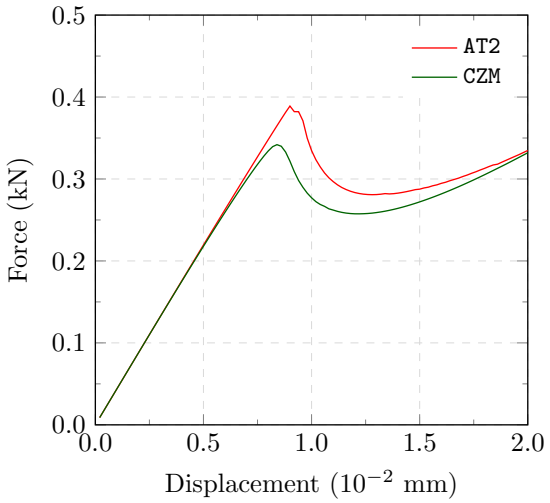

Source: The author.

Although all algorithms provide identical results, the number of iterations required to convergence is rather different, as we can see in Fig. 22. In fact, the BORAM and L-BFGS algorithms require much fewer iterations compared to AM solver. Additionally, the number of iterations in BORAM is even smaller compared to L-BFGS for both models.

Both BORAM and L-BFGS algorithms achieved a significant saving in CPU time compared to AM solver, leading to a total time around 10 times smaller than the AM algorithm, as shown in Fig. 23. However, the gains provided by BORAM is not so relevant for this example, specially for the `CZM` model, where L-BFGS outperforms BORAM . The computation cost of reforming the tangent matrix in BORAM is higher, even leading to a smaller number of iterations.

Figure 22 – **Single-edge notched plate under shear**: Iteration number at each increment.

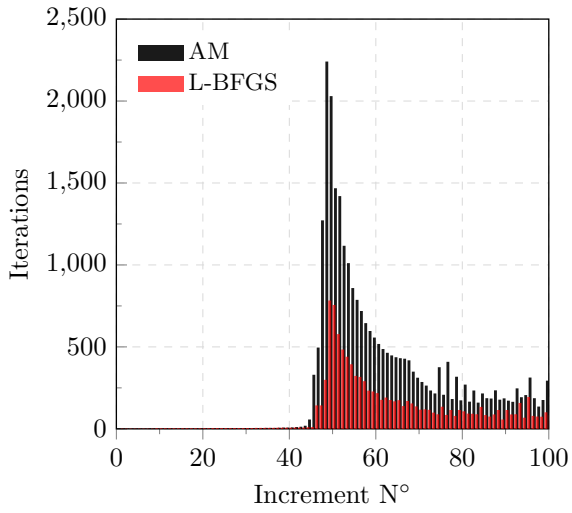

(a) `AT2` model

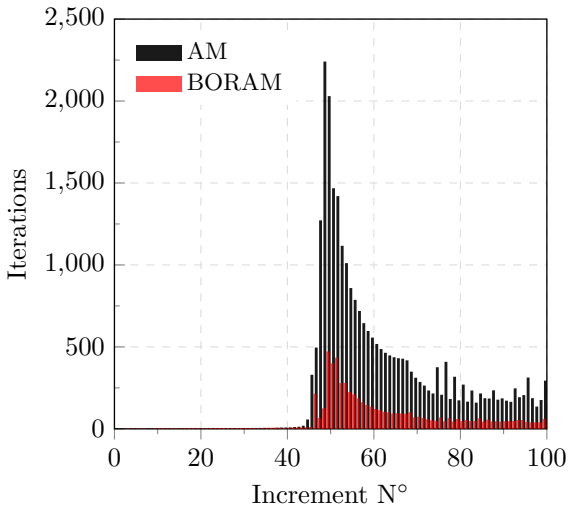

(b) `AT2` model

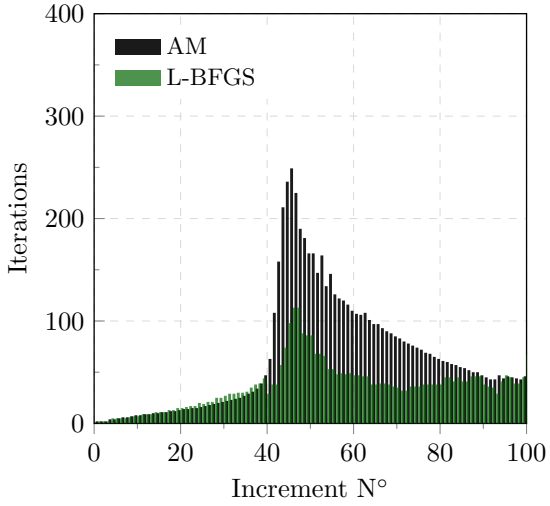

(c) `CZM` model

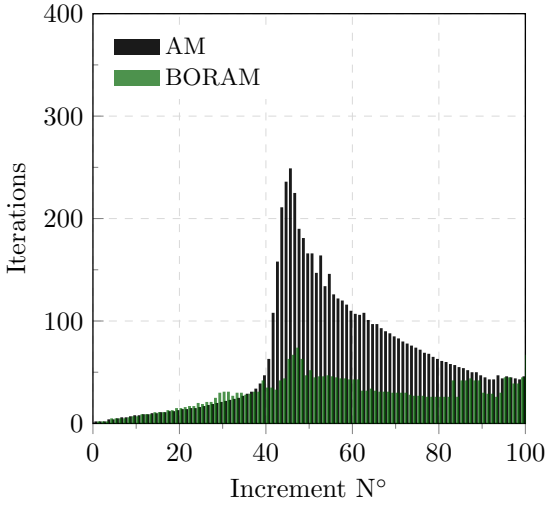

(d) `CZM` model

Source: The author.

Figure 23 – **Single-edge notched plate under shear**: Accumulated time at each increment.

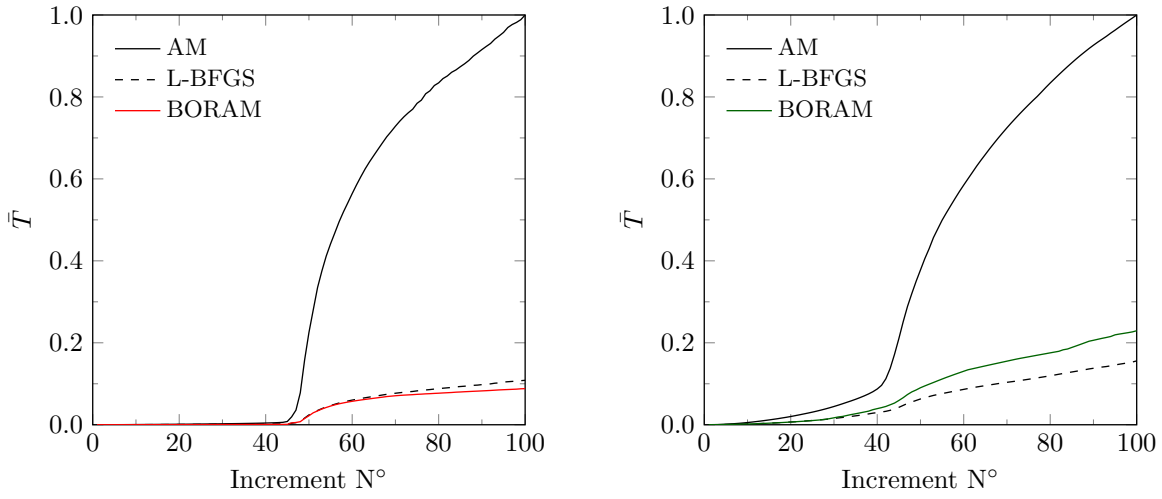

(a) `AT2` model (b) `CZM` model

Source: The author.

5.3 Symmetric three-point bending test - S3PBT

The symmetric three-point bending is a classical test used to study phase-field models for the brittle fracture behavior of materials [29, 111]. The specimen is subjected to a load at the center of the upper edge and two lateral constraints located at the ends of the lower edge of the specimen. The simulation setup is shown in Fig. 24. Following [99], the material properties are set as $E = 20.8$ kN/mm^2, $\mathcal{G}_c = 5.4 \times 10^{-4}$ kN/mm, $\nu = 0.3$, and $f_t = 2 \times 10^{-1}$ kN/mm^2. A length scale $\ell = 0.03$ mm is considered, much less than Irwin's characteristic length $\ell_{\text{ch}} = 0.28$ mm. An *a priori* refined mesh with elements of size $h = 0.002$ mm is used to discretize the expected crack propagation region (see Fig. 24b). The strain energy decomposition plays an important role in this case, since allowing damage under compression produces a small fracture zone near the applied load. Due to it, crack propagation can start from the loading area, instead of from the notch.

The simulation is performed using 100 load increments to apply the prescribed displacement of $\bar{u} = 0.08$ mm, as done by [99]. As expected, the crack propagation starts from the notch and vertically evolves towards the upper edge, which is depicted in Fig. 25. The load-displacement curves shown in Fig. 26 are in agreement with those obtained by [99, 130]. Since all the results of the algorithms coincide, only the BORAM are shown in Figs. 25 and 26.

Figure 24 – **Symmetric three-point bending test**: (a) Geometry (mm) and boundary conditions. (b) Finite element discretization (104,147 elements).

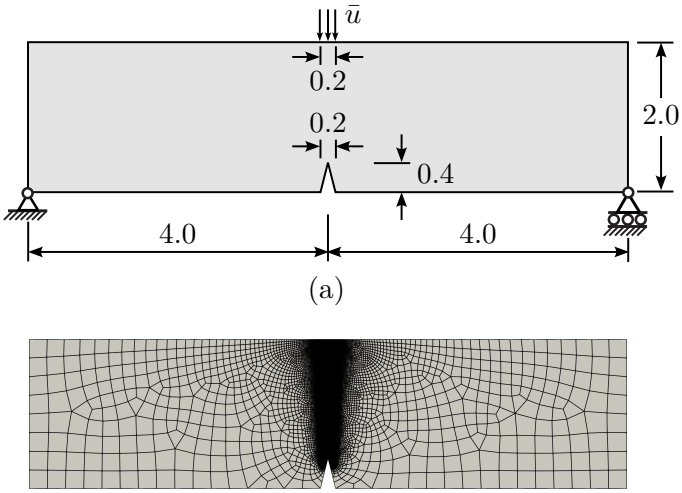

(a)

(b)

Source: The author.

Figure 25 – **Symmetric three-point bending test**: Damage profile at displacement $\bar{u} = 0.08$ mm.

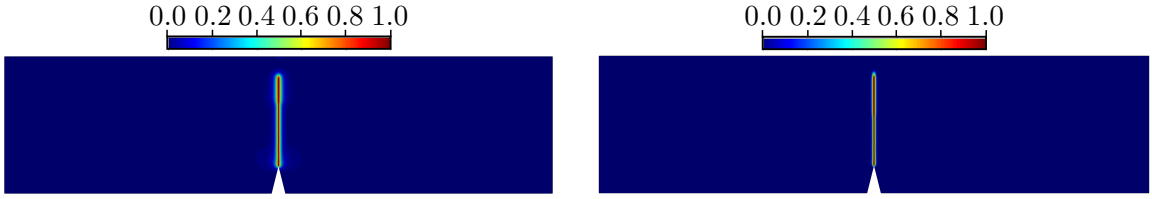

(a) `AT2` model (b) `CZM` model

Source: The author.

Figure 26 – **Symmetric three-point bending test**: Load *versus* displacement curves.

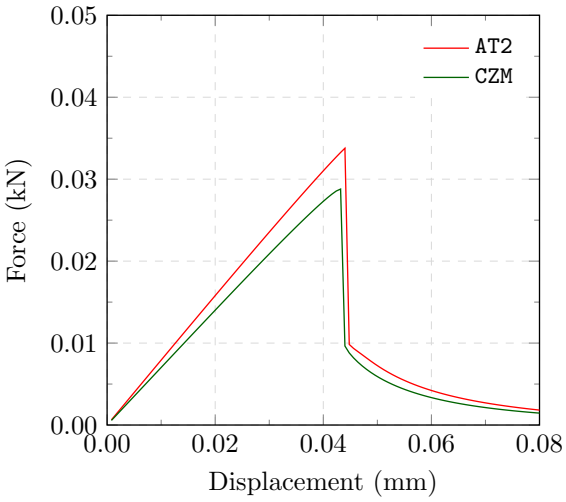

Source: The author.

The numerical performance of each algorithm is shown in Fig. 27 and 28. As observed, in all cases BORAM plays an important role in reducing the computational cost. Although the `AT2` model required 2,517 iterations for the L-BFGS algorithm to achieve convergence at increment 56, which is considerably greater than the 1,209 iterations for the AM algorithm, the total time taken was around five times smaller. Moreover, the BORAM algorithm is able to reduce the number of iterations required by L-BFGS algorithm, leading to a total of 419 iterations. Regarding the computational cost, BORAM is also more efficient than L-BFGS and AM for the `AT2` model. However, this gain is not observed for `CZM` model. Considering both models, we can conclude that in this case the L-BFGS and BORAM algorithms are about 5 times faster than the AM algorithm.

Figure 27 – **Symmetric three-point bending test**: Iteration number at each increment.

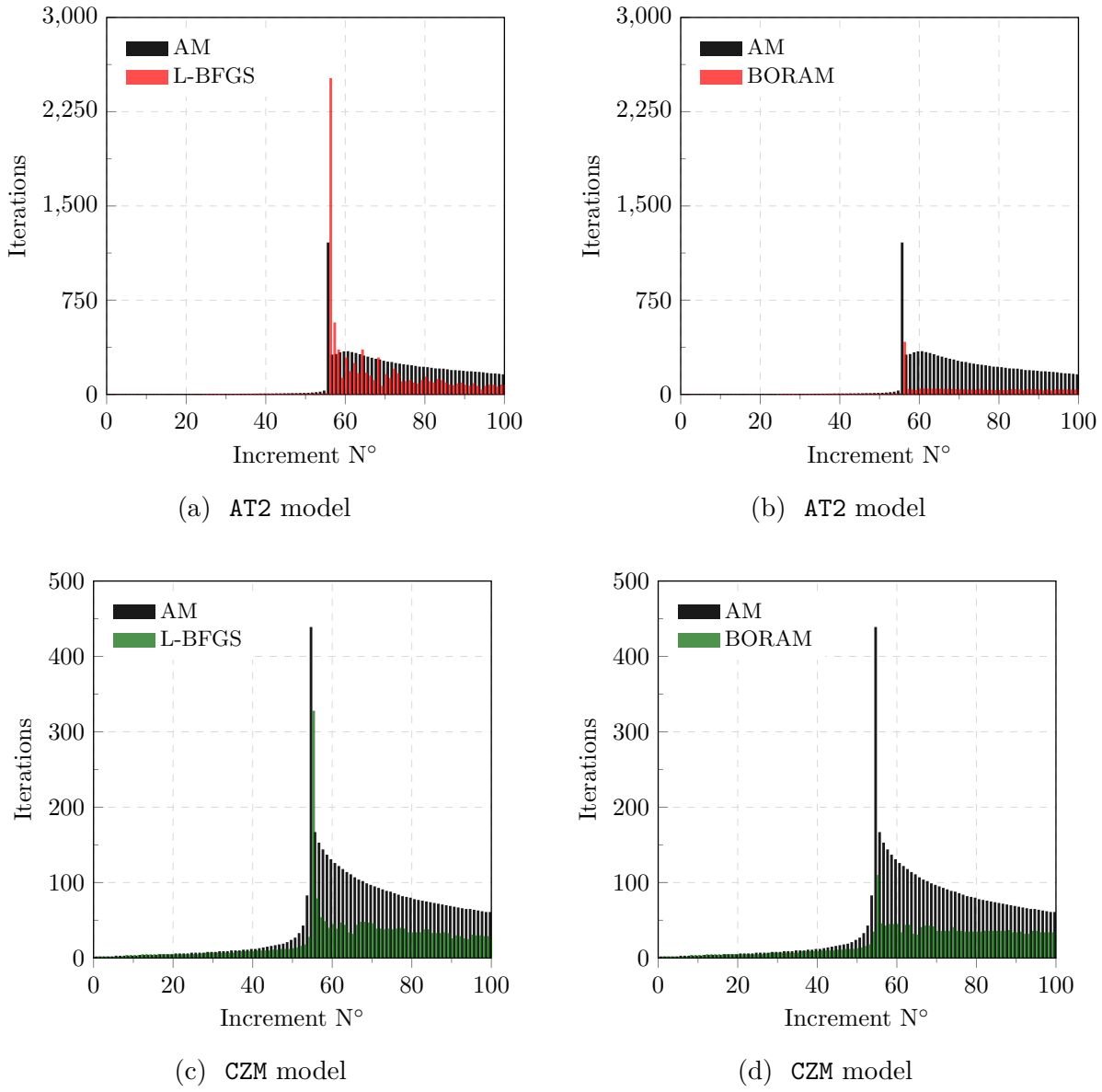

(a) `AT2` model

(b) `AT2` model

(c) `CZM` model

(d) `CZM` model

Source: The author.

Figure 28 – **Symmetric three-point bending test**: Accumulated time at each increment.

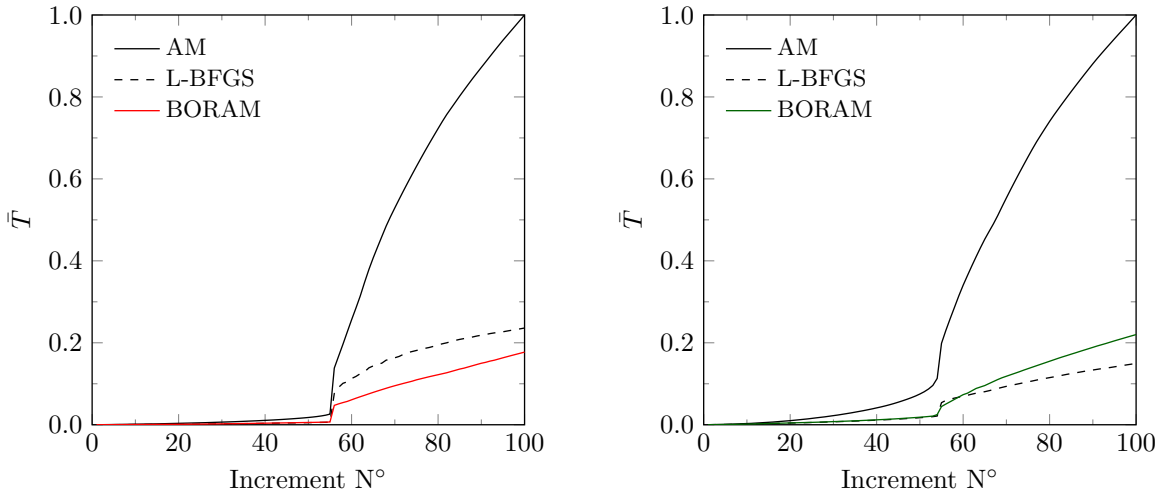

(a) `AT2` model (b) `CZM` model

Source: The author.

5.4 L-shaped panel - LSP

The mixed-mode failure test of a L-shaped panel conducted by [136] is now considered. This concrete L-shaped panel is a popular experiment used to evaluate and validate phase-field models [95,97,99,135]. The geometry, loading and boundary conditions of the specimen are shown in Fig. 29a. The bottom edge of the specimen is fixed, and a vertical point load is applied upward under displacement control at a distance of 30 mm to the right edge of the horizontal leg. The specimen has a thickness of 100 mm.

Figure 29 – **L-shaped panel**: (a) Geometry (mm) and boundary conditions. (b) Finite element discretization (20,053 elements).

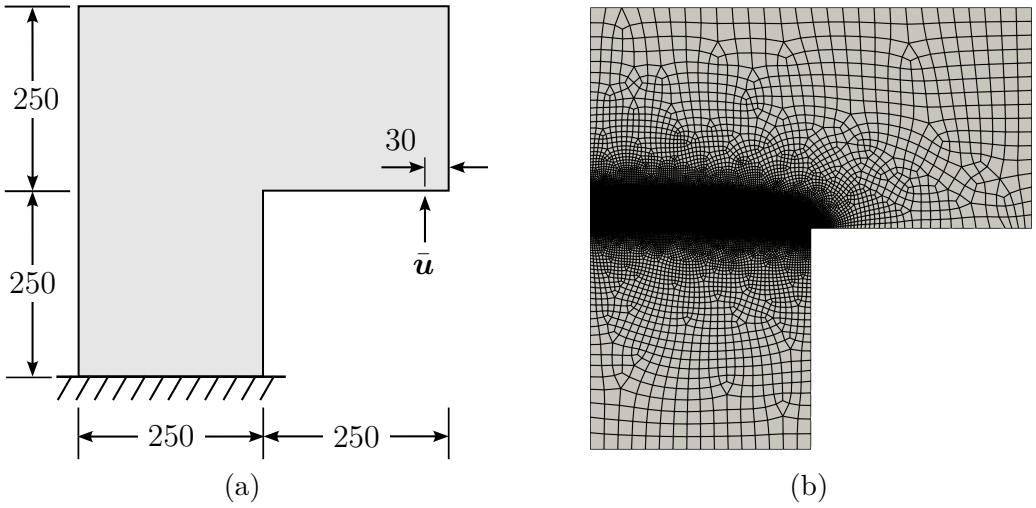

Source: The author.

The material properties are taken from the reference [136]: Young's modulus $E = 20$ kN/mm^2, Poisson's ratio $\nu = 0.18$, failure strength $f_t = 2.5 \times 10^{-3}$ kN/mm^2, and fracture energy $\mathcal{G}_c = 1.3 \times 10^{-4}$ kN/mm. The concrete softening law is employed in the analysis. A mesh with element size $h = 1$ mm is used to discretize the specimen in the expected crack propagation region (see Fig. 29b), and a length scale $\ell = 5$ mm is considered in all simulations. The prescribed vertical displacement $\bar{u} = 1.0$ mm is applied in 100 equal increments, as done by [97].

Though the specimen geometry and loading/boundary conditions are very simple, the numerical modeling of the L-shaped panel is rather challenging. The main difficulty arises from the mixed-mode crack propagation, which leads to a complex crack pattern. The phase-field evolution is expected to start at the corner and propagate towards left edge, as shown in Fig. 30. The load *versus* displacement curves are shown in Fig. 31, and it is observed that the results are in agreement with those available in the literature [97, 99]. Additionally, it is observed that the `AT2` model leads to a higher peak load compared to the `CZM` model, which is explained by the length scaled dependence of the `AT2` model, as discussed in [99]. The results of all algorithms coincide, so only the results of the BORAM algorithm are shown in Figs. 30 and 31.

Figure 30 – **L-shaped panel**: Damage profile at displacement $\bar{u} = 1.0$ mm.

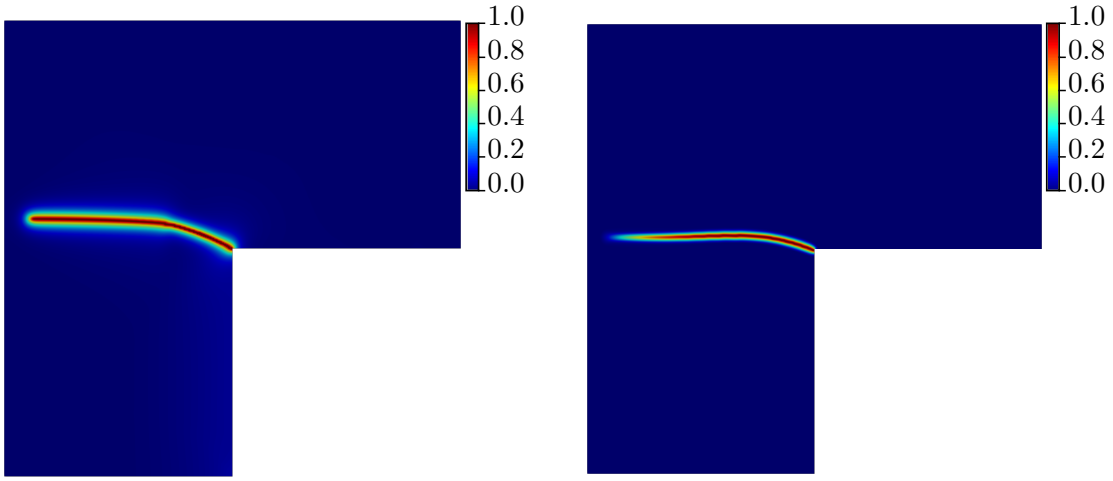

(a) `AT2` model (b) `CZM` model

Source: The author.

As observed in Fig. 32, both BORAM and L-BFGS algorithms lead to a significant reduction in the number of iterations required to achieve convergence compared to the AM algorithm for the `AT2` model. Additionally, the BORAM algorithm requires fewer iterations than L-BFGS for the step where the crack starts to propagate. For the `CZM` model, only BORAM shows a significant reduction in the number of iterations compared to AM algorithm.

Figure 31 – **L-shaped panel**: Load *versus* displacement curves.

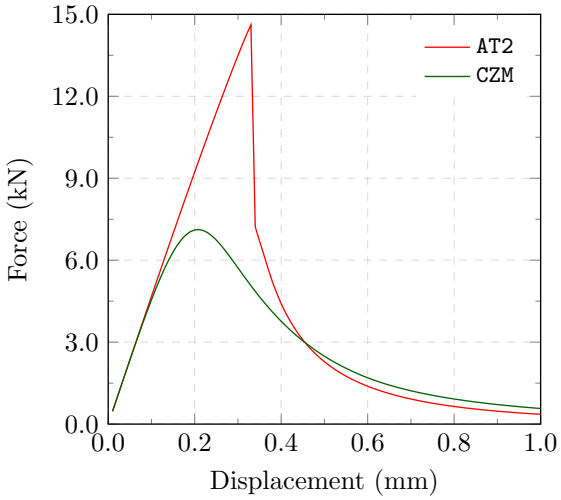

Figure 32 – **L-shaped panel**: Iteration number at each increment.

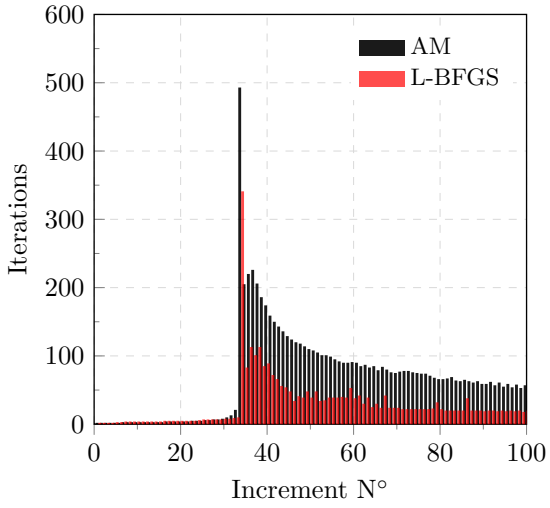

(a) `AT2` model

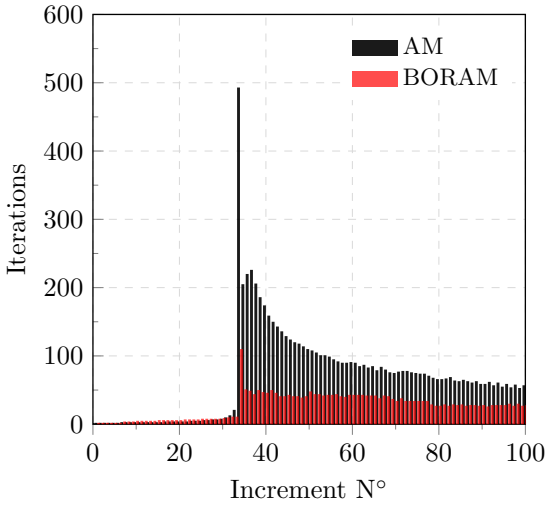

(b) `AT2` model

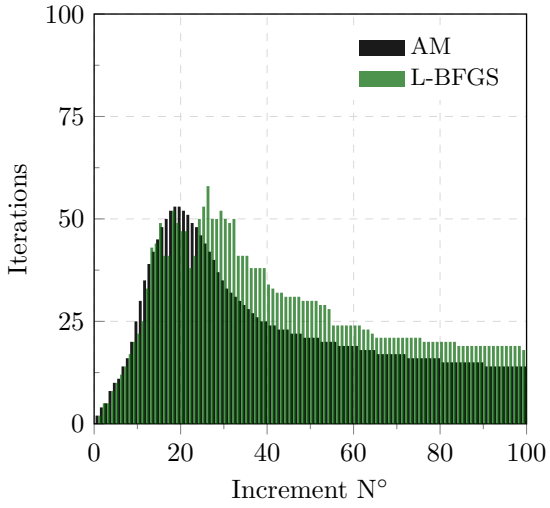

(c) `CZM` model

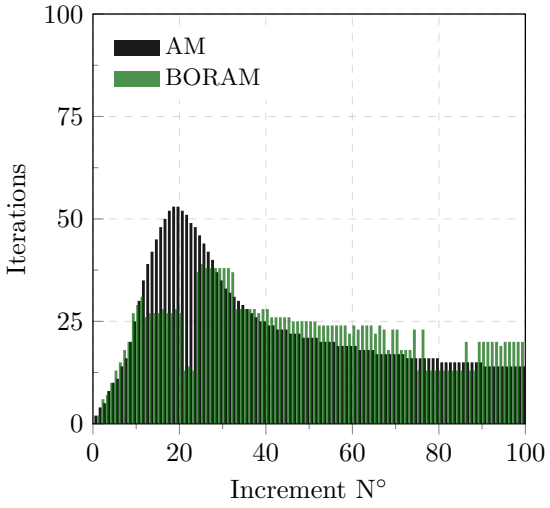

(d) `CZM` model

In relation to the computational cost, both L-BFGS and BORAM provide considerable savings in CPU time compared to the AM algorithm for the `AT2` and `CZM` models, as shown in Fig. 33. In general, all algorithms performed similarly for both models, where L-BFGS and BORAM are about 5 times faster than the AM algorithm for `AT2` model, and about 2 times faster for `CZM` model.

Figure 33 – **L-shaped panel**: Accumulated time at each increment.

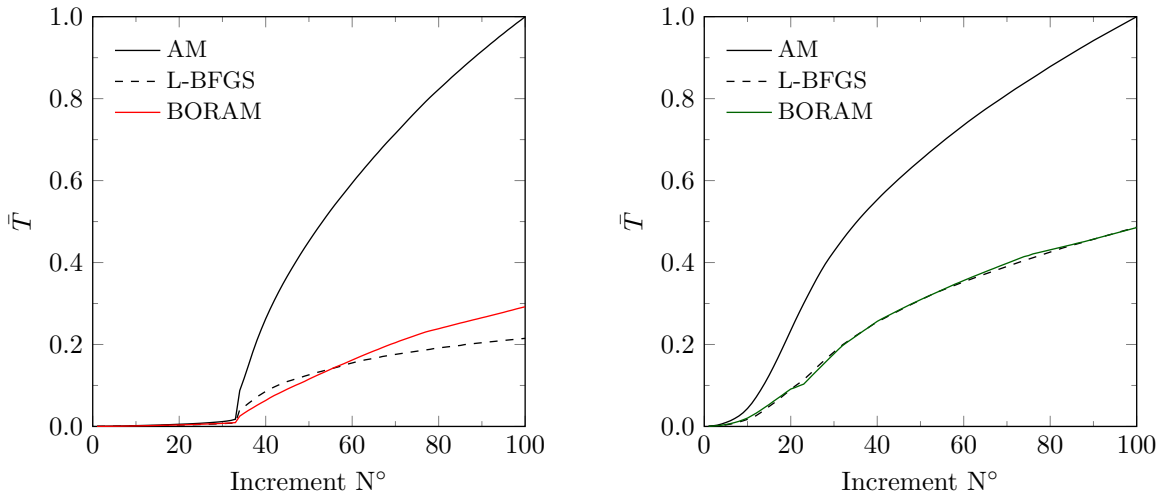

(a) `AT2` model (b) `CZM` model

Source: The author.

5.5 Wedge-splitting test - WST

This example considers the wedge-splitting test conducted by [137]. It involves a square-shaped specimen with dimensions 800 mm × 800 mm × 400 mm, featuring a vertical notch extending approximately half the specimen height, as depicted in Fig. 34a. The specimen is vertically supported at the center of each half of the bottom edge. Two horizontal splitting displacements $\bar{\boldsymbol{u}}$ are applied to the upper lateral faces of the notch through a vertically pushed wedge mechanism.

The material properties are adopted from the experimental test [137]: Young's modulus $E = 28.3$ kN/mm^2, Poisson's ratio $\nu = 0.18$, tensile strength $f_t = 2.12 \times 10^{-3}$ kN/mm^2, and fracture energy $\mathcal{G}_c = 3.73 \times 10^{-4}$ kN/mm. The concrete softening law is employed in the analysis, and direct displacement control is used throughout the simulation. As is illustrated in 34b, the specimen is discretized with a mesh of size $h = 1$ mm where the phase-field evolution is expected. A length scale $\ell = 5$ mm is considered in all simulations.

The load is applied in 100 increments, with a prescribed displacement of $\bar{u} = 2.5$ mm, as done by [99]. The final damage profile is shown in Fig. 35. Fig. 36 shows the splitting load *versus* CMOD (Crack Mouth Opening Displacement) curves. It is observed

that the AT2 models leads to a much higher peak load compared to the CZM model, which is also observed in [99]. Since the results of all algorithms coincide, only the results of the BORAM algorithm are shown in Figs. 35 and 36.

Figure 34 – **Wedge-splitting test**: (a) Geometry (mm) and boundary conditions. (b) Finite element discretization (30,190 elements).

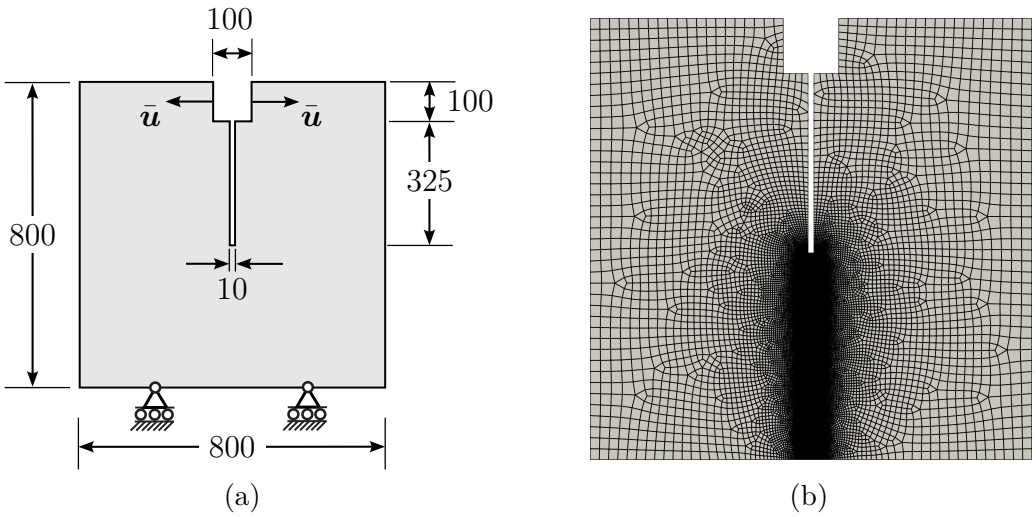

(a) (b)

Source: The author.

Figure 35 – **Wedge-splitting test**: Damage profile at CMOD 2.5 mm.

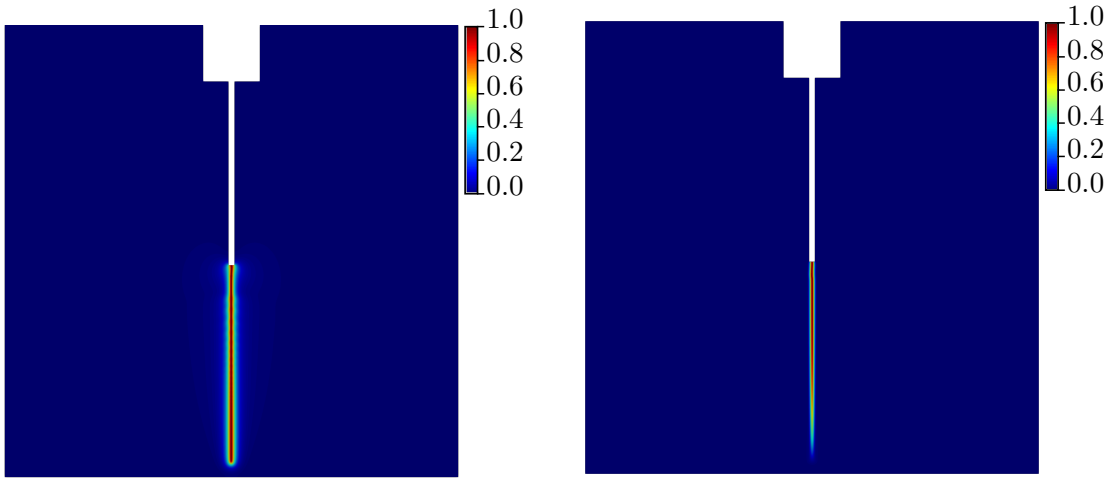

(a) AT2 model (b) CZM model

Source: The author.

As is demonstrated in Fig. 37, the BORAM algorithm significantly reduces the number of iterations for all models compared to the AM and L-BFGS algorithms. Specially for the CZM model, where L-BFGS requires much more iterations than AM to achieve convergence at several increments. For this example, the BORAM algorithm is able to reduce the number of iterations required by L-BFGS algorithm. By analyzing Fig. 38, we can observe that both L-BFGS and BORAM algorithms lead to a significant reduction in

computational cost compared to the AM algorithm, being around 5 times faster for both models. However, for the `CZM` model, only BORAM provides a relevant reduction in the computational cost compared to AM, leading to a total time around 2 times smaller.

Figure 36 – **Wedge-splitting test**: Load *versus* displacement curves.

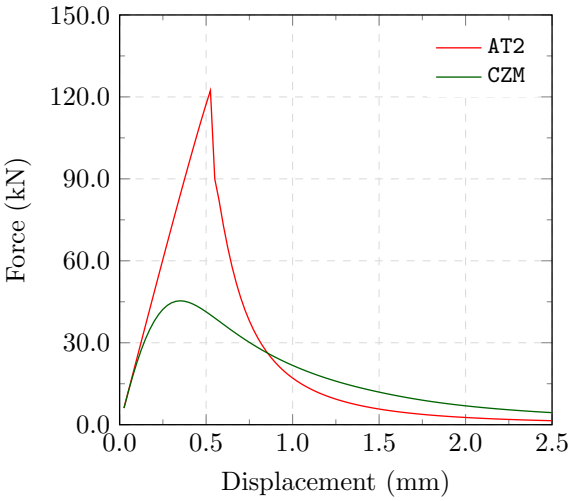

Source: The author.

Figure 37 – **Wedge-splitting test**: Iteration number at each increment.

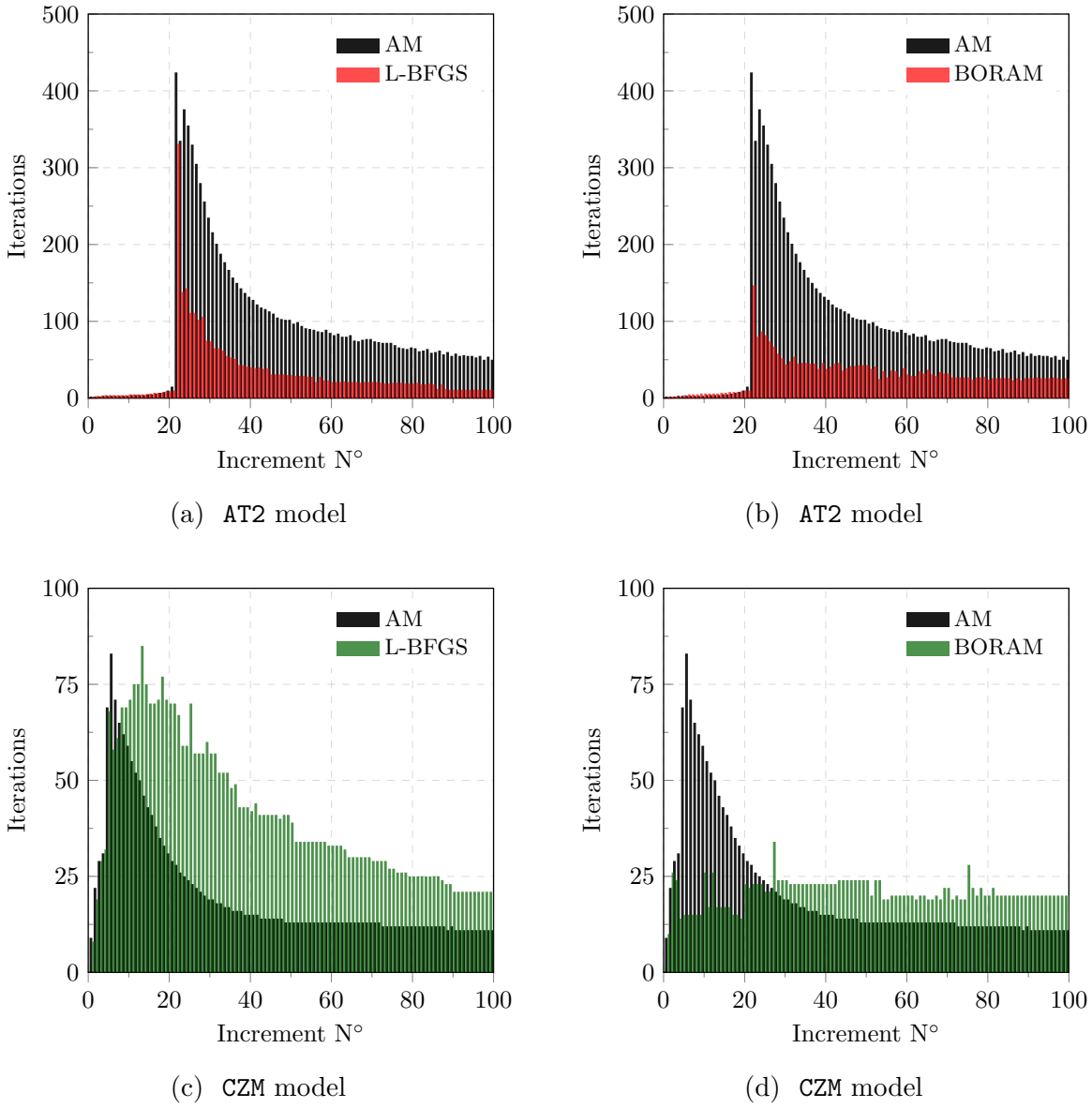

(a) `AT2` model

(b) `AT2` model

(c) `CZM` model

(d) `CZM` model

Source: The author.

Figure 38 – **Wedge-splitting test**: Accumulated time at each increment.

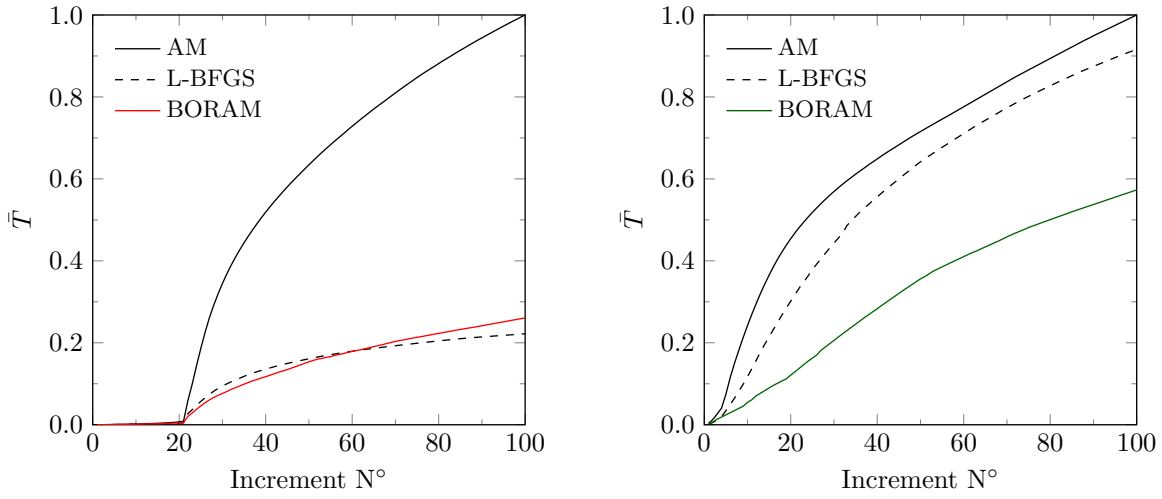

(a) `AT2` model

(b) `CZM` model

Source: The author.

5.6 Discussion on computational performance

All results related to the computational performance of the AM, L-BFGS, and BORAM algorithms for each example are summarized in this section. The total number of iterations and time required for each algorithm to solve all pseudo-time steps of each example are shown in Tab. 3 and Tab. 4. It is important to emphasize that all analyses are subjected to the same convergence criteria. Moreover, numbers in parentheses in the fifth column of Tab. 3 and Tab. 4 indicates the total number of L-BFGS or BORAM iterations with line search activated.

As can be observed in Tab. 3, in general the L-BFGS algorithm requires fewer iterations and lower CPU time compared to the AM algorithm to solve any example. By analysing fifth column, we can observe that the line search plays an important role in analyses with the `AT2` model, as it is activated in all examples. On the other hand, in cases with smoother crack propagation, such as the BUT and SENPS with the `CZM` model (see Figs. 11 and 21), the line search is not activated at any step. This leads us to conclude that the line search is primarily needed in steps with unstable crack propagation. It is worth mentioning that the line search is essential in examples where it was activated to prevent divergence of the L-BFGS algorithm, as is highlighted in Fig. 6. Specially in LSP and WST examples, where the line search is activated in significant number of iterations. Furthermore, for certain steps the line search also improved the convergence rate by giving $\lambda > 1$, similar to the results presented in Figs. 7c, 8c and 8f.

Table 3 – Computational performance of the AM and L-BFGS algorithms for each example. Numbers in parentheses indicate the number of iterations with line search activated.

Example	Number of elements	Model	Total number of iterations		Total time (T) (h:m:s)		$\frac{T_{\text{L-BFGS}}}{T_{\text{AM}}}(\%)$
			AM	L-BFGS	AM	L-BFGS	
BUT	1,000	`AT2`	1,545	1,053 (29)	00:03:10	00:00:46	24.2
		`CZM`	3,443	1,946 (0)	00:09:17	00:01:46	18.9
SENPT	22,566	`AT2`	2,064	1,830 (95)	01:52:05	00:36:41	32.7
		`CZM`	11,167	3,762 (51)	10:46:23	01:15:09	11.6
SENPS	66,933	`AT2`	26,877	10,466 (5)	79:04:24	08:34:32	10.8
		`CZM`	6,449	3,665 (0)	19:37:39	03:03:34	15.6
S3PBT	104,147	`AT2`	11,423	8,977 (111)	50:07:57	11:50:05	23.6
		`CZM`	5,107	2,423 (96)	24:54:08	03:43:16	14.9
LSP	20,053	`AT2`	6,920	2,939 (766)	05:33:02	01:11:36	21.5
		`CZM`	2,343	2,811 (430)	02:05:21	01:00:58	48.6
WST	30,190	`AT2`	9,315	3,093 (1,809)	11:37:07	02:34:46	22.2
		`CZM`	2,079	4,092 (1,099)	02:47:48	02:33:43	91.6

Source: The author.

Meanwhile, Tab. 4 demonstrates that the BORAM algorithm also provides a substantial reduction in the number of iterations and CPU time compared to the AM algorithm for all examples. Similar to the L-BFGS algorithm, the BORAM also employed the line search in several cases, except for the BUT example with the `CZM` model, as shown in the fifth column of Tab. 4. When comparing the L-BFGS and BORAM algorithms, it is conclued that BORAM is slightly less efficient than L-BFGS in general, but it still outperforms the AM algorithm. However, BORAM algorithm considerable reduces the number of iterations for the `AT2` model in the S3PBT examples and the computational cost for the `CZM` model in the WST example.

Many aspects impact the performance of the L-BFGS and BORAM algorithms, including discretization size, phase-field model, crack propagation complexity, number of matrix updates, and increments, among others. Nevertheless, when evaluating the last column of both Tab. 3 and Tab. 4 – where is presented for each example the L-BFGS and BORAM computational cost as a percentage of the AM computational cost –, we can summarize that the proposed L-BFGS and BORAM results in an approximate computational time saving of about five on average. This is a significant reduction in computational cost, especially for large-scale problems with complex crack propagation. In some cases, such as the SENPT and SENPS examples, where the L-BFGS and BORAM algorithms are about 10 times faster than the AM algorithm.

Table 4 – Computational performance of the AM and BORAM algorithms for each example. Numbers in parentheses indicate the number of iterations with line search activated.

Example	Number of elements	Model	Total number of iterations		Total time (T) (h:m:s)		$\frac{T_{\text{BORAM}}}{T_{\text{AM}}}(\%)$
			AM	BORAM	AM	BORAM	
BUT	1,000	AT2	1,545	977 (10)	00:03:10	00:00:45	23.8
		CZM	3,443	1,895 (0)	00:09:17	00:02:03	22.0
SENPT	22,566	AT2	2,064	984 (2)	01:52:05	00:24:43	22.1
		CZM	11,167	3,762 (51)	10:46:23	01:16:18	11.5
SENPS	66,933	AT2	26,877	6,127 (3)	79:04:24	15:29:13	19.6
		CZM	6,449	3,665 (62)	19:37:39	04:30:14	22.9
S3PBT	104,147	AT2	11,423	2,451 (77)	50:07:57	08:53:14	17.7
		CZM	5,107	2,187 (2)	24:54:08	05:28:50	22.0
LSP	20,053	AT2	6,920	2,738 (434)	05:33:02	01:37:16	29.2
		CZM	2,343	2,263 (419)	02:05:21	01:00:50	48.5
WST	30,190	AT2	9,315	3,121 (812)	11:37:07	03:01:44	26.1
		CZM	2,079	2,077 (794)	02:47:48	01:36:10	57.3

Source: The author.

6 CONCLUSIONS

This work presents two algorithmic innovations for phase-field fracture analysis: an enhanced Limited Broyden–Fletcher–Goldfarb–Shanno (L-BFGS) method with a novel quasi-Newton line search strategy, and the BORAM (Hybrid L-**B**FGS **ORAM**) algorithm that combines L-BFGS with Over-Relaxed Alternating Minimization (ORAM). The study aimed to enhance both the robustness and computational efficiency of monolithic solvers when dealing with highly nonlinear and non-convex energy functionals characteristic of phase-field fracture mechanics, particularly addressing the challenges arising from unstable crack propagation phenomena.

The L-BFGS enhancement incorporates a sophisticated gradient-based line search that effectively mitigates divergence issues inherent to quasi-Newton methods in fracture problems. Building upon this foundation, the BORAM algorithm provides an adaptive solution strategies that automatically adjust to the evolving nature of crack propagation problems. Both approaches can be applied to variational and non-variational formulations since no restrictive assumptions are made regarding the energy functional, providing versatile frameworks for diverse phase-field fracture simulations.

Both algorithms were rigorously evaluated through comprehensive numerical experiments covering brittle and quasi-brittle fracture scenarios across multiple benchmark problems. The results demonstrate that the proposed methodologies achieve substantial reductions in computational cost while maintaining high accuracy compared to traditional alternating minimization approaches. The key contributions and innovations of this work are summarized as follows:

- **Enhanced L-BFGS with Novel Line Search Strategy**: The development of a gradient-based line search method specifically tailored for the L-BFGS algorithm in phase-field fracture mechanics. This approach ensures algorithmic robustness by dynamically adjusting the search direction with adaptive step sizes (λ), preventing divergence at critical load steps ($\lambda < 1$) while enhancing convergence rates ($\lambda > 1$). Therefore, the method supports both positive and negative step sizes, providing flexibility in search directions as originally suggested by [24]. This enhancement serves as the foundation for the BORAM algorithm.

- **BORAM Hybrid Algorithm**: This novel adaptive solution strategy combines the computational efficiency of the enhanced L-BFGS method with the robustness of Over-Relaxed Alternating Minimization (ORAM). The algorithm employs a sophisticated convergence rate detection mechanism based on semi-logarithmic linear

regression analysis of residual norms, enabling seamless automatic switching between solution methodologies based on real-time assessment of crack propagation events.

- **Computational Efficiency**: Both the enhanced L-BFGS and BORAM algorithms demonstrate significant computational advantages over traditional alternating minimization (AM) approach. The methods achieve average computational savings of approximately five times compared to standard alternating minimization.

- **Comprehensive Open-Source Implementation**: Both algorithms have been implemented and made available as open-source code through the BORAM repository, allowing researchers and practitioners worldwide to utilize and further develop these methodologies. The comprehensive implementation includes documentation, example problems, and integration guidelines, providing a robust platform for collaboration and continuous improvement in the computational fracture mechanics community.

The dual algorithmic contributions of this work have implications for computational fracture mechanics and broad applicability across various engineering disciplines where fracture prediction and failure analysis are critical. Potential areas of immediate impact include aerospace structural analysis, civil infrastructure assessment, and mechanical component design, where the computational efficiency gains are particularly valuable for large-scale simulations involving complex geometries and loading conditions. The seamless integration capabilities of both algorithms allow for straightforward implementation into existing finite element frameworks, enabling immediate performance enhancements in commercial and research software packages.

6.1 Topics for future investigation

The following are some topics for future investigation derived directly from the contents that were explored in this Ph.D. thesis:

- **Implementation of box-constrained L-BFGS algorithm**: Develop a constrained optimization variant to enforce the irreversibility constraint directly within the quasi-Newton framework. This approach would eliminate the computational overhead associated with history field tracking while enabling the application to `AT1` phase-field model, thereby expanding the algorithmic applicability and improving computational efficiency.

- **Adaptive load increment strategies**: Integrate automatic adaptive load increment schemes into both L-BFGS and BORAM algorithms. While constant load increments were employed in the current study, adaptive schemes would enhance

algorithmic efficiency by dynamically adjusting increment sizes based on convergence behavior. Preliminary observations indicate that L-BFGS can accommodate larger load increments, but systematic investigation is required to establish optimal increment bounds without compromising solution accuracy.

- **Adaptive mesh refinement integration**: Incorporate adaptive mesh refinement techniques to optimize computational resource allocation while preserving solution accuracy, particularly in regions characterized by steep stress gradients or complex crack geometries. The combination of the developed algorithms with adaptive meshing strategies would provide additional computational cost reductions and enable efficient simulation of large-scale fracture problems.

REFERENCES

1 GRIFFITH, A. A. The phenomena of rupture and flow in solids. **Philosophical Transactions of the Royal Society of London. Series A, Containing Papers of a Mathematical or Physical Character**, The Royal Society, v. 221, p. 163–198, 1921.

2 BABUŠKA, I.; MELENK, J. M. The partition of unity finite element method. **International Journal for Numerical Methods in Engineering**, v. 40, n. 4, p. 727–758, 1997.

3 BELYTSCHKO, T.; BLACK, T. Elastic crack growth in finite elements with minimal remeshing. **International Journal for Numerical Methods in Engineering**, v. 45, n. 5, p. 601–620, 1999.

4 DUARTE, C. A.; ODEN, J. T. *H-p* clouds — an *h-p* meshless method. **Numerical Methods for Partial Differential Equations**, v. 12, n. 6, p. 673–705, Nov 1996.

5 FRANCFORT, G.; MARIGO, J.-J. Revisiting brittle fracture as an energy minimization problem. **Journal of the Mechanics and Physics of Solids**, v. 46, n. 8, p. 1319–1342, 1998.

6 BOURDIN, B.; FRANCFORT, G.; MARIGO, J.-J. Numerical experiments in revisited brittle fracture. **Journal of the Mechanics and Physics of Solids**, v. 48, n. 4, p. 797–826, 2000.

7 BOURDIN, B.; FRANCFORT, G.; MARIGO, J.-J. The variational approach to fracture. **Journal of Elasticity**, v. 91, n. 1-3, p. 5–148, 2008.

8 MIEHE, C.; ALDAKHEEL, F.; RAINA, A. Phase field modeling of ductile fracture at finite strains: a variational gradient-extended plasticity-damage theory. **International Journal of Plasticity**, v. 84, p. 1–32, 2016.

9 BORDEN, M. J.; VERHOOSEL, C. V.; SCOTT, M. A.; HUGHES, T. J.; LANDIS, C. M. A phase-field description of dynamic brittle fracture. **Computer Methods in Applied Mechanics and Engineering**, v. 217-220, p. 77–95, 2012.

10 GEELEN, R. J.; LIU, Y.; HU, T.; TUPEK, M. R.; DOLBOW, J. E. A phase-field formulation for dynamic cohesive fracture. **Computer Methods in Applied Mechanics and Engineering**, v. 348, p. 680–711, 2019.

11 MIEHE, C.; SCHÄNZEL, L.-M.; ULMER, H. Phase field modeling of fracture in multi-physics problems. part I. balance of crack surface and failure criteria for brittle crack propagation in thermo-elastic solids. **Computer Methods in Applied Mechanics and Engineering**, v. 294, p. 449–485, 2015.

12 MIEHE, C.; HOFACKER, M.; SCHÄNZEL, L.-M.; ALDAKHEEL, F. Phase field modeling of fracture in multi-physics problems. part II. coupled brittle-to-ductile failure criteria and crack propagation in thermo-elastic–plastic solids. **Computer Methods in Applied Mechanics and Engineering**, v. 294, p. 486–522, 2015.

13 MIEHE, C.; SCHÄNZEL, L.-M. Phase field modeling of fracture in rubbery polymers. part I: Finite elasticity coupled with brittle failure. **Journal of the Mechanics and Physics of Solids**, v. 65, p. 93–113, 2014.

14 CUI, C.; MA, R.; MARTÍNEZ-PAÑEDA, E. Electro-chemo-mechanical phase field modeling of localized corrosion: theory and comsol implementation. **Engineering with Computers**, v. 39, n. 6, p. 3877–3894, 2023.

15 MARTÍNEZ-PAÑEDA, E.; GOLAHMAR, A.; NIORDSON, C. F. A phase field formulation for hydrogen assisted cracking. **Computer Methods in Applied Mechanics and Engineering**, v. 342, p. 742–761, 2018.

16 KRISTENSEN, P. K.; NIORDSON, C. F.; MARTÍNEZ-PAÑEDA, E. A phase field model for elastic-gradient-plastic solids undergoing hydrogen embrittlement. **Journal of the Mechanics and Physics of Solids**, v. 143, p. 104093, 2020.

17 MIKELIĆ, A.; WHEELER, M. F.; WICK, T. Phase-field modeling of a fluid-driven fracture in a poroelastic medium. **Computational Geosciences**, v. 19, p. 1171–1195, 2015.

18 LEE, S.; WHEELER, M. F.; WICK, T. Pressure and fluid-driven fracture propagation in porous media using an adaptive finite element phase field model. **Computer Methods in Applied Mechanics and Engineering**, v. 305, p. 111–132, 2016.

19 HEISTER, T.; WHEELER, M. F.; WICK, T. A primal-dual active set method and predictor-corrector mesh adaptivity for computing fracture propagation using a phase-field approach. **Computer Methods in Applied Mechanics and Engineering**, v. 290, p. 466–495, 2015.

20 JIN, T.; LI, Z.; CHEN, K. A novel phase-field monolithic scheme for brittle crack propagation based on the limited-memory BFGS method with adaptive mesh refinement. **International Journal for Numerical Methods in Engineering**, v. 125, n. 22, p. e7572, 2024.

21 PATIL, R.; MISHRA, B.; SINGH, I. An adaptive multiscale phase field method for brittle fracture. **Computer Methods in Applied Mechanics and Engineering**, v. 329, p. 254–288, 2018.

22 GEELEN, R.; PLEWS, J.; TUPEK, M.; DOLBOW, J. An extended/generalized phase-field finite element method for crack growth with global-local enrichment. **International Journal for Numerical Methods in Engineering**, v. 121, n. 11, p. 2534–2557, 2020.

23 MUIXÍ, A.; MARCO, O.; RODRÍGUEZ-FERRAN, A.; FERNÁNDEZ-MÉNDEZ, S. A combined XFEM phase-field computational model for crack growth without remeshing. **Computational Mechanics**, v. 67, n. 1, p. 231–249.

24 GERASIMOV, T.; LORENZIS, L. D. A line search assisted monolithic approach for phase-field computing of brittle fracture. **Computer Methods in Applied Mechanics and Engineering**, v. 312, p. 276–303, 2016, phase Field Approaches to Fracture.

25 WICK, T. An error-oriented Newton/inexact augmented lagrangian approach for fully monolithic phase-field fracture propagation. **SIAM Journal on Scientific Computing**, v. 39, n. 4, p. B589–B617, 2017.

26 WICK, T. Modified Newton methods for solving fully monolithic phase-field quasi-static brittle fracture propagation. **Computer Methods in Applied Mechanics and Engineering**, v. 325, p. 577–611, 2017.

27 LAMPRON, O.; THERRIAULT, D.; LÉVESQUE, M. An efficient and robust monolithic approach to phase-field quasi-static brittle fracture using a modified Newton method. **Computer Methods in Applied Mechanics and Engineering**, v. 386, p. 114091, 2021.

28 KOPANIČÁKOVÁ, A.; KRAUSE, R. A recursive multilevel trust region method with application to fully monolithic phase-field models of brittle fracture. **Computer Methods in Applied Mechanics and Engineering**, v. 360, p. 112720, 2020.

29 MIEHE, C.; WELSCHINGER, F.; HOFACKER, M. Thermodynamically consistent phase-field models of fracture: Variational principles and multi-field fe implementations. **International Journal for Numerical Methods in Engineering**, v. 83, n. 10, p. 1273–1311, 2010.

30 MIEHE, C.; HOFACKER, M.; WELSCHINGER, F. A phase field model for rate-independent crack propagation: Robust algorithmic implementation based on operator splits. **Computer Methods in Applied Mechanics and Engineering**, v. 199, n. 45, p. 2765–2778, 2010.

31 AMOR, H.; MARIGO, J.-J.; MAURINI, C. Regularized formulation of the variational brittle fracture with unilateral contact: Numerical experiments. **Journal of the Mechanics and Physics of Solids**, v. 57, n. 8, p. 1209–1229, 2009.

32 WU, J.-Y.; HUANG, Y.; NGUYEN, V. P. On the BFGS monolithic algorithm for the unified phase field damage theory. **Computer Methods in Applied Mechanics and Engineering**, v. 360, p. 112704, 2020.

33 KRISTENSEN, P. K.; MARTÍNEZ-PAÑEDA, E. Phase field fracture modelling using quasi-Newton methods and a new adaptive step scheme. **Theoretical and Applied Fracture Mechanics**, v. 107, p. 102446, 2020.

34 BRUN, M. K.; WICK, T.; BERRE, I.; NORDBOTTEN, J. M.; RADU, F. A. An iterative staggered scheme for phase field brittle fracture propagation with stabilizing parameters. **Computer Methods in Applied Mechanics and Engineering**, v. 361, p. 112752, 2020.

35 FARRELL, P.; MAURINI, C. Linear and nonlinear solvers for variational phase-field models of brittle fracture. **International Journal for Numerical Methods in Engineering**, v. 109, n. 5, p. 648–667, 2017.

36 STORVIK, E.; BOTH, J. W.; SARGADO, J. M.; NORDBOTTEN, J. M.; RADU, F. A. An accelerated staggered scheme for variational phase-field models of brittle fracture. **Computer Methods in Applied Mechanics and Engineering**, v. 381, p. 113822, 2021.

37 SCHAPIRA, Y.; RADTKE, L.; KOLLMANNSBERGER, S.; DÜSTER, A. Performance of acceleration techniques for staggered phase-field solutions. **Computer Methods in Applied Mechanics and Engineering**, v. 410, p. 116029, 2023.

38 GUPTA, A.; KRISHNAN, U. M.; CHOWDHURY, R.; CHAKRABARTI, A. An auto-adaptive sub-stepping algorithm for phase-field modeling of brittle fracture. **Theoretical and Applied Fracture Mechanics**, v. 108, p. 102622, 2020.

39 YU, Y.; HOU, C.; RABCZUK, T.; ZHAO, M. An adaptive incremental solution scheme for the phase field model of fracture. **Engineering Fracture Mechanics**, v. 315, p. 110799, 2025.

40 BHARALI, R.; GOSWAMI, S.; ANITESCU, C.; RABCZUK, T. A robust monolithic solver for phase-field fracture integrated with fracture energy based arc-length method and under-relaxation. **Computer Methods in Applied Mechanics and Engineering**, v. 394, p. 114927, 2022.

41 WU, J.-Y.; HUANG, Y.; ZHOU, H.; NGUYEN, V. P. Three-dimensional phase-field modeling of mode I + II/III failure in solids. **Computer Methods in Applied Mechanics and Engineering**, v. 373, p. 113537, 2021.

42 SMITH, M. **ABAQUS/Standard User's Manual, Version 6.9**. United States: Dassault Systèmes Simulia Corp, 2009.

43 RAMOS, C. S.; DUARTE, C. A.; SHAUER, N.; PROENÇA, S. P. Phase-field fracture analysis: A gradient-based line search strategy for the L-BFGS algorithm. **Computer Methods in Applied Mechanics and Engineering**, v. 445, p. 118170, 2025.

44 ANDERSON, T. **Fracture Mechanics: Fundamentals and Applications**. Boca Raton: CRC Press, 2017.

45 ASHBY, M. F.; JONES, D. R. Chapter 9 - dislocations and yielding in crystals. *In*: ASHBY, M. F.; JONES, D. R. (ed.). **Engineering Materials 1 (Fourth Edition)**. Fourth edition. Boston: Butterworth-Heinemann, 2012. p. 135–145. ISBN 978-0-08-096665-6.

46 TALREJA, R. Damage and failure of composite materials. *In*: _____. **Advanced Theories for Deformation, Damage and Failure in Materials**. Cham: Springer International Publishing, 2023. p. 235–280. ISBN 978-3-031-04354-3.

47 KUHN, C. **Numerical and analytical investigation of a phase field model for fracture**. 2013. Tese (Doutorado) — Technischen Universitat Kaiserslautern, 2013.

48 CHAMBOLLE, A.; FRANCFORT, G.; MARIGO, J.-J. When and how do cracks propagate? **Journal of the Mechanics and Physics of Solids**, v. 57, n. 9, p. 1614–1622, 2009.

49 HUSSAIN, M.; PU, S.; UNDERWOOD, J. Strain energy release rate for a crack under combined mode i and mode ii. *In*: **Fracture Analysis: Proceedings of the 1973 National Symposium on Fracture Mechanics, Part II**. [*S.l.: s.n.*]: ASTM International, 1974. ISBN 978-0-8031-0361-0.

50 ERDOGAN, F.; SIH, G. C. On the crack extension in plates under plane loading and transverse shear. **Journal of Basic Engineering**, v. 85, n. 4, p. 519–525, 12 1963.

51 IRWIN, G. R. Analysis of stresses and strains near the end of a crack traversing a plate. **Journal of Applied Mechanics**, v. 24, p. 361–364, 1957.

52 BARENBLATT, G. The mathematical theory of equilibrium cracks in brittle fracture. *In*: DRYDEN, H.; VON KÁRMÁN, T.; KUERTI, G.; VAN DEN DUNGEN, F.; HOWARTH, L. (ed.). [*S.l.: s.n.*]: Elsevier, 1962, (Advances in Applied Mechanics, v. 7). p. 55–129.

53 BOUCHARD, P.; BAY, F.; CHASTEL, Y. Numerical modelling of crack propagation: automatic remeshing and comparison of different criteria. **Computer Methods in Applied Mechanics and Engineering**, v. 192, n. 35, p. 3887–3908, 2003.

54 HILLERBORG, A.; MODéER, M.; PETERSSON, P.-E. Analysis of crack formation and crack growth in concrete by means of fracture mechanics and finite elements. **Cement and Concrete Research**, v. 6, n. 6, p. 773–781, 1976.

55 NGUYEN, V. P. An open source program to generate zero-thickness cohesive interface elements. **Advances in Engineering Software**, v. 74, p. 27–39, 2014.

56 NGUYEN, V. P. Discontinuous galerkin/extrinsic cohesive zone modeling: Implementation caveats and applications in computational fracture mechanics. **Engineering Fracture Mechanics**, v. 128, p. 37–68, 2014.

57 BABUSKA, I.; CALOZ, G.; OSBORN, J. E. Special finite element methods for a class of second order elliptic problems with rough coefficients. **SIAM Journal on Numerical Analysis**, v. 31, n. 4, p. 945–981, 1994.

58 MELENK, J.; BABUSKA, I. The partition of unity finite element method: Basic theory and applications. **Computer Methods in Applied Mechanics and Engineering**, v. 139, n. 1, p. 289–314, 1996.

59 MOËS, N.; DOLBOW, J.; BELYTSCHKO, T. A finite element method for crack growth without remeshing. **International Journal for Numerical Methods in Engineering**, v. 46, n. 1, p. 131–150, 1999.

60 BELYTSCHKO, T.; GRACIE, R.; VENTURA, G. A review of extended/generalized finite element methods for material modeling. **Modelling and Simulation in Materials Science and Engineering**, v. 17, n. 4, p. 043001, apr 2009.

61 FRIES, T.-P.; BELYTSCHKO, T. The extended/generalized finite element method: An overview of the method and its applications. **International Journal for Numerical Methods in Engineering**, v. 84, n. 3, p. 253–304, 2010.

62 GUPTA, V.; DUARTE, C. A.; BABUŠKA, I.; BANERJEE, U. A stable and optimally convergent generalized FEM (SGFEM) for linear elastic fracture mechanics. **Computer Methods in Applied Mechanics and Engineering**, v. 266, p. 23–39, 2013.

63 GUPTA, V.; DUARTE, C. A.; BABUŠKA, I.; BANERJEE, U. Stable GFEM (SGFEM): Improved conditioning and accuracy of GFEM/XFEM for three-dimensional fracture mechanics. **Computer Methods in Applied Mechanics and Engineering**, v. 289, p. 355–386, 2015.

64 ZHANG, Q.; BABUŠKA, I.; BANERJEE, U. Robustness in Stable Generalized Finite Element Methods (SGFEM) applied to Poisson problems with crack singularities. **Computer Methods in Applied Mechanics and Engineering**, v. 311, p. 476–502, 2016.

65 BELYTSCHKO, T.; CHEN, H.; XU, J.; ZI, G. Dynamic crack propagation based on loss of hyperbolicity and a new discontinuous enrichment. **International Journal for Numerical Methods in Engineering**, v. 58, n. 12, p. 1873–1905, 2003.

66 DUMSTORFF, P.; MESCHKE, G. Crack propagation criteria in the framework of X-FEM-based structural analyses. **International Journal for Numerical and Analytical Methods in Geomechanics**, v. 31, n. 2, p. 239–259, 2007.

67 BORDAS, S.; RABCZUK, T.; ZI, G. Three-dimensional crack initiation, propagation, branching and junction in non-linear materials by an extended meshfree method without asymptotic enrichment. **Engineering Fracture Mechanics**, v. 75, n. 5, p. 943 – 960, 2008.

68 SUKUMAR, N.; DOLBOW, J. E.; MOËS, N. Extended finite element method in computational fracture mechanics: a retrospective examination. **International Journal of Fracture**, v. 196, p. 189 – 206, 2015.

69 KACHANOV, L. M. Rupture time under creep conditions. **International Journal of Fracture**, v. 97, p. 11–18, 1999.

70 MURAKAMI, S. Material damage and continuum damage mechanics. *In*: _____. **Continuum Damage Mechanics: A Continuum Mechanics Approach to the Analysis of Damage and Fracture**. Dordrecht: Springer Netherlands, 2012. p. 3–13.

71 JIRÁSEK, M. Mathematical analysis of strain localization. **Revue Européenne de Génie Civil**, Taylor & Francis, v. 11, n. 7-8, p. 977–991, 2007.

72 PEERLINGS, R. H. J.; BORST, R. D.; BREKELMANS, W. A. M.; VREE, J. H. P. D. Gradient enhanced damage for quasi-brittle materials. **International Journal for Numerical Methods in Engineering**, v. 39, n. 19, p. 3391–3403, 1996.

73 LORENTZ, E.; ANDRIEUX, S. A variational formulation for nonlocal damage models. **International Journal of Plasticity**, v. 15, n. 2, p. 119–138, 1999.

74 PHAM, K.; AMOR, H.; MARIGO, J.-J.; MAURINI, C. Gradient damage models and their use to approximate brittle fracture. **International Journal of Damage Mechanics**, v. 20, n. 4, p. 618–652, 2011.

75 SILLING, S.; LEHOUCQ, R. Peridynamic theory of solid mechanics. *In*: AREF, H.; GIESSEN, E. van der (ed.). **Advances in Applied Mechanics**. [*S.l.: s.n.*]: Elsevier, 2010, (Advances in Applied Mechanics, v. 44). p. 73–168.

76 HOFACKER, M.; MIEHE, C. Continuum phase field modeling of dynamic fracture: variational principles and staggered fe implementation. **International Journal of Fracture**, v. 178, n. 1, p. 113–129, 2012.

77 HAKIM, V.; KARMA, A. Laws of crack motion and phase-field models of fracture. **Journal of the Mechanics and Physics of Solids**, v. 57, n. 2, p. 342–368, 2009.

78 KARMA, A.; KESSLER, D. A.; LEVINE, H. Phase-field model of mode iii dynamic fracture. **Phys. Rev. Lett.**, American Physical Society, v. 87, p. 045501, Jul 2001.

79 SIMONE, A.; WELLS, G. N.; SLUYS, L. J. From continuous to discontinuous failure in a gradient-enhanced continuum damage model. **Computer Methods in Applied Mechanics and Engineering**, v. 192, n. 41, p. 4581–4607, 2003.

80 GIOVANARDI, B.; SCOTTI, A.; FORMAGGIA, L. A hybrid XFEM –phase field (Xfield) method for crack propagation in brittle elastic materials. **Computer Methods in Applied Mechanics and Engineering**, v. 320, p. 396 – 420, 2017.

81 GEELEN, R. J. M.; LIU, Y.; DOLBOW, J. E.; RODRíGUEZ-FERRAN, A. An optimization-based phase-field method for continuous-discontinuous crack propagation. **International Journal for Numerical Methods in Engineering**, v. 116, n. 1, p. 1–20, 2018.

82 WANG, Y.; WAISMAN, H. From diffuse damage to sharp cohesive cracks: A coupled XFEM framework for failure analysis of quasi-brittle materials. **Computer Methods in Applied Mechanics and Engineering**, v. 299, p. 57 – 89, 2016.

83 MOËS, N.; STOLZ, C.; BERNARD, P.-E.; CHEVAUGEON, N. A level set based model for damage growth: The thick level set approach. **International Journal for Numerical Methods in Engineering**, v. 86, n. 3, p. 358–380, 2011.

84 MOREAU, K.; MOËS, N.; PICART, D.; STAINIER, L. Explicit dynamics with a non-local damage model using the thick level set approach. **International Journal for Numerical Methods in Engineering**, v. 102, n. 3-4, p. 808–838, 2015.

85 CAZES, F.; MOËS, N. Comparison of a phase-field model and of a thick level set model for brittle and quasi-brittle fracture. **International Journal for Numerical Methods in Engineering**, v. 103, n. 2, p. 114–143, 2015.

86 BOURDIN, B. Numerical implementation of the variational formulation for quasi-static brittle fracture. **Interfaces and Free Boundaries**, v. 9, n. 3, p. 411 – 430, 2007.

87 BOURDIN, B. The variational formulation of brittle fracture: numerical implementation and extensions. *In*: COMBESCURE, A.; BORST, R. D.; BELYTSCHKO, T. (ed.). **IUTAM Symposium on Discretization Methods for Evolving Discontinuities**. Dordrecht: Springer Netherlands, 2007. p. 381–393.

88 AMBROSIO, L.; TORTORELLI, V. M. Approximation of functional depending on jumps by elliptic functional via t-convergence. **Communications on Pure and Applied Mathematics**, v. 43, n. 8, p. 999–1036, 1990.

89 BELLETTINI, G.; COSCIA, A. Discrete approximation of a free discontinuity problem. **Numerical Functional Analysis and Optimization**, Taylor & Francis, v. 15, n. 3-4, p. 201–224, 1994.

90 CHAMBOLLE, A. An approximation result for special functions with bounded deformation. **Journal de Mathématiques Pures et Appliquées**, v. 83, n. 7, p. 929–954, 2004.

91 SICSIC, P.; MARIGO, J.-J. From gradient damage laws to Griffith's theory of crack propagation. **Journal of Elasticity**, v. 113, n. 1, p. 55–74, 09 2013.

92 KUMAR, A.; LOPEZ-PAMIES, O. The phase-field approach to self-healable fracture of elastomers: A model accounting for fracture nucleation at large, with application to a class of conspicuous experiments. **Theoretical and Applied Fracture Mechanics**, v. 107, p. 102550, 2020.

93 KUMAR, A.; BOURDIN, B.; FRANCFORT, G. A.; LOPEZ-PAMIES, O. Revisiting nucleation in the phase-field approach to brittle fracture. **Journal of the Mechanics and Physics of Solids**, v. 142, p. 104027, 2020.

94 LOPEZ-PAMIES, O.; DOLBOW, J. E.; FRANCFORT, G. A.; LARSEN, C. J. Classical variational phase-field models cannot predict fracture nucleation. **Computer Methods in Applied Mechanics and Engineering**, v. 433, p. 117520, 2025.

95 MANDAL, T. K.; NGUYEN, V. P.; WU, J.-Y. Length scale and mesh bias sensitivity of phase-field models for brittle and cohesive fracture. **Engineering Fracture Mechanics**, v. 217, p. 106532, 2019.

96 ZHANG, X.; VIGNES, C.; SLOAN, S. W.; SHENG, D. Numerical evaluation of the phase-field model for brittle fracture with emphasis on the length scale. **Computational Mechanics**, v. 59, n. 5, p. 737–752, 2017.

97 WU, J.-Y. A unified phase-field theory for the mechanics of damage and quasi-brittle failure. **Journal of the Mechanics and Physics of Solids**, v. 103, p. 72–99, 2017.

98 LORENTZ, E.; GODARD, V. Gradient damage models: Toward full-scale computations. **Computer Methods in Applied Mechanics and Engineering**, v. 200, n. 21, p. 1927–1944, 2011.

99 WU, J.-Y.; NGUYEN, V. P. A length scale insensitive phase-field damage model for brittle fracture. **Journal of the Mechanics and Physics of Solids**, v. 119, p. 20–42, 2018.

100 LORENTZ, E. A nonlocal damage model for plain concrete consistent with cohesive fracture. **International Journal of Fracture**, v. 207, n. 2, p. 123–159, 2017.

101 BARENBLATT, G. The formation of equilibrium cracks during brittle fracture. general ideas and hypotheses. axially-symmetric cracks. **Journal of Applied Mathematics and Mechanics**, v. 23, n. 3, p. 622–636, 1959.

102 CORNELISSEN, H. A. W.; HORDIJK, D. A.; REINHARDT, H. W. Experimental determination of crack softening characteristics of normalweight and lightweight concrete. *In*: . [*S.l.: s.n.*], 1986.

103 KUHN, C.; SCHLÜTER, A.; MÜLLER, R. On degradation functions in phase field fracture models. **Computational Materials Science**, v. 108, p. 374–384, 2015, selected Articles from Phase-field Method 2014 International Seminar.

104 AMBATI, M.; GERASIMOV, T.; LORENZIS, L. D. Phase-field modeling of ductile fracture. **Computational Mechanics**, v. 55, p. 1017–1040, 2015.

105 WILSON, Z. A.; LANDIS, C. M. Phase-field modeling of hydraulic fracture. **Journal of the Mechanics and Physics of Solids**, v. 96, p. 264–290, 2016.

106 WU, J.-Y. Robust numerical implementation of non-standard phase-field damage models for failure in solids. **Computer Methods in Applied Mechanics and Engineering**, v. 340, p. 767–797, 2018.

107 GERASIMOV, T.; LORENZIS, L. D. On penalization in variational phase-field models of brittle fracture. **Computer Methods in Applied Mechanics and Engineering**, Elsevier BV, v. 354, p. 990–1026, sep 2019.

108 KOLDITZ, L.; MANG, K.; WICK, T. A modified combined active-set Newton method for solving phase-field fracture into the monolithic limit. **Computer Methods in Applied Mechanics and Engineering**, v. 414, p. 116170, 2023.

109 WHEELER, M.; WICK, T.; WOLLNER, W. An augmented-lagrangian method for the phase-field approach for pressurized fractures. **Computer Methods in Applied Mechanics and Engineering**, v. 271, p. 69–85, 2014.

110 LANCIONI, G.; ROYER-CARFAGNI, G. The variational approach to fracture mechanics. a practical application to the french panthéon in paris. **Journal of Elasticity**, v. 95, n. 30, 2009.

111 AMBATI, M.; GERASIMOV, T.; LORENZIS, L. D. A review on phase-field models of brittle fracture and a new fast hybrid formulation. **Computational Mechanics**, v. 55, n. 2, p. 383–405, 2015.

112 MIEHE, C.; ALDAKHEEL, F.; TEICHTMEISTER, S. Phase-field modeling of ductile fracture at finite strains: A robust variational-based numerical implementation of a gradient-extended theory by micromorphic regularization. **International Journal for Numerical Methods in Engineering**, v. 111, n. 9, p. 816–863, 2017.

113 LEE, S.; WHEELER, M. F.; WICK, T.; SRINIVASAN, S. Initialization of phase-field fracture propagation in porous media using probability maps of fracture networks. **Mechanics Research Communications**, v. 80, p. 16–23, 2017, multi-Physics of Solids at Fracture.

114 REID, J. K. A method for finding the optimum successive over-relaxation parameter. **The Computer Journal**, v. 9, n. 2, p. 200–204, 08 1966.

115 BROYDEN, C. G. The convergence of a class of double-rank minimization algorithms 1. general considerations. **IMA Journal of Applied Mathematics**, v. 6, n. 1, p. 76–90, 03 1970.

116 FLETCHER, R. A new approach to variable metric algorithms. **The Computer Journal**, v. 13, n. 3, p. 317–322, 01 1970.

117 GOLDFARB, D. A family of variable-metric methods derived by variational means. **Mathematics of Computation**, American Mathematical Society, v. 24, n. 109, p. 23–26, 1970.

118 SHANNO, D. F. Conditioning of quasi-Newton methods for function minimization. **Mathematics of Computation**, American Mathematical Society, v. 24, n. 111, p. 647–656, 1970.

119 MANDAL, T. K.; NGUYEN, V. P.; WU, J.-Y.; NGUYEN-THANH, C.; de Vaucorbeil, A. Fracture of thermo-elastic solids: Phase-field modeling and new results with an efficient monolithic solver. **Computer Methods in Applied Mechanics and Engineering**, v. 376, p. 113648, 2021.

120 MATTHIES, H.; STRANG, G. The solution of nonlinear finite element equations. **International Journal for Numerical Methods in Engineering**, v. 14, n. 11, p. 1613–1626, 1979.

121 LIU, D. C.; NOCEDAL, J. On the limited memory BFGS method for large scale optimization. **Mathematical Programming**, v. 45, n. 1, p. 503–528, 1989.

122 POWELL, M. J. D. On the convergence of the variable metric algorithm. **IMA Journal of Applied Mathematics**, v. 7, n. 1, p. 21–36, 02 1971.

123 BYRD, R. H.; NOCEDAL, J. A tool for the analysis of quasi-Newton methods with application to unconstrained minimization. **SIAM Journal on Numerical Analysis**, v. 26, n. 3, p. 727–739, 1989.

124 BYRD, R. H.; NOCEDAL, J.; YUAN, Y.-X. Global convergence of a class of quasi-Newton methods on convex problems. **SIAM Journal on Numerical Analysis**, Society for Industrial and Applied Mathematics, v. 24, n. 5, p. 1171–1190, 1987.

125 YUAN, G.; SHENG, Z.; WANG, B.; HU, W.; LI, C. The global convergence of a modified BFGS method for nonconvex functions. **Journal of Computational and Applied Mathematics**, v. 327, p. 274–294, 2018.

126 LI, D.-H.; FUKUSHIMA, M. A modified BFGS method and its global convergence in nonconvex minimization. **Journal of Computational and Applied Mathematics**, v. 129, n. 1, p. 15–35, 2001, nonlinear Programming and Variational Inequalities.

127 LI, D.-H.; FUKUSHIMA, M. On the global convergence of the BFGS method for nonconvex unconstrained optimization problems. **SIAM Journal on Optimization**, v. 11, n. 4, p. 1054–1064, 2001.

128 RAMOS, C. S.; SHAUER, N. **L-BFGS for phase-field fracture**. [*S.l.: s.n.*]: GitHub, 2025. https://github.com/gfemuillinois/BORAM.

129 GUENNEBAUD, G.; JACOB, B. *et al.* **Eigen v3**. 2010. http://eigen.tuxfamily.org.

130 MOLNÁR, G.; GRAVOUIL, A. 2D and 3D abaqus implementation of a robust staggered phase-field solution for modeling brittle fracture. **Finite Elements in Analysis and Design**, v. 130, p. 27–38, 2017.

131 WU, J.-Y.; HUANG, Y. Comprehensive implementations of phase-field damage models in abaqus. **Theoretical and Applied Fracture Mechanics**, v. 106, p. 102440, 2020.

132 NAJMEDDINE, A.; SHAKIBA, M. Efficient BFGS quasi-Newton method for large deformation phase-field modeling of fracture in hyperelastic materials. **Engineering Fracture Mechanics**, v. 310, p. 110463, 2024.

133 SELEŠ, K.; LESIČAR, T.; TONKOVIĆ, Z.; SORIĆ, J. A residual control staggered solution scheme for the phase-field modeling of brittle fracture. **Engineering Fracture Mechanics**, v. 205, p. 370–386, 2019.

134 GEUZAINE, C.; REMACLE, J.-F. Gmsh: A 3-d finite element mesh generator with built-in pre- and post-processing facilities. **International Journal for Numerical Methods in Engineering**, v. 79, n. 11, p. 1309–1331, 2009.

135 WU, J.-Y. A geometrically regularized gradient-damage model with energetic equivalence. **Computer Methods in Applied Mechanics and Engineering**, v. 328, p. 612–637, 2018.

136 WINKLER, B. J. **Traglastuntersuchungen von unbewehrten und bewehrten Betonstrukturen auf der Grundlage eines objektiven Werkstoffgesetzes für Beton**. [*S.l.: s.n.*]: Innsbruck University Press, 2001.

137 TRUNK, G. **Einfluss der Bauteilgröße auf die Bruchenergie von beton**. 1999. Tese (Doutorado) — Eidgenössische Technische Hochschule (ETH) Zürich, 1999.


EESC • USP